PULSED INDUCTIVE PLASMA STUDIES BY SPECTROSCOPY AND INTERNAL PROBE METHODS

by

WARNER CHARLES MEEKS

A DISSERTATION

Presented to the Faculty of the Graduate School of the

MISSOURI UNIVERSITY OF SCIENCE AND TECHNOLOGY

In Partial Fulfillment of the Requirements for the Degree

DOCTOR OF PHILOSOPHY

in

AEROSPACE ENGINEERING

2015

Approved by

Joshua Rovey, Advisor
Jie Gao
Hai-Lung Tsai
Carlos Castaño, Nuclear Engineering Dept.
Scott Kovaleski, Electrical Engineering Dept., UM-Columbia

ABSTRACT

The broad effort of the Missouri Plasmoid Experiment is to elucidate the energy conversion processes in a pulsed inductive discharge due to the presence of plasma. The test article is a 440 to 490 kHz theta-pinch (or solenoidal) geometry coil with a stored energy of around 80 joules. In this work experimental hydrogen, helium, argon and xenon data at back-fill pressures of 10 to 100 mTorr (1.3 to 133.3 Pa) are obtained and interpreted. Spectral and internal probe studies were performed on MPX Mk.I and Mk.II devices, respectively. IR spectra were acquired in the Mk.I device for argon and xenon. While triple probe studies on hydrogen, helium, argon, and xenon were performed in the Mk.II device.

Time-resolved electron temperature estimates for argon and xenon during the discharge time frame of 0 to 23 μs are obtained post-process via line intensity ratio methods. Experimental intensity ratios are compared with those of steady-state corona and collisional-radiative model assumptions. Electron temperature estimates were highly model dependent with the steady-state corona model yielding temperatures of around 10 eV or less and the collisional-radiative model yielding up to 100 eV.

Triple probe measurements provide both time- and radially-resolved electron temperature and density estimates for all four gases. Electron temperatures are seen to be limited to 20 eV on average with ionization fractions of up to 28%. In addition, probe currents show substantial evidence of a high charge density wave translating radially inward with speeds approximately given by the ion acoustic wave speed.

Finally, energy analyses of the triple probe results are performed and compared against circuit modeling efforts made previously on the same test article. Peak energy in combined electron heating and ionization accounts for on average around 25% of total dissipated circuit energy due to plasma. With the exception of xenon in which 40 to 90% was accounted for.

ACKNOWLEDGMENTS

Professionally, I would like to acknowledge and give thanks to my advisor, Dr. Joshua Rovey, for his patience and guidance throughout my graduate studies. To the Office of Graduate Studies, former Chancellor Carney, and Chancellor Schrader for providing the Chancellor's Fellowship program and allowing me the opportunity to pursue this dream. And to my committee members Dr's Gao, Castaño, Tsai, and Kovaleski for helping me to realize my goal of reaching the peak of my education potential.

Personally, I would like to thank George and Pati Green for the kindness they have shown me and my family and for their enduring support and encouragement during the whole of my graduate studies. I would also like to thank Stephanie Green and Ryan Pahl for the same.

Finally I have to praise my wife for putting up with so many late nights at work and my lack of patience at times. All while being a great mom. Jamie, after over ten years your love and devotion to me and my dreams is evident everyday and continues to give me strength. Thank you.

This work is dedicated to my parents, David and Kathy Meeks, who did not live to see this achievement but who's pride in me I continue to cherish and who's encouragement I continue to hear. I love you both so much.

-Warner

TABLE OF CONTENTS

SECTION

LIST OF ILLUSTRATIONS

LIST OF TABLES

NOMENCLATURE

$\bar{V}_r$	radial wave speed approximated by probe current ($\frac{\mathrm{m}}{\mathrm{s}}$)
η_{jk}	escape factor of the j^{th} to k^{th} transition emission
λ_D	Debye length (mm)
λ_{ie}	ion-electron mean free path (cm)
λ_{ji}	emission wavelength for the j^{th} to i^{th} state transition (nm)
μ_0	permeability of free space ($= 4\pi \times 10^{-7} \frac{\text{V-s}}{\text{A-m}}$)
ν	collision frequency (s^{-1})
σ	collisional cross-section (m^2)
τ_j	j^{th} metastable state diffusion time (s)
A_{ji}	spontaneous decay rate (Einstein Coefficient) from the j^{th} to i^{th} species (s^{-1})
d_s	sheath thickness (mm)
e	elementary or fundamental charge ($= 1.6 \times 10^{-19}$ C)
E_{iz}	first ionization potential of species (eV)
h	Plank's constant ($= 6.63 \times 10^{-34}$ J-s)
$I(\lambda_{ji})$	emission intensity of the j^{th} to i^{th} state transition (counts per m^2)
k_{B}	Boltzmann's constant ($= 1.38 \times 10^{-23}\ \frac{\mathrm{J}}{\mathrm{K}}$)
Kn	Knudsen number
m_e	electron mass ($= 0.91 \times 10^{-30}$ kg)
M_i	ion mass ($\approx M_0$, kg)
n_0	ground state number density (m^{-3})
n_e	electron number density (m^{-3})
N_j	number density of the j^{th} species (m^{-3})
r_p	probe radius (mm)
s	tip separation distance (mm)

T_e	electron temperature in Kelvin (K)
T_{eV}	electron temperature in volts (eV), NOTE: $k_{\mathrm{B}}T_e = eT_{\mathrm{eV}}$
V_p	probe potential (V)
V_s	space (plasma) potential (V)

1. BACKGROUND AND APPROACH

1.1. PULSED INDUCTIVE PLASMA THEORY

Pulsed inductive plasma (PIP) devices such as the theta-pinch coil used in the following work are an electrode-less type of plasma source often used at high energies in both research and industry[1–7]. A brief analysis of the fundamental physics involved in cylindrical PIP devices such as that used here is provided. As a starting point one considers a known amount of electrical energy stored in a capacitance, C, at a voltage, V, to give a total energy stored of $\frac{1}{2}CV^2$. Additionally, the capacitor is electrically connected in series via an ideal switch with a conductive structure that, by some geometric means forms a complete circuit back to the capacitor's opposite terminal. This complete circuit is collectively referred to as the device. If this switch is then closed current will begin to flow in an effort to reduce the potential difference across the capacitor and return it to equilibrium (zero voltage). In the absence of a plasma gas, electromagnetic fields within the device are governed exclusively by Maxwell's laws. An excellent review of the fundamentals of electrodynamics can be found in Griffiths (1999) and a summary of the laws critical to this work are as follows; Amp-Maxwell's law written for free-space describes the axial magnetic field that is induced in vacuum due to current flowing in the inductive coil[8],

$$\oint \vec{B}(t) \cdot d\vec{l} = \mu_o \int \vec{J} \cdot d\vec{A} + \mu_o \epsilon_o \frac{\partial}{\partial t} \int \vec{E} \cdot d\vec{A} \ . \tag{1.1}$$

Of note is that the magnetic field, $\vec{B}(t)$, is directly proportional to the current flowing in the device, $\vec{I}(t)$. If the geometry is assumed to be an infinitely long conductive cylinder of zero resistance and of turns, n, per unit length (1.1) leads to,

$$B(t) \quad = \quad \mu_o n I(t) \tag{1.2}$$

inside the cylinder. Thus, the magnetic field inside this idealized *solenoid* is not spatially dependent and is uniform through the inner diameter. Two sometimes sizeable effects this solution neglects are the end effects of a cylindrical geometry of real length, L, and the azimuthal asymmetry brought on by the physical connection of transmission lines. As a time-dependent magnetic field is now present in the device Faraday's law of Induction comes into focus describing the azimuthal or circular electric field induced due to a time-varying magnetic field,

$$\oint \vec{E}(t) \cdot \vec{dl} = \frac{-\partial}{\partial t} \int \vec{B}(t) \cdot \vec{dA} \tag{1.3}$$

Briefly one might return to (1.1) with the realization that the electric and magnetic fields are coupled, and this would be a correct assessment. However, a quick order-of-magnitude check to the coefficient pair $\mu_0 \epsilon_0$ yields a factor of 10^{-17} greatly diminishing electric field coupling in dielectric materials. Returning to the ideal solenoid geometry (1.3) leads to,

$$\begin{aligned} 2\pi r E(t) &= \frac{-dB(t)}{dt} \pi r^2 \\ \text{or} \qquad E(t) &= -\frac{r}{2} \frac{dB(t)}{dt} . \end{aligned} \tag{1.4}$$

Thus in a cylindrical PIP device absent any plasma species one would expect the internal electric field to be a maximum at the outer most internal radius which leads to the inductive coupling taking place primarily just inside the coil. Also and have a time-varying peak when the *change* in magnetic field with time is highest. Remembering that the magnetic field is directly proportional to discharge current leads to a recognition that $|\vec{E}| \propto f_{discharge}$. If the notion of charged species is now introduced the Lorentz Force law governs the motion of these species in a collisionless regime,

$$\vec{F} = q \cdot (\vec{E} + \vec{V} \times \vec{B}) \tag{1.5}$$

Figure 1.1 shows the ideal solenoid field topology during positive dI/dt.

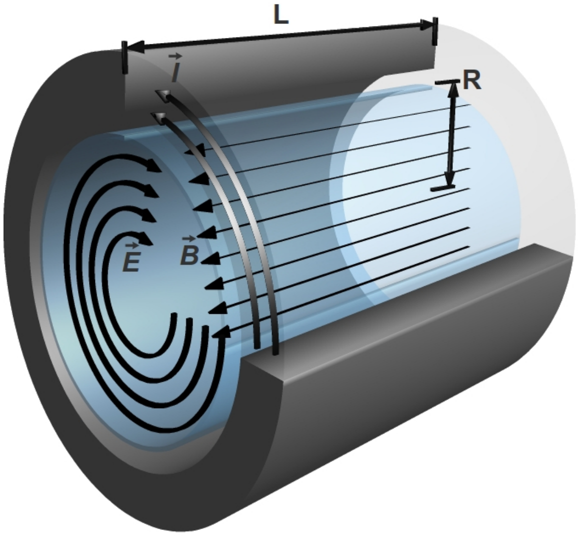

Figure 1.1. The field topology of an ideal solenoid coil geometry of length, L and radius, R, with increasing (positive) coil current. Note the azimuthal current & electric fields, $\vec{I}$ & $\vec{E}$, respectively and axial magnetic field, $\vec{B}$.

1.2. PREVIOUS WORK IN THE FIELD

In recent years, PIP devices currently being investigated by the fusion and space propulsion communities utilizing mostly deuterium and xenon, respectively, have provided promising new results. Detailing effective timing of pre-ionization stages[9, 10], iterating through various coil geometries and ionization techniques[5, 11–16], and refining high speed switching capabilities [17], a large volume of work has been put towards pulsed inductive plasma utilization. Additionally, numerical analysis of these devices has given some understanding of the field topology[18] and optimal electrical circuit characteristics for peak inductive coupling[19–21]. Despite this, efforts to differentiate and quantify the various modes of energy that arise during and after the inductive process are lacking.

1.3. PREVIOUS WORK WITH MPX

The Missouri Plasmoid Experiment (MPX) is a theta-pinch configuration pulsed inductive plasma device and the original Mk.I test article came online in 2011 with a Mk.II test article following in 2014. Work by Pahl and Rovey involved magnetic field sensing via B-dot probes, energy analysis via circuit modeling, and pre-ionization studies[22–24]. Culminating in a doctoral thesis, energy lost by the circuit due to plasma in that work was partitioned into either inductive or resistive loads, with transfer to inductive energy being a reversible process and to resistive (joule) heating being a non-reversible process. It was reported that inductive energy into xenon was highest at 8.4% of initial MPX energy (6.4 of 79.2 joules) followed by argon then hydrogen[21]. This inductive energy was seen to decrease with higher pressures up to 100 mTorr. Non-reversible energy loss by resistive heating is seen to dissipate 16 to 20 joules from 10 to 100 mTorr in argon with hydrogen and xenon following a similar trend. Also reported in that work was that the highest resistive losses were in xenon at lower pressures (10 to 60 mTorr) and in hydrogen at higher pressures (60 to 100 mTorr). Comparison with the findings of that work will be made here in subsequent chapters.

1.4. CONTRIBUTION OF THIS WORK

As mentioned above pulsed inductive devices typically start with a stored capacitive energy. However, once discharged and by the end of the operational discharge cycle that energy has been divided among radiative losses (light emission, stray capacitance/inductance, etc.), joule heating (of the device, plasma, and neutral gas), unusable directions in bulk fluid motion (via poor containment or undesired expansion upon expulsion), and collisional processes. These collisional processes can be divided further still into numerous electronic modes, many of which do not provide a direct path to ionization. The net effect of these collective losses is an increase in ionization cost and a reduced effectiveness of the device.

Specifically within the aerospace community, high power pulsed inductive in-space electric propulsion concepts have faced three major hurdles in the last few decades keeping them firmly on the drawing board and in the laboratory rather than on a spacecraft. These are; 1.) power sources on the order of 10's to 100's of kilowatts, 2.) high-speed, high-power charging and switching technologies, and 3.) performance and efficiencies comparable to, or better than, those of state-of-the-art electric propulsion systems in use now. NASA has acknowledged and is addressing the first of these hurdles through several initiatives. The second of these is being researched heavily from a number of groups in industry and academia, some of which were mentioned in Section 1.3. While the third has seen limited attention. This is partly because the relationships between the discharge energy cost (i.e., ionization cost) and the factors shown to affect it are not well understood. Specifically, factors such as the inductive device geometry, discharge frequency, operating pressure, and the use of heavy gases suitable for electric propulsion have all been found to have a role in the performance and effectiveness of these pulsed inductive plasma devices.

To this end, the present work has utilized both external and internal diagnostic techniques to interrogate a simple geometry pulsed inductive plasma and quantify some of the primary energy modes that occur throughout and after a discharge cycle. Parametric analyses focus primarily on variation of operating pressure and gas species.

1.5. APPROACH

Using a cylindrical geometry pulsed inductive device design plasmas generated in a variety of gas species and operating pressures are interrogated using multiple diagnostic techniques. First, spectral analyses of plasma light emission in the near infra-red (near-IR) range are performed using collisional-statistic modelling to obtain time-resolved electron temperature profiles. Second, current analyses using internal triple probe diagnostics are performed to obtain additional time-resolved electron temperature as well as electron density profiles. Some general volumetric partitioning is then used and total energies entrained in ions and electrons are quantified and discussed.

2. TEST ARTICLE, FACILITIES, AND DIAGNOSTICS

2.1. THETA-PINCH DEVICE

2.1.1. MPX Mk.I Coil. The Mk.I coil is constructed from a rolled sheet of 1.5 mm thick copper and spans approximately 83% of the evacuated length at 76.2 cm (30 in) and has an inner diameter of 17.8 cm (7.0 in). A photo of the Missouri Plasmoid Experiment (MPX) Mk.I device with call-outs can be seen in Figure 2.1.

2.1.2. MPX Mk.II Coil. The Mk.II coil is a 11-segment design constructed from milled billets of aluminum assembled in parallel with an inner diameter equal to that of the Mk.I of 17.8 cm and a slightly increased length of 78.4 cm (30.8 in). An equal inner diameter to that of the Mk.I design matched with the same quartz tube ensures the best chance for an equal amount of coil to plasma coupling between the designs. To provide some confidence in achieving this goal main current discharge profiles in vacuum are compared and can be seen in Figure 2.2. The MPX Mk.II test article can be seen in Figure 2.3.

2.1.3. Discharge Circuit. The discharge circuit consists of a single Maxwell Technologies 0.7 μF, 70 kV rated high-energy capacitor with a 0.05 μH series inductance and a Perkin-Elmer GP-14B spark-gap trigger with maximum hold-off voltage of 36 kV. Charge voltage on the capacitor was maintained at 15 ± 0.02 kV for all tests. A DC glow discharge electron source, commonly referred to as a type of pre-ionization source, was placed at one end of the discharge chamber out of the line-of-sight of the optical emission pick-up and at least 30 cm (12 in) from triple probes to assist with reliable plasma formation at all tested conditions. The DC source was maintained at approximately 500 volts and was current limited to 1 milliamp. Upon transitioning to the Mk.II design this DC source was continued and placed in a similar location to maintain continuity between designs. Figure 2.4 shows two typical current discharge profiles to highlight the deviation from vacuum when plasma

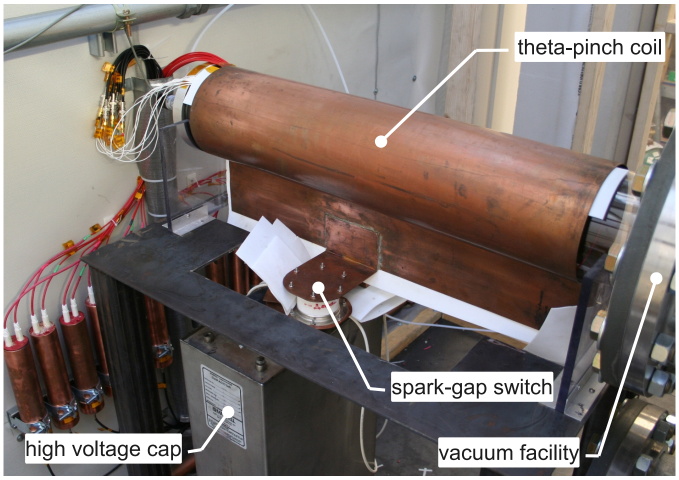

Figure 2.1. Missouri Plasmoid Experiment Mk.I rolled copper sheet single-turn coil design.

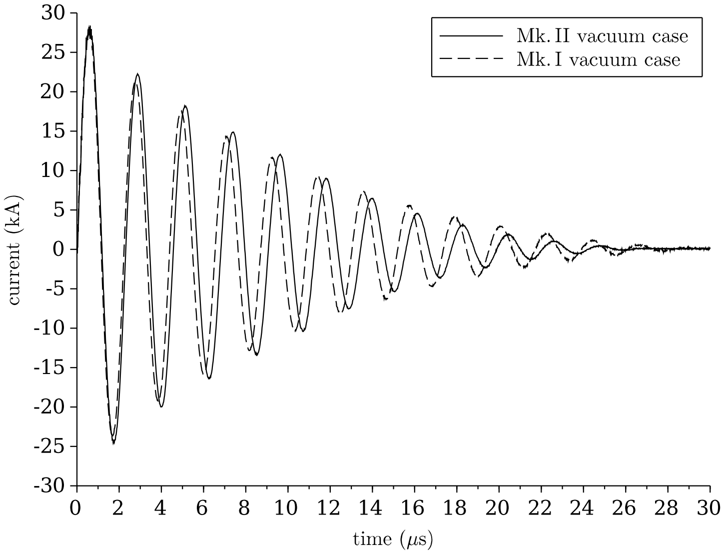

Figure 2.2. MPX Mk.I and Mk.II currents compared to show comparable frequencies and amplitudes.

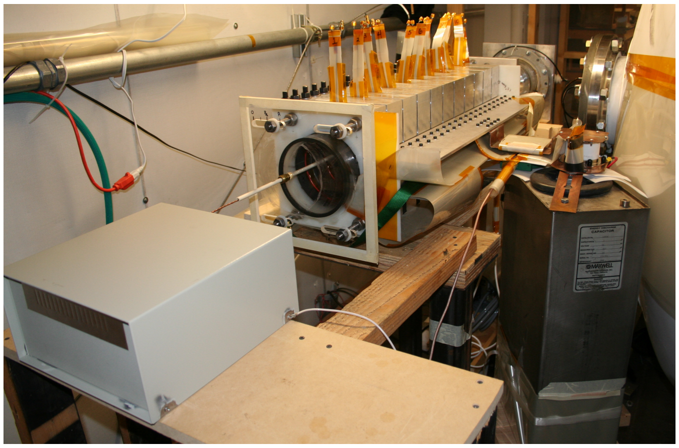

Figure 2.3. Missouri Plasmoid Experiment Mk.II segmented single-turn coil design along with integrated probe assembly.

is present. Attenuation due to mutual inductance can be observed when plasma is present, and this is a well-known effect observed in similar devices[25, 26]. This mutual inductance affects the discharge profile two-fold; 1.) it reduces the LRC time-constant decaying the discharge earlier and 2.) it increases the discharge frequency. Performing Fourier analysis on all discharge current profiles reveals that the discharge frequency at base pressure is 462 kHz while pressurized discharge frequencies where plasma is present average 490 kHz. MPX Mk.II showed a slight decrease in characteristic frequency with plasma to around 460 kHz.

2.2. MAIN VACUUM FACILITIES

2.2.1. Large Vacuum Facility. Spectroscopy and triple probe studies were performed using different vacuum pumping facilities. During spectroscopy studies the MPX cylindrical quartz vacuum vessel was connected at one end to a much larger cylindrical vacuum chamber of length 3 m (10 ft) and diameter 1.8 m (6 ft). This large chamber was pumped using up to four 0.8 m (32 in) Varian diffusion pumps backed by a 2-stage (Edwards EH-4200 roots-blower → Tokuda KP-7500BG rotary-vane) roughing pump. The

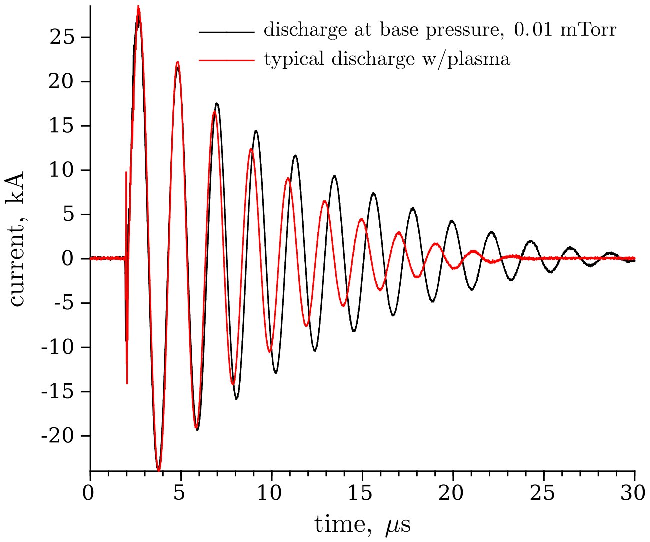

Figure 2.4. Typical MPX Mk.I discharge profiles with and without plasma. Time zero represents when the data acquisition system received its trigger subsequently showing a delay of around 2 µs before capacitor discharge.

large vacuum facility can be seen in Figure 2.5 and achieves a base pressure of 10^{-6} Torr monitored with a Adixen (model: ACC2009, cold cathode+Pirani) full-range gauge. The 2-stage roughing pump can be seen in Figure 2.6. During backfill to operational pressures in MPX Mk.I the quartz tube was isolated using an aluminum plate attached via armature to a translation stage located within the larger chamber. When sealed the quartz tube maintained a vacuum of less than 0.1 mTorr. MPX quartz tube pressures were measured directly with an MKS capacitance manometer (baratron model: 626, range: 10^{-5} to 10^{-1} Torr) as shown in the upper-right of Figure 2.3. Additionally, gas species of interest in this work are detailed in Table 2.1 and backfilled using an Alicat Scientific 0 to 20 sccm flow controller.

2.2.2. Small Vacuum Facility. In the interim between studies the decision was made to disconnect the quartz tube from the large chamber and pump it directly with a separate smaller pump combination. Which consisted of a Adixen MDP-5011 molecular drag pump backed by a Edwards 3-Series rotary-vane roughing pump. This new configuration can be seen in Figure 2.3 and the corresponding pump combination in Figure 2.7.

Figure 2.5. Large main chamber with diffusion pumps (seen in green) supporting MPX Mk.I. MPX quartz tube connected via a center port (18 inch diameter) at the rear.

Figure 2.6. 2-stage roughing pump backing of high vacuum diffusion pumps. Upper left: roots-blower. Lower-right: rotary-vane pump.

Table 2.1. Gas species characteristics used in this work.

gas species	H_2	He	Ar	Xe
weight, M_i (10^{-27} kg)	3.35	6.65	66.3	218
1^{st} ionization pot. (eV)	15.44 (diatomic)	24.59	15.76	12.13

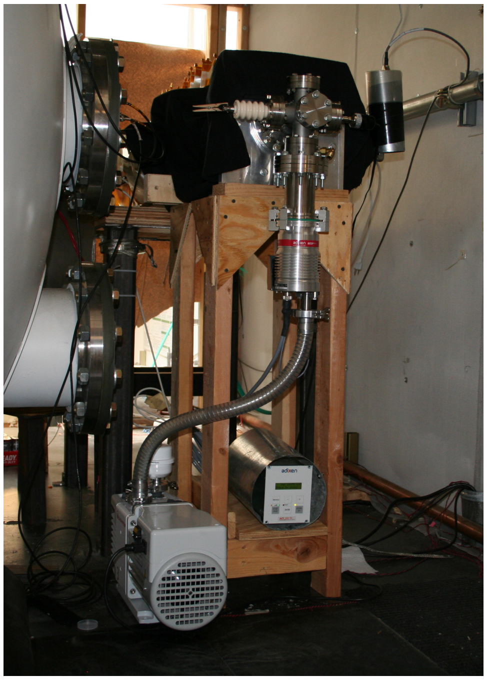

Figure 2.7. Small pump combination located downstream of the Mk.II device (in the upper-right corner of Figure 2.3).

2.3. EXTERNAL DIAGNOSTICS

A number of plasma interrogation techniques have been pioneered and refined over the last roughly half century[27–38]. Two primary diagnostics are utilized in this work. Namely, spectroscopy (an external diagnostic) and electrostatic probes (an internal diagnostic).

2.3.1. Czerny-Turner Spectrometer. A Princeton Instruments SP-2356 Czerny-Turner (C-T) spectrometer with a 0.3 m focal length, triple grating turret with gratings of 300, 1200, and 2400 g/mm, and a 14 mm high slit with width adjustable from 10 µm to 3 mm was borrowed from the Energetics and Pulsed Power Laboratory group at the University of Missouri - Columbia campus. Grating and slit width used here were 300 g/mm and 50 µm, respectively, yielding a spectral resolution of 0.134 nm per pixel. Interfaced with the spectrometer was a PI-MAX intensified CCD camera with a 1024 by 1024 pixel array

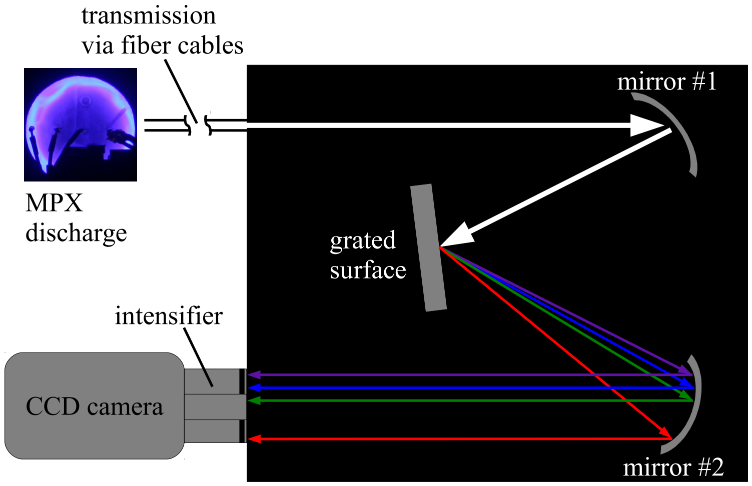

Figure 2.8. Basic Czerny-Turner spectrometer operation with MPX as the light source lacking certain wavelength bands.

and a ST-133 controller with built-in PTG trigger module for repetitive (used in this work) or sequential external triggering. Basic C-T spectrometer operation is detailed in Figure 2.8.

2.3.2. Optical Transmission. Light emission was transmitted from the experiment to the spectrometer slit via a 7.5 m long, 200 µm core, VIS/NIR (low OH) Ocean Optics fiber. The fiber was mounted perpendicular to the coil axial direction pointing toward the center of the discharge tube. This optical configuration is similar to that used by Yokota[39]. Figure 2.9 also provides further clarification of this orientation. The spectral band during argon testing was 696 to 834 nm while for xenon testing was 803 to 938 nm.

2.4. INTERNAL DIAGNOSTICS

2.4.1. Probe Assembly. The main probe body is constructed of two sizes of alumina tubing. The first of which is a four-bore 4.8 mm (0.19 in) outer diameter tube and second is a single-bore 8.1 mm (0.32 in) outer diameter tube with inner diameter sized to accommodate the four-bore tube O.D. Alumina (Al_2O_3) is a ceramic based material with

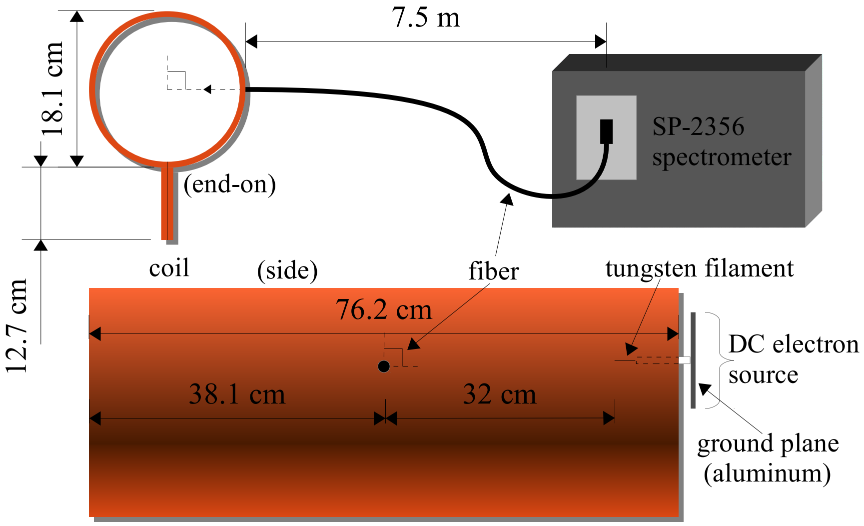

Figure 2.9. MPX Mk.I with single optical fiber to the Czerny-Turner type SP-2356 spectrometer.

non-ablative, non-conductive, and non-reactive attributes ideal for direct exposure environments. To alleviate low signal-to-noise currents by the probe a 0.53 mm (0.021 in) diameter and 8 mm (0.315 in) length tungsten wire was used providing a 13.4 mm^2 (0.021 in^2) surface area for current collection. To mitigate RF pick-up from the fast switching spark-gap and capacitive coupling with the main coil multiple features were built into the probe and accompanying signal output assembly. Minimizing unshielded lengths of wire the probes pick-ups transition quickly into solid-shielded co-axial cable (see Figures 2.10 and 2.11) with a 1 mm diameter copper jacket and 28 AWG (0.32 mm dia.) solid inner conductor. With four wires in total the bundle is then twisted immediately following the tungsten termination to the remaining length of the probe assembly. Figures 2.10, 2.11, and 2.12 provide additional clarification of the probe circuit assembly.

2.4.2. Probe Integration. Integration into MPX was facilitated through a 30.5 cm × 30.5 cm (12 in × 12 in) by 1.27 cm (0.5 in) thick acrylic (dielectric) plate mounted at one end of the device sealed to the quartz tube with a ’L’-shaped rubber gasket and a pressure fit maintained with four bolts. Transition of the probe assembly from vacuum was facilitated

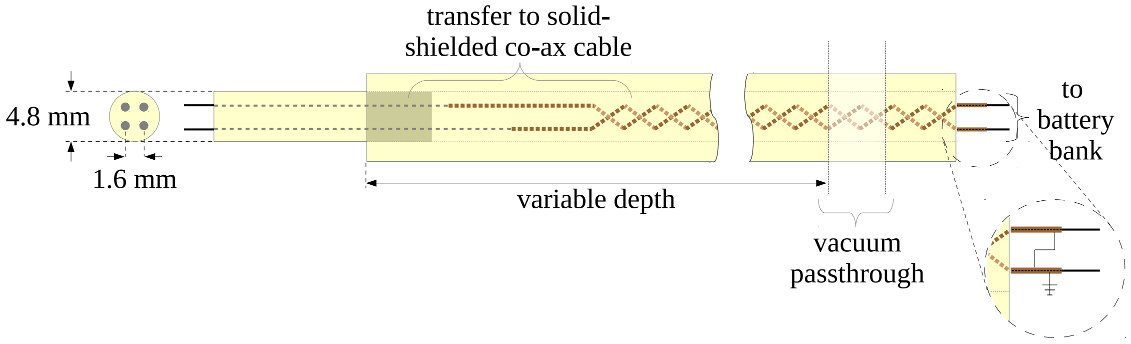

Figure 2.10. Triple probe schematic showing transition to twisted co-ax cable with a shared ground shielding.

through a customized Swagelok-style compression fitting refitted with o-rings (see Figure 2.11) which allows for axial translation of the probe assembly without loss in vacuum down to millitorr levels. Radial translation is afforded through elongated mounting holes at the four bolt locations allowing the entire acrylic plate to slide along the gasket. Both o-ring and 'L' gasket are sealed with Dow Corning high vacuum grease that eases translation while maintaining a seal. As with axial translation, radial translation of the probe can also be done without loss of vacuum. Additionally, the remainder of the probe circuitry along with the battery supplies and dual Pearson model 4100 current monitors are all housed in a mobile conductive enclosure providing direct shielding to ground. Figure 2.12 shows this assembly and integration.

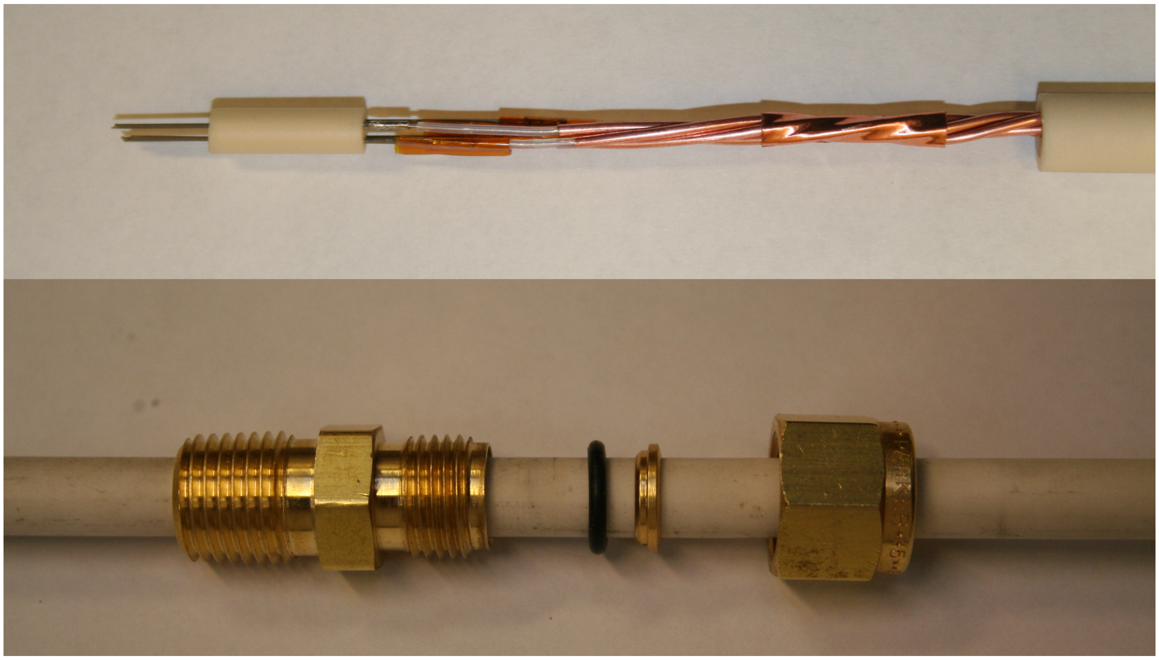

Figure 2.11. Triple probe construction showing transition to twisted co-ax cable before being potted with two-part epoxy along with Swagelok-style vacuum passthrough.

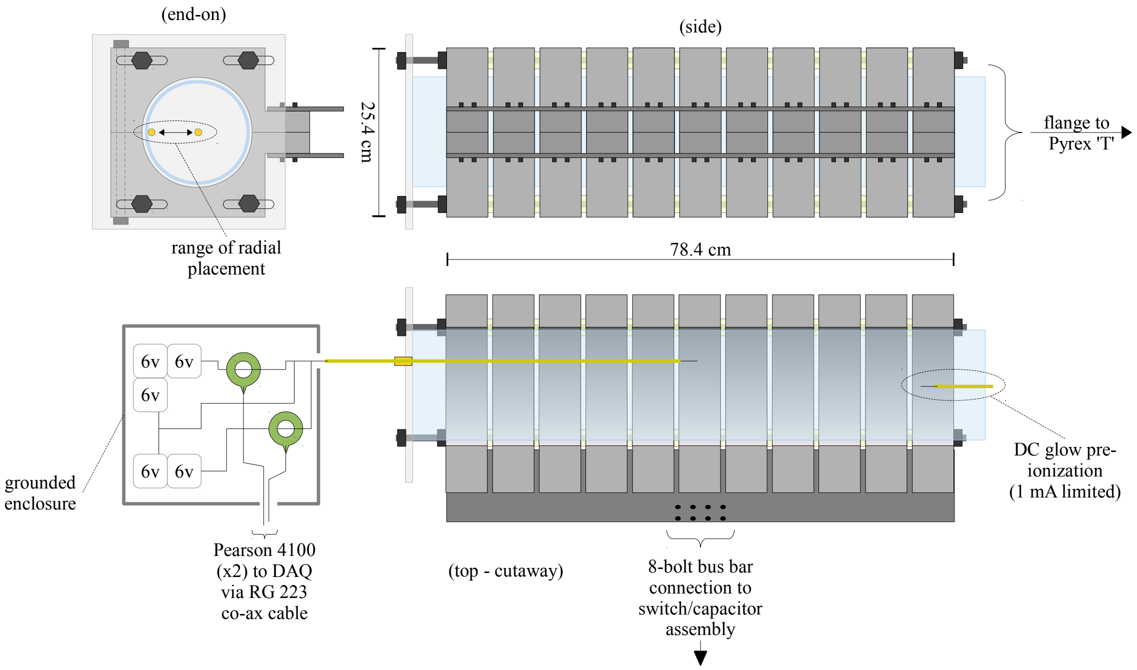

Figure 2.12. Missouri Plasmoid Experiment Mk.II segmented coil design with probe assembly integrated. DC pre-ionization in the Mk.II was purposely placed in a physically similar location to that of the Mk.I testing.

3. SPECTROSCOPY

3.1. SPECTRAL THEORY

3.1.1. Line Emission. Collisions that occur in a plasma can be very broadly separated into two main categories; those in which the total kinetic energy carried by the colliding species is conserved as kinetic energy (i.e., the conservation of momentum), and those in which some amount of the total kinetic energy is lost, or more appropriately, transferred to another energy mode. These categories are referred to as elastic and inelastic collisions, respectively. The latter of these can then be further refined based on the energy mode, or modes, that have been introduced by the collision. Of primary interest here are collisions in which some amount of kinetic energy has been transferred to electronic energy. That is, the collision has increased or *excited* one or more valence electrons orbiting the species of interest. From this point the now excited electron will execute one of two actions. Either it will eventually decay back to it's original energy level, referred to as spontaneous decay, emitting a photon (light emission) with energy equal that of the difference between the excited and original electronic states. Or, if collisions are frequent enough, it may be given further energy to leave the orbit of the parent atom, leaving said atom in an ionized state with charge approximately equal to that of the elementary charge, e ($= 1.6 \times 10^{-19}$ coulombs). If the wavelength, λ, can be observed, energy of the photon can be calculated using Planck's constant ($h = 6.63 \times 10^{-34}$ J-s) and the simple formula,

$$E_\lambda = \frac{hc}{\lambda} \ \text{(J)} \tag{3.1}$$

where c is the unabated speed of light (3.00×10^8 m/s). Dividing by e gives this energy in electron-volts (eV). Figure 3.1 shows estimates of these energy levels in eV's for argon[40].

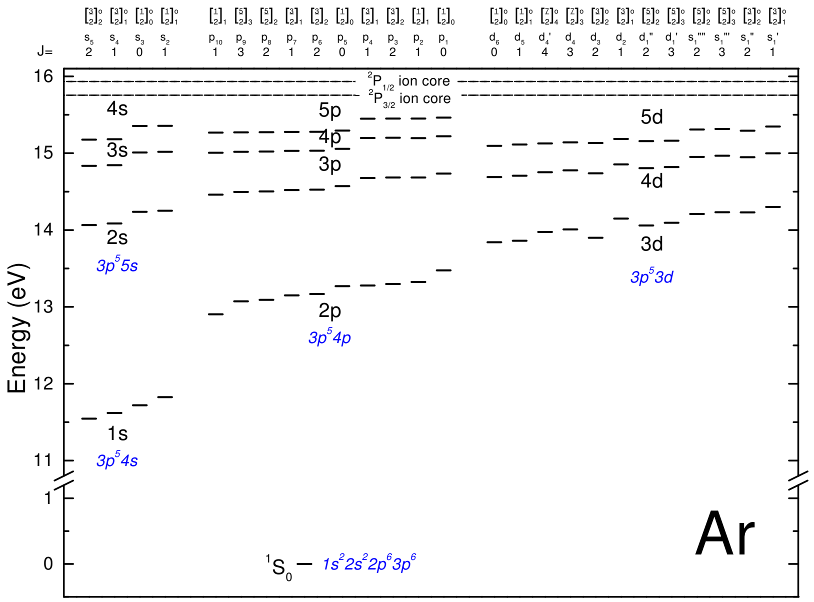

©2002 Atom Weasels

Figure 3.1. Energy level diagram for argon assembled by the Atomic Collisions Group at the University of Wisconsin.

3.1.2. Collisional Statistic Modeling. Modeling based on collisional statistics is most often divided into three broad categories, or regimes, depending on the level of collisionality. These are, from lowest to highest collisional frequency: 1.) Steady-State Corona (SSC) models or simply corona models which assume depopulation of light-emitting species is exclusively by spontaneous radiative decay if species are excited or radiative recombination if species are ionized. 2.) Collisional-Radiative (CR) models which assume depopulation of light-emitting species is done by appreciable levels of both radiative decay and collisional de-excitation. 3) Local Thermal Equilibrium (LTE) models which assume collisional processes dominate and depopulation of all species is governed by the principle of detailed balance. From here models in all three regimes can be further refined to accommodate specific problems of interest. For a complete list of the assumptions and criteria involved in each model a discussion such as that by McWhirter[29] can be found in literature.

3.1.2.1. Coronal Approximation. As a first approximation steady-state corona (SSC) assumptions are used to estimate time-resolved electron temperature via the line intensity ratio technique[29, 41]. In SSC models population of the j^{th} excited state is given by the rate balance equation,

$$\langle\sigma v\rangle_{0j} n_e n_0 = N_j \sum_{i<j} A_{ji}, \tag{3.2}$$

where n_e, n_0, and N_j represent number densities of electrons, ground-state atoms, and the excited species, respectively, $\langle\sigma v\rangle_{0j}$ represents the electron collision rate coefficient (integrated over a Maxwellian velocity distribution) for ground to j^{th} excited level collisions, and A_{ji} is the spontaneous transition decay rate from the j^{th} (upper) level to any i^{th} (lower) level. Intensity (photon counts) of emission through solid angle fraction, $\omega/4\pi$, integrated over plasma depth ds (here ds would be a radial chord; see Figure 2.9) is given by the rate equation,

$$I(\lambda_{ji}) = \left(\frac{\omega}{4\pi}\right)(\tau\alpha)_{\lambda,j\to i} A_{ji} \int N_j ds, \tag{3.3}$$

where $(\tau\alpha)_{\lambda,j\to i}$ is the overall OES transmission efficiency at wavelength λ_{ji}. For spectra obtained along the same collection path and assuming approximately equal transmission efficiencies for transitions $j \to i$ and $k \to l$, combining (3.2) and (3.3) yields for intensity ratio $I(\lambda_{ji})/I(\lambda_{kl})$;

$$\frac{I(\lambda_{ji})}{I(\lambda_{kl})} = \frac{\langle\sigma v\rangle_{0j}}{\langle\sigma v\rangle_{0k}} \frac{A_{ji}}{\sum_{n<j} A_{jn}} \frac{\sum_{n<k} A_{kn}}{A_{kl}}. \tag{3.4}$$

The decay rate fractions are usually symbolically reduced by defining what is referred to as a *branching ratio*, B_{ji} ($\equiv A_{ji}/\sum_{n<j} A_{jn}$). In this work the corona model is applied to the neutral excited state transitions of $2p_2 \to 1s_5$ and $2p_3 \to 1s_4$ (in Paschen notation) for argon. $B_{p_2 s_5}$ and $B_{p_3 s_4}$ are found to be 0.181 and 0.245, respectively. With the assumption of a Maxwellian electron thermal distribution collision rate coefficients can be calculated given well-known argon collision cross-sections. From (3.4) then, intensity ratios as a

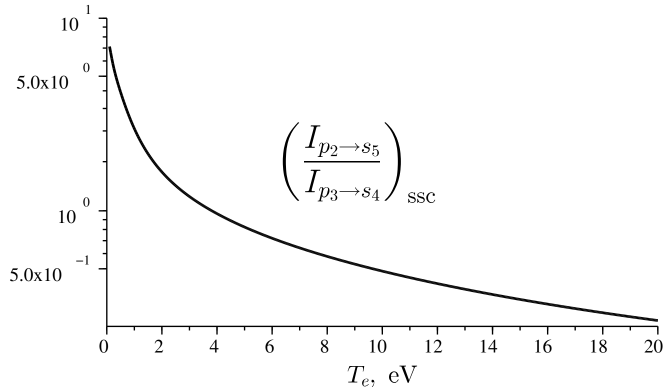

Figure 3.2. Intensity ratio results of the steady-state corona model applied to the transitions $2p_2 \rightarrow 1s_5$ (696.5 nm) over $2p_3 \rightarrow 1s_4$ (738.4 nm).

function of electron temperature may be easily obtained. Figure 3.2 shows this result in the temperature range of 0.1 to 20 eV for the line intensity ratio $I_{696.5}/I_{738.4}$.

3.1.2.2. Collisional-Radiative Approximation. As the background neutral population becomes predominantly ionized corona model assumptions cease to be valid and a new model is required to more appropriately estimate the plasma state. In this work a previously published and well-assessed CR model for argon by Iordanova and Koleva[42, 43] and a CR model developed for use with xenon Hall-effect thrusters (HETs) at the U.S. Air Force[44, 45] are utilized for T_e estimates. The Iordanova model uses numerically obtained collisional cross-sections that have been validated against multiple experimental data sets[46, 47] while cross-sections of backward processes are obtained from the principle of detailed balance. Collisional processes involving the ground state of argon (denoted as the 0^{th} state) as well as the first fourteen (ordered by energy) excited neutral states (denoted 1^{st}-14^{th} states) are included. In Paschen notation these are represented by $1s_{5-2}$ and $2p_{10-1}$. For estimation of electron temperature the Iordanova model uses a cross-point method in which multiple line intensity ratios are plotted verses both temperature, T_e, and electron density, n_e. Plots for two different line ratios are then compared against each other for a common point of intersection, or *cross-point*. To narrow the iterative process necessary to correctly estimate electron temperature generally an approximate range of foreseeable electron density can be made *a priori*. This range is also bounded by those densities applicable to collisional-radiative models. Here this electron density range is taken to be 10^{10} to 10^{14} cm^{-3}.

As done with the SSC model a rate equation is written, here for each of the fourteen excited states, thus necessitating the simultaneous solution of fourteen rate balance (i.e., steady-state) equations. For the j^{th} excited species this rate equation takes the general form,

$$
\begin{aligned}
\overbrace{\sum_{i\neq j}\langle\sigma v\rangle_{i\to j} n_e N_i + \sum_{i>j} A_{ij} N_i}^{\text{populating terms}} \quad = \quad & \overbrace{\left(\langle\sigma v\rangle_{j\to\text{ion}} n_e + \frac{1}{\tau_j}\right) N_j}^{\text{de-populating terms}} \\
& + \sum_{k\neq j}\langle\sigma v\rangle_{j\to k} n_e N_j \\
& + \sum_{k<j}\eta_{jk} A_{jk} N_j \\
& + \sum_{k}\langle\sigma v\rangle_{(kj)\to\text{ion}} N_k N_j \,. \qquad (3.5)
\end{aligned}
$$

Similar nomenclature to that found in the SSC model discussion above is reused here along with new additional terms. Namely these are; the characteristic times of diffusion of metastables to the cylinder walls, τ, and escape factors, η, that represent the re-absorption of light emission based on the level of opacity of a cylindrical plasma slab. The last term on the right hand side of (3.5) represents inelastic collisions leading to ionization. It is emphasized that (3.5) is generalized and for a given species not all terms would be utilized. One example would be (3.5) written for the metastable species $1s_5$ and $1s_3$ would include the diffusion times, $\tau_{5,3}$ but not the spontaneous decay term for de-population (the right-hand side). The latter of these considerations comes by definition of a metastable species in which there is no allowed electron decay directly from these states[48]. For a complete discussion of the terms present per species the reader is referred to the original model publication[42].

3.2. RAW SPECTRAL DATA

Pressures of 10, 30, 50, and 100 mTorr were tested using xenon and argon gases back-filled from less than 0.1 mTorr. It was noted that emission activity tapered off dramatically as back-fill pressure was reduced below around 7 mTorr. Two different data collection schemes were performed at all four pressures for each gas. The first set of data were long-exposures of 20 μs to capture all dominant emission activity over the entire discharge oscillation time. Four to five of these spectra were acquired per pressure and then averaged to provide a measure of consistency. Figures 3.4 and 3.3 show the results of these averaged long-exposures for argon and xenon, respectively. The standard deviation of emission intensity was calculated and a bandwidth averaged standard deviation, $\overline{\sigma}$, can be found in Table 3.1 along with the percentage of maximum intensity each $\overline{\sigma}$ represents per pressure. It will be shown in the next chapter that substantial plasma activity is observable well past the end of the discharge. However, optical studies gave evidence that light emission activity tapered off at or near the end of the discharge by showing negligible further light accumulation out to 30 μs. Despite this, evidence of plasma activity appeared in probe studies out to 100's of μs. Celik et al. have shown in RF afterglow studies with argon that upon power-off a dark period of very low light emission can occur followed by a re-illumination delayed up to 0.5 ms[49]. Given this insight it should be noted that possible light emission in MPX could be occurring long after the end of the main discharge cycle but was not captured in emission studies presented here. Because of this, no MPX spectroscopy studies are available to compare against probe current activity at later times (>20 μs).

The second set of data were obtained to provide a time-resolved intensity profile. This was achieved by fixing CCD gate width (exposure time) to 0.25 μs and delaying gate

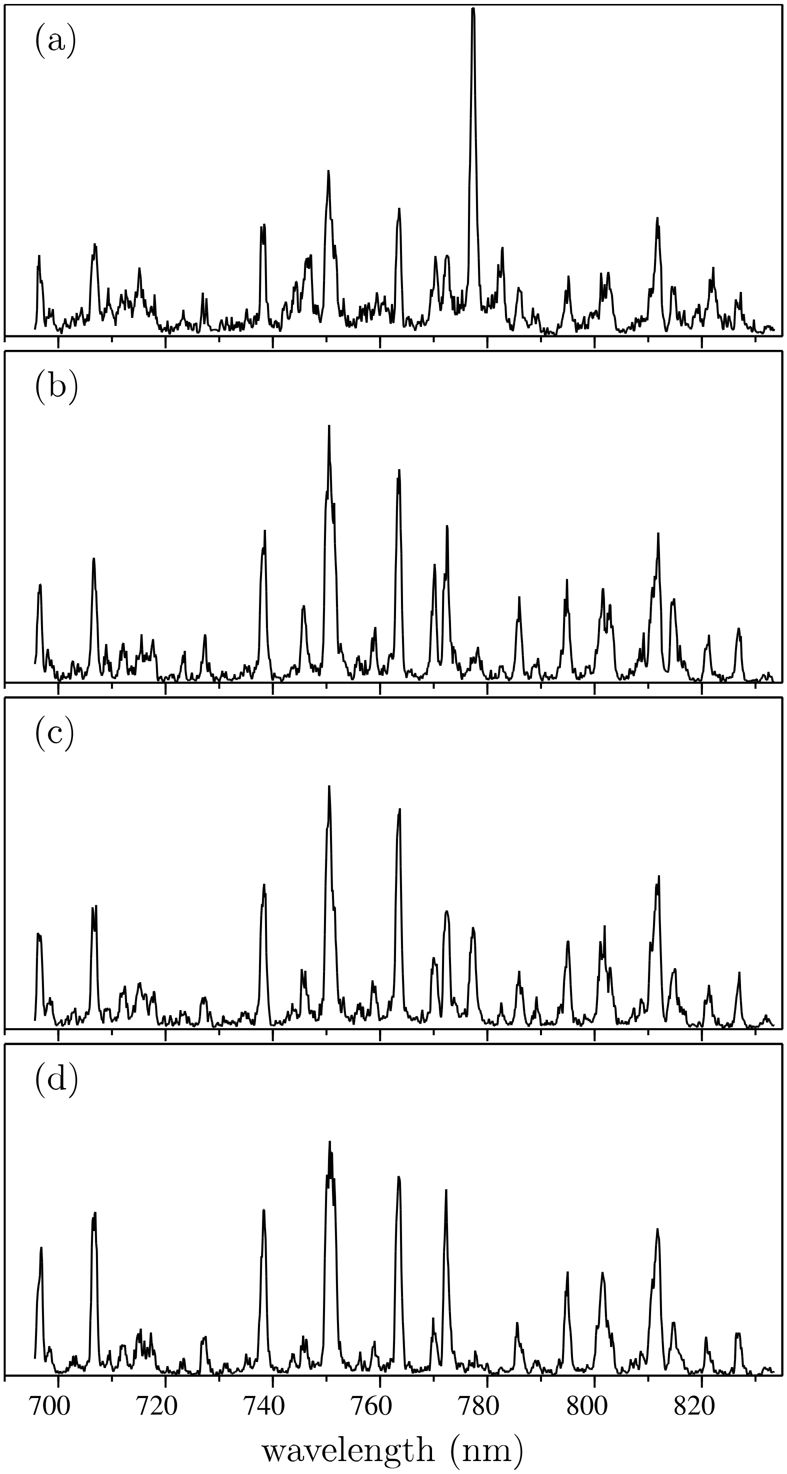

Figure 3.3. (a) 10, (b) 30, (c) 50, and (d) 100 mTorr 20 µs MPX discharge exposures for argon (equivalent vertical scales).

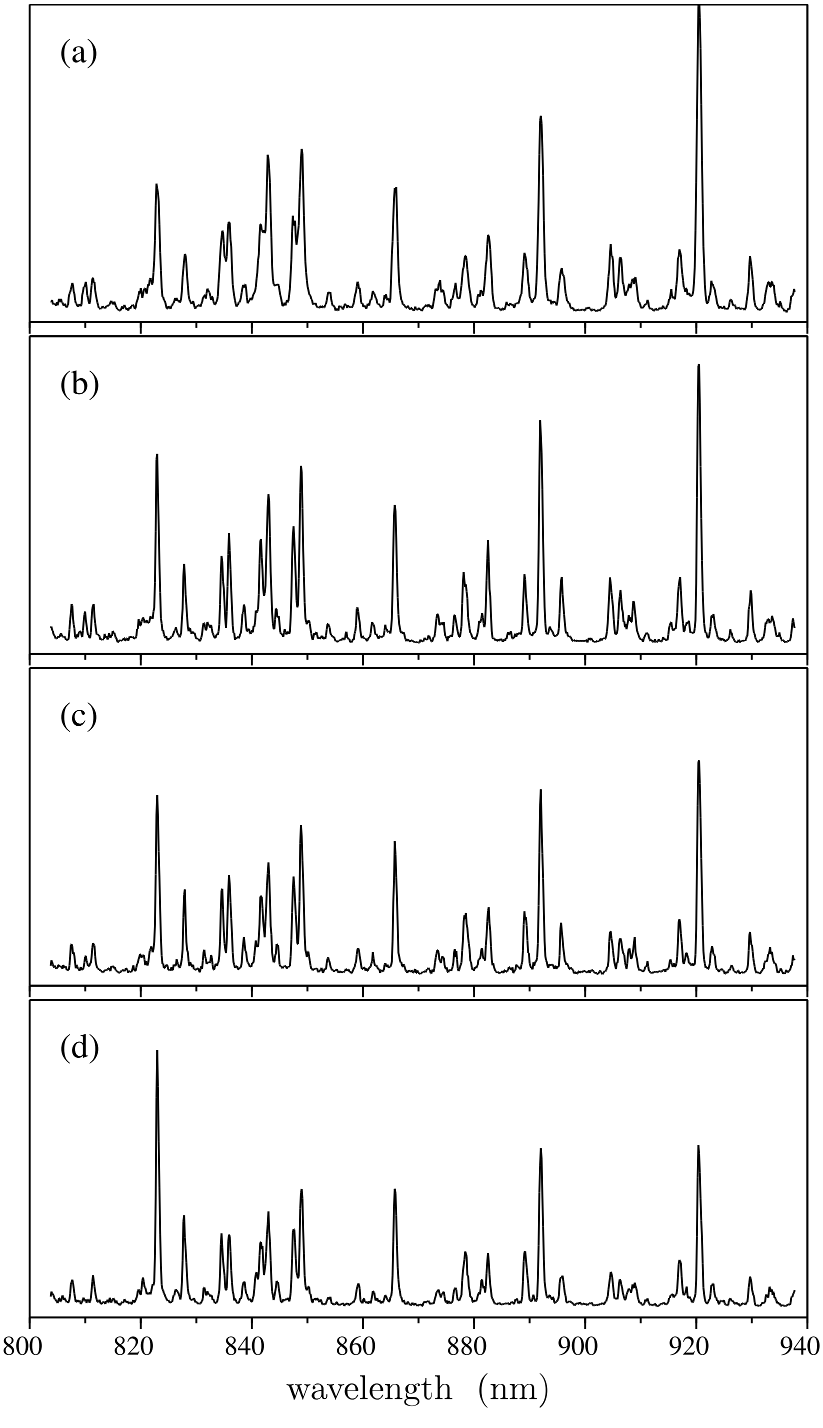

Figure 3.4. (a) 10, (b) 30, (c) 50, and (d) 100 mTorr 20 μs MPX discharge exposures for xenon (equivalent vertical scales).

Table 3.1. Mean shot-to-shot standard deviation, $\overline{\sigma}$ (and its percentage of maximum spectral intensity), for 20 µs exposures seen in Figures 3.4a-d and 3.3a-d.

Pressure (mTorr)	$\overline{\sigma}$ (counts)	% of max int.
Argon:		
10	54.7	1.1
30	44.9	1.2
50	66.7	1.8
100	43.0	1.2
Xenon:		
10	37.8	<1.0
30	47.2	1.4
50	40.3	1.6
100	36.4	1.4

turn-on time starting from the initial trigger, $t_0 \approx 0.0$ seconds and extending to 20 µs. Actual initial start time is approximately 0.03 µs due to machine delay. Thus time-marching a short exposure window forward to build the time-resolved profile. The decision to use 0.25 µs was a compromise due to the low light intensity plasma. At gate widths less than 0.25 µs the light intensity became effectively unusable against the background continuum. The ratio of these intensities against the background continuum is referred to throughout the remainder of this work as the signal-to-noise ratio, or SNR. At each delay time between two and five spectra were acquired depending on whether or not plasma activity was observed. The primary reason necessitating multiple shots per delay time was the presence of a significant temporal jitter (up to ± 100 ns) between discharges attributed to operating the spark-gap switch at only 42% of its maximum hold-off voltage. Unfortunately, this could not be compensated for due to the method of synchronized triggering of both the data acquisition system and spectrometer. Figures 3.5 and 3.6 show MPX spectral emission time-resolved via post-process for argon (750.4 nm) and xenon (823.2 nm) tests, respectively. 10 and 30 mTorr short duration argon tests in Figure 3.5 appear truncated due to unrelated facility issues. Testing was terminated early because of malfunctioning vacuum equipment and unable to be resumed in a timely fashion before returning the spectrometer to UM-Columbia.

Inspection of the 20 μs spectral data shown in Figures 3.3 and 3.4 shows that excited neutrals cannot account for all activity in the bandwidth observed. Two possible sources for the additional emission activity in this bandwidth are; 1.) contaminant spectra from other gas species such as those in air left behind during evacuation, and 2.) second-order spectra from the higher energy UV-band. Second (and higher) order spectra appearing in lower wavelength bands is a very well understood optical effect of using diffraction grating based spectrometry[50]. Both of these possibilities are explored via studies in the UV-band with xenon. Figure 3.7 shows both xenon (b) and air (c) UV-band spectra taken during MPX discharges in 50 mTorr and compares them with the IR-band 50 mTorr xenon spectra (a) from Figure 3.4. Figure 3.7 also provides answers to both earlier questions regarding the added emission activity mentioned above. This is achieved by observing that; 1.) none of the dominant lines in the air spectra appear in the xenon spectra when comparing the two UV-band tests which confirms that the method of backfill was sufficient to remove contaminant species to a negligible level, and 2.) the dominant UV peaks in xenon are clearly repeated at double their respective wavelengths in the IR-band (clarified by the callouts). In addition to the aforementioned repeatability for the IR-band spectra, the UV-band spectra seen in Figure 3.7 consist of three independent data sets each.

From here additional verification of second-order spectra for both argon and xenon is performed by cross-referencing with the National Institute of Standards and Technology (NIST) spectral database for documented lines in both the UV and near-IR bands. Figures 3.8 and 3.9 show overlays of this cross-referencing (blue and red data points) onto the 50 mTorr discharges shown in Figures 3.3 and 3.4 for argon and xenon, respectively. This overlay accounts for all dominant intensities with the exception of a line at 777 nm in argon. This exception is attributed to an atomic oxygen triplet. It was found that a 3 to 5

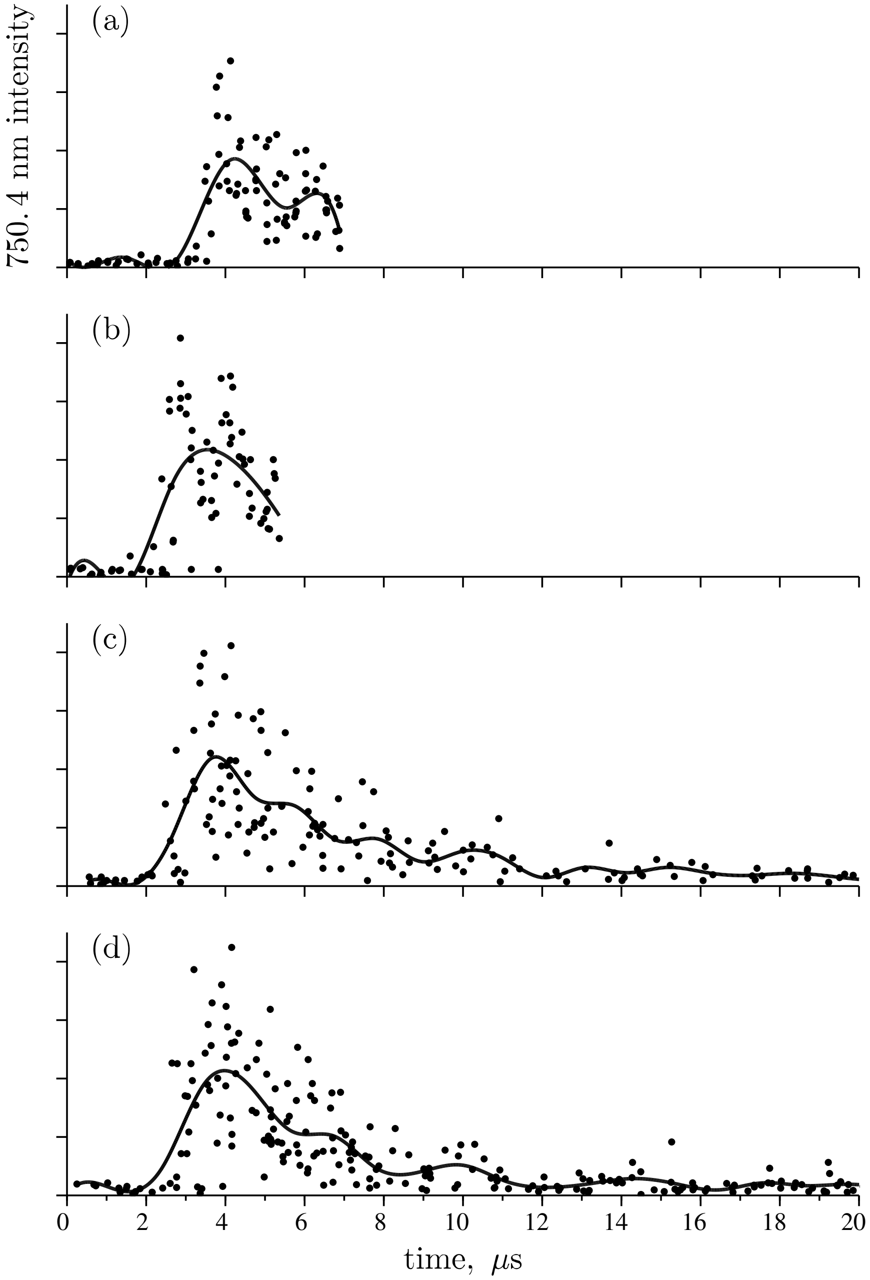

Figure 3.5. 0.25 μs MPX discharge exposures for the 750.4 nm argon line at; (a) 10, (b) 30, (c) 50, and (d) 100 mTorr (equivalent vertical scales).

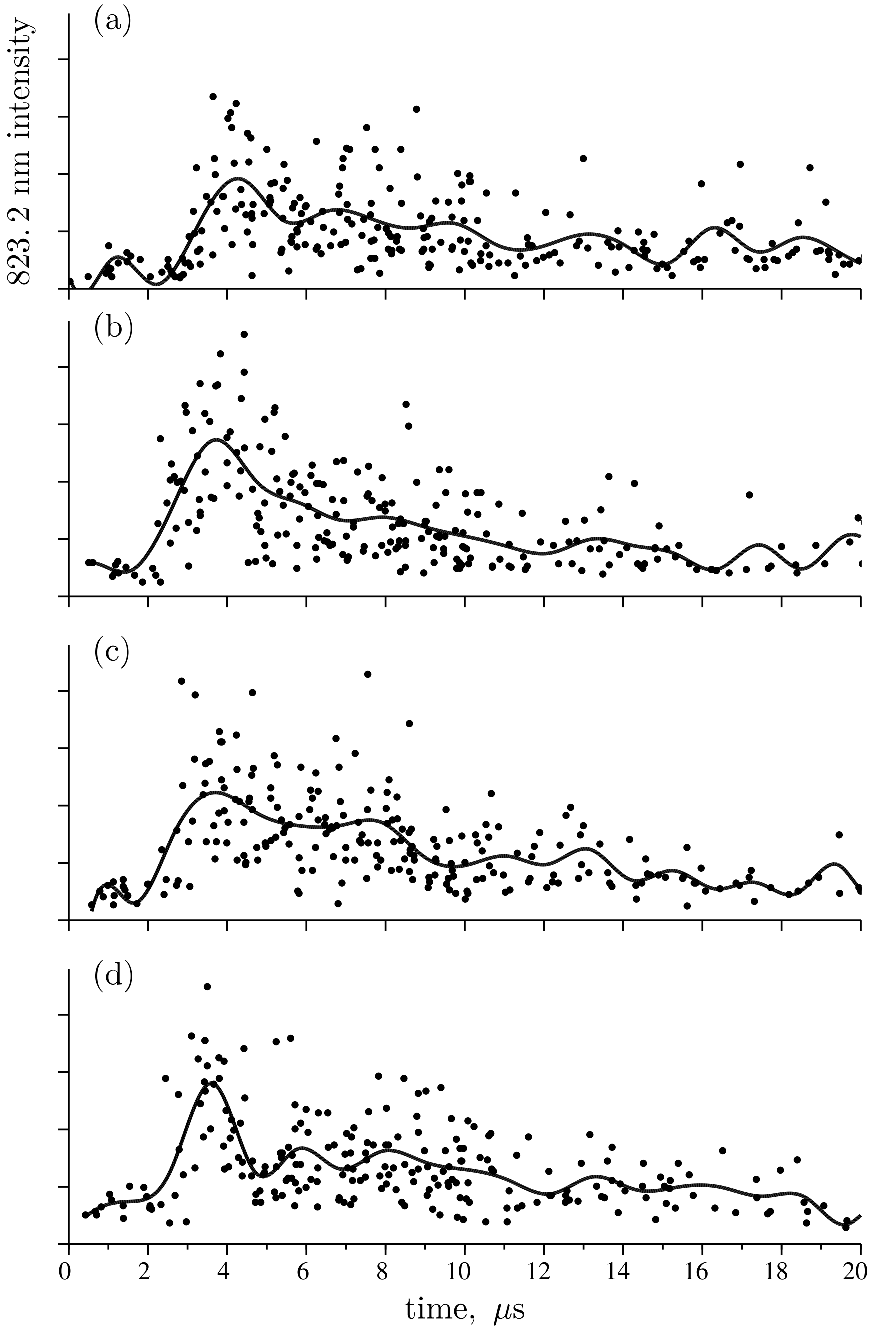

Figure 3.6. 0.25 µs MPX discharge exposures for the 823.2 nm xenon line at; (a) 10, (b) 30, (c) 50, and (d) 100 mTorr (equivalent vertical scales).

shot ‘cleansing’ procedure was needed to remove this contaminant spectra from the data after any re-pressurization of the vacuum facility to atmosphere. This has been encountered before in PIP device operation and is generally thought to be the result of oxygen impurity deposition to the inner walls of the quartz vacuum vessel.

3.3. COLLISIONAL MODELING RESULTS

3.3.1. Corona Model. Time-resolved intensity ratios were compared against the curve shown in Figure 3.2 and subsequent electron temperature estimates can be found in Figure 3.10a along with a reference discharge current in Figure 3.10b. It is noted that temperature profiles in Figure 3.10a do not start at $t_0 = 0.0$. At times earlier than those plotted for each pressure insufficient spectral activity forced unreliable temperature analyses.

3.3.2. Collisional-Radiative Model. Figure 3.11 shows the results of the collisional-radiative approach for discharge pressures of 50 and 100 mTorr. These results are for the cross-point method described in-brief above and in further detail in Ref.[42] applied to the combination $I_{696.5}/I_{738.4}$ and $I_{801.5}/I_{794.8}$. In addition, the SSC results of Figure 3.10a extended to roughly 20 μs and previously published xenon collisional-radiative results are provided for reference. Electron temperature estimates can be seen to range from SSC model minimums of around 1 to 2 eV up to and exceeding 80 eV estimated by the CR model. Gaps in high-level temperature estimates are a result of the experimental intensity ratios falling outside the regime allowed by the CR model. It is speculated that at these times collisional de-excitation greatly dominates over radiative decay processes and the gas is approaching a fully ionized state. Gaps in low-level temperature estimates represent periods where the electron population has shrunk and cooled significantly and collisional processes have fallen off in favor of spontaneous radiative decay.

Results of the CR approximation agree reasonably with results of previous theta pinch experiments of similar conditions using a variety of diagnostic methods[9, 39]. Figure 3.12 shows resulting time-resolved electron temperature from 250 kHz, 1.2 kJ of stored

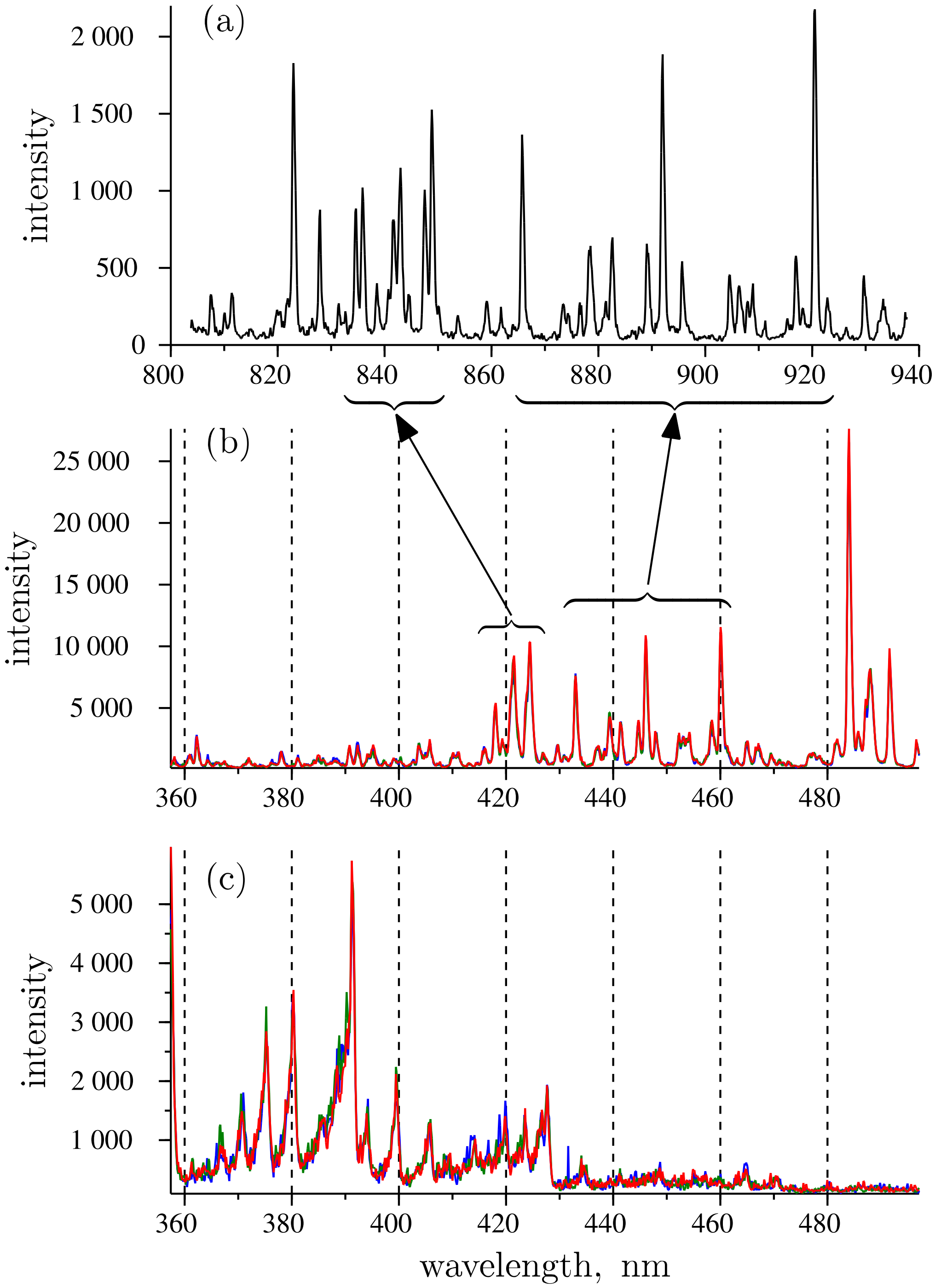

Figure 3.7. (a) 50 mTorr near-IR full discharge spectra (Figure 3.4c). UV spectra (3 sets each) for MPX at 50 mTorr in; (b) xenon, and (c) air. Callouts show the shared spectra in the UV (1st order) and near-IR (2nd order) ranges.

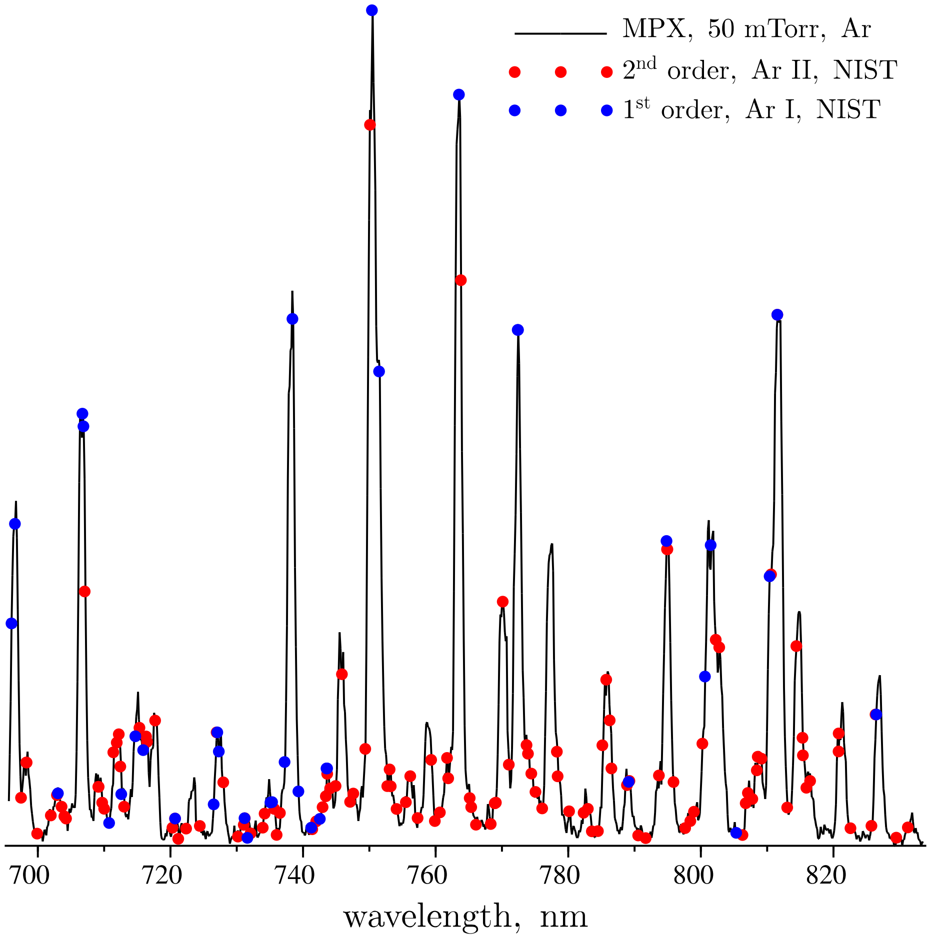

Figure 3.8. 20 µs discharge of MPX at 50 mTorr argon. Dominant peaks are nearly all accounted for by taking into account second order diffraction of Ar II. Second order peaks compiled from NIST data.

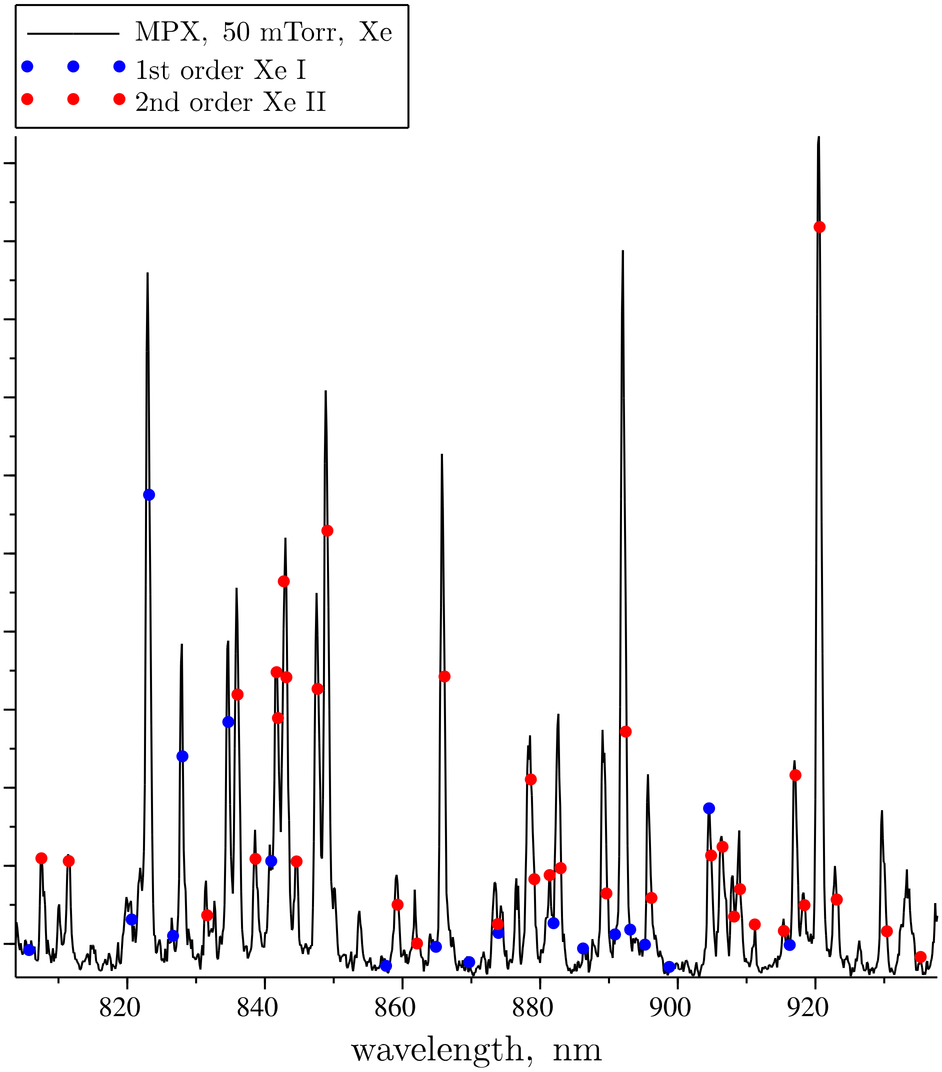

Figure 3.9. 20 μs discharge of MPX at 50 mTorr xenon. Dominant peaks are all accounted for by taking into account second order diffraction of Xe II. Second order peaks compiled from NIST data.

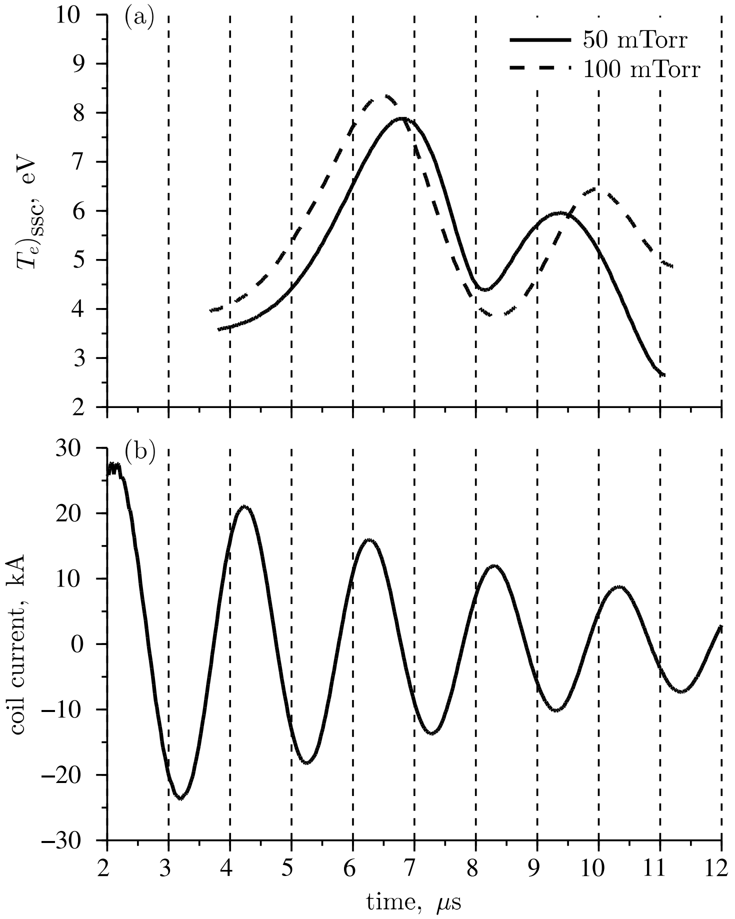

Figure 3.10. Selection of time-resolved electron temperature estimates for MPX at 15 kV (80 J) and 490 kHz based on the argon 696.5 to 738.4 nm transition intensity ratio and steady-state corona model assumptions.

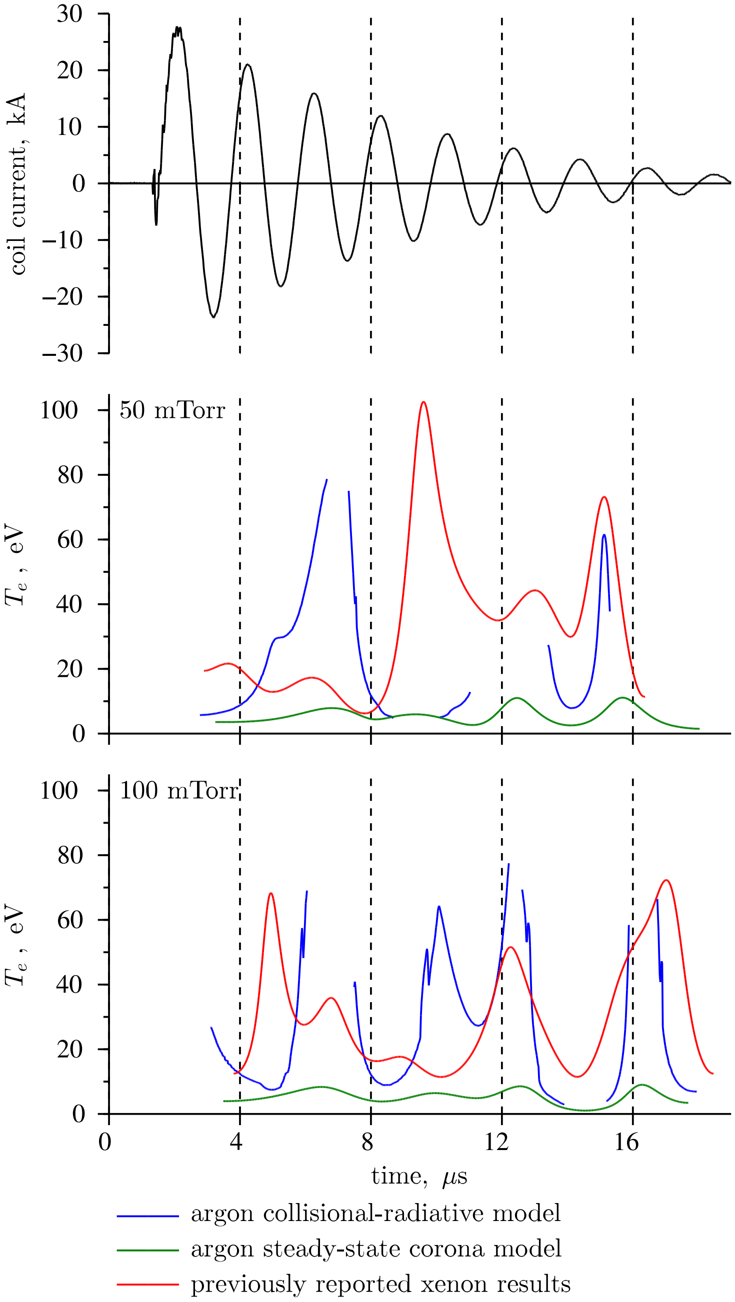

Figure 3.11. Results of collisional-radiative model assumptions along with corona model assumptions of the same data. Previous xenon work also included for reference.

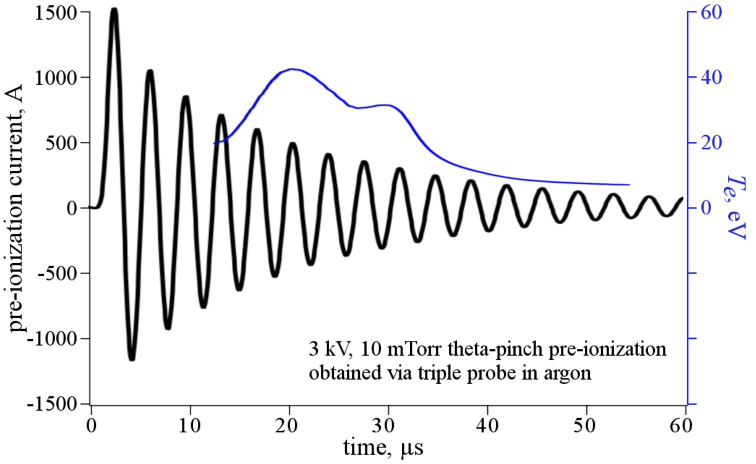

Figure 3.12. Reported data from Ref.[9] on an argon co-axial theta-pinch pre-ionization using a triple probe analysis at 10 mTorr.

energy on a single turn co-axial theta pinch test article. The data shown was taken during pre-ionization testing at a 10 mTorr argon backfill. Electron temperature in Figure 3.12 was arrived at via internal triple probe analysis[37, 51]. Figure 3.13 shows electron temperature estimates in a 100 mTorr slow frequency (15.6 kHz) and high energy (32 kJ) helium theta-pinch discharge[39] overlay onto 100 mTorr MPX data, both as a function of characteristic discharge half-cycles (≈ 1 μs for MPX, ≈ 32 μs for Yokota). The results of Yokota are based on steady-state corona and collisional-radiative models as well. However, the collisional-radiative model used by Yokota is based on experimentally derived (i.e., *apparent*) helium cross-sections rather than numerically derived cross-sections like those used in this work.

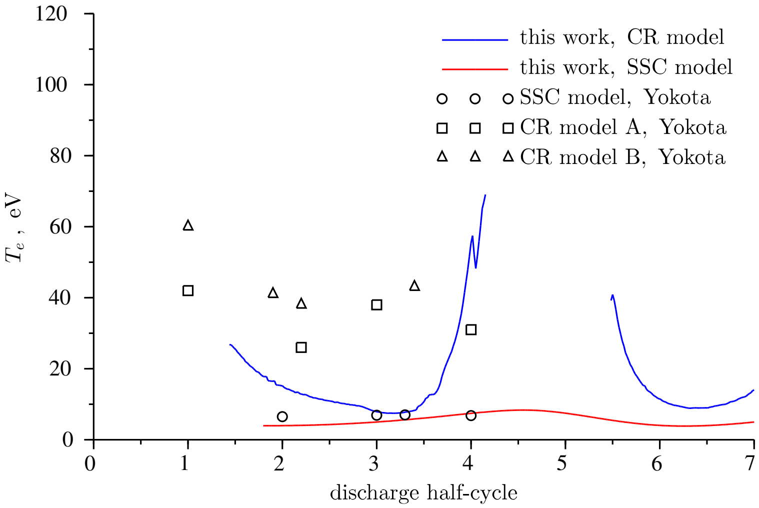

Figure 3.13. 100 mTorr argon work presented here along with reported data from Ref.[39] overlaid as functions of discharge half-cycles.

4. INTERNAL PROBES

4.1. PROBE THEORY

4.1.1. Langmuir Probe Theory. The Langmuir probe is an electrically biased conductor, generally simple in geometry (flat, cylindrical, or spherical), designed to measure numbers of impinging charge carriers in the form of an electric current. Because collection of individual ions and electrons is typically both grossly large in frequency and incredibly small in magnitude, current collected from a Langmuir probe is more readily seen as a *net* total current. The magnitude of which is dependent primarily on the number of charge carriers (plasma density), particle kinetic energies (or macroscopic temperature), and exposed probe surface area. Additionally, gas species can play an implicit role by way of particle mobility and ionization potential. Pioneered by Mott-Smith and Langmuir in the late 1920's[52] the Langmuir probe is one of the most expanded upon and still very much relevant plasma diagnostic tools common across industry, research, and academia today. Extensive analyses of probe current collection theory can be found in texts by Lieberman & Lichtenberg[53], Chen[28], and Hutchinson[54]. Some basic concepts of Langmuir probe current collection are outlined here. While additional concepts specifically relevant to double and triple Langmuir probes are the topics of the next two sections.

The typical current-voltage trace of a cylindrical Langmuir probe can be seen in Figure 4.1 where the convention is to place electron current positive. Addressing Figure 4.1 from left to right, a probe bias voltage, V_{probe} or simply V_{p}, that is very negative will collect predominantly ions, repealing all but the most energetic electrons and yielding what is known as the ion saturation current, $I_{i,sat}$. As the probe is brought close to zero volts the flux of electrons and ions becomes comparable and eventually balance yielding a net zero current by definition at the *floating potential*, V_f, which is the voltage potential an insulated probe would adopt. As electrons are much more mobile than heavy ions a comparably small increase into positive voltages yields large electron currents quickly surpassing ion saturation magnitudes in an exponential fashion. If electrons are assumed to be thermalized, or governed by a Maxwellian energy distribution, this exponential relationship for electron current is given by[55],

$$I_e = I_{e,sat} \exp\Big(e(V_\mathrm{p} - V_s)/(k_\mathrm{B} T_e)\Big) \tag{4.1}$$

where $I_{e,sat}$ is now the *electron* saturation current. Electron saturation current is typically a few orders of magnitude higher than ion saturation and occurs near the plasma (or ‘space’) potential, V_s. Ideally, electron saturation current would be a limit approached asymptotically. However, as voltage is increased the sheath surrounding the probe (typically of a few Debye length, λ_D, in thickness) grows with saturation current following proportionally. Regarding the value of V_s, the random flux of particles from the system favors the light mobile electrons and for plasmas that have access to a grounded conductive surface (e.g. a chamber wall) Chen gives an order of magnitude approximation of $5k_\mathrm{B}T_e$ for V_s[55]. Thus V_s is typically slightly positive due to a mild imbalance in the quasi-neutral assumption. However, it should be noted that there is no defined ‘zero’ probe voltage in Figure 4.1. This is because the location of the exponential transition region in this characteristic is very dependent on both probe and discharge device. Several base assumptions are generally adhered to in Langmuir probe analysis and are also verified to apply throughout this work as well. For cylindrical geometry probe operation these are namely:

1. Probe currents are small compared to discharge current injecting a minimal disturbance.

2. Probe radius is large compared to Debye length.

3. Probe radius is large compared to sheath thickness ($r_p/d_s >> 1$).

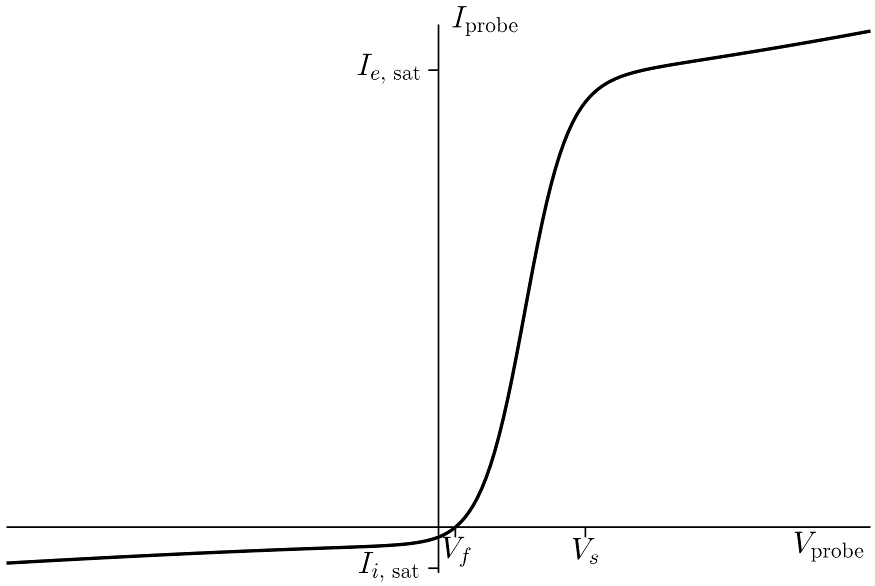

Figure 4.1. Typical I-V characteristic trace of a cylindrical Langmuir probe.

4. Probe radius and therefore sheath thickness is small compared to the dominant collisional mean free paths, primarily λ_{ie} leading to a collisionless sheath ($d_s << r_p << \lambda_{ie}$ or simply $\lambda_{ie}/r_p >> 1$).

5. Electrons are governed by a Maxwellian (thermal) energy distribution.

Table 4.1 summarizes the relevant probe characteristics. Sheath thickness is estimated by[53],

$$d_s = \lambda_D \frac{\sqrt{2}}{3} \left(\frac{2e\phi_{ps}}{k_\text{B} T_e} \right) \tag{4.2}$$

where $\phi_{ps} = V_p - V_s \approx V_p$ is the voltage potential between the probe and the plasma. V_s is assumed to be much smaller than V_p as this work focuses on a dynamic plasma with no close grounded surfaces provided within the chamber. For operating condition calculations the larger bias battery voltage of approximately 20 volts is used to provide a more

Table 4.1. Triple probe design specifications.

diameter, $2r_p$	0.53 mm (0.021 in)
tip length	8.0 mm (0.315 in)
number of probe tips	4 (1 insulated)
tip separation, s	1.6 mm (0.063 in)
collection area, A_p	13.4 mm^2 (0.021 in^2)

conservative estimate. λ_D is the Debye length for a given plasma temperature, T_e, given by,

$$\lambda_D = \sqrt{\frac{\epsilon_0 k_{\mathrm{B}} T_e}{e^2 n_0}}\,. \tag{4.3}$$

Lieberman and Lichtenberg give experimental elastic scattering and charge transfer collision cross-sections, σ, for heavy particle (ion-neutral) collisions in helium and argon as ranging between 2×10^{-16} and 8×10^{-15} cm^2 in the T_{eV} range of 4 to 100 eV. For a general mean free path defined as $\lambda = (n_0\sigma)^{-1}$ and neutral densities ranging from 10^{14} cm^{-3} for 10 mTorr to 10^{15} cm^{-3} for 100 mTorr these cross-section limits yield $10^{-1} < \lambda < 10^{1}$ cm. This puts the lower limit one order above the characteristic probe radius with the upper limit at three orders above, satisfying collisionless sheath criteria. In addition, Table 4.2 summarizes other relevant operating parameters for the estimated bounds of this work. Mean free path for collisions between charged particles ($e^- - e^-$, e^--ion, ion-ion) is given approximately by[56],

$$\lambda_{ie} \approx \lambda_{ee} \approx \lambda_{ii} \approx 3.4\times10^{13}\frac{T_{\mathrm{eV}}^2}{n_0 \ln\Lambda}, \text{ (cm)} \tag{4.4}$$

where the natural log of the impact parameter, $\ln\Lambda$, is assumed to be 10. It can be seen from Table 4.2 that 100 mTorr represents an upper limit for this probe design with higher pressures requiring a smaller probe radius.

Table 4.2. Conditions for valid probe operation.

pressure (mTorr)	10		100	
neutral density (10^{20} m^{-3})	3.3		32.9	
T_e (eV)	5	50	5	50
λ_{ie}/r_p	10	970	1	97
r_p/d_s	129	230	410	729

4.1.2. Double Probe Theory. Expanding the Langmuir probe concept the development of double probes aims at providing reliable probe measurements in a plasma environment with no well-defined reference voltage and a time-dependent space potential[57]. This is done while maintaining a minimum level of disturbance to the plasma from probe currents. These requirements are achieved by adding a second probe tip in the immediate vicinity of the first. The second probe acts as the current source (or sink depending on the direction of bias) thereby truncating and localizing the current path to a distance approximately that of the separation between probe tips. Now the probe circuit can be isolated from ground, requiring no need of an external reference. Furthermore this isolated probe circuit can float with the time-varying plasma space potential maintaining a reliable measure of plasma properties. An additional benefit of the double probe technique is that currents only approximately that of the ion saturation current are required thus further reducing disturbance to the plasma with the added benefit of requiring only a few 10's of volts of bias to adequately capture the full profile. Of primary concern when introducing this second (or any additional) probe tip is the requirement of a tip separation distance, s, to be much greater than the thickness of the sheath that is formed around both biased probe tips. This is to ensure that the sheath of one probe does not contaminate the pick-up of the other maintaining a probe current dependent on the *bulk* plasma properties rather than a localized atypical plasma. Values for s are listed in Table 4.1. Also, based on the r_p/d_s

values found in Table 4.2 along with the knowledge that $s \approx 2.4 \times r_p$ it is clear that this condition is met.

Double probe theory then follows with the assertion that the current to *both* probes is limited by the ion saturation current of the negatively biased probe to maintain current conservation through the isolated probe circuit. For equal probe surface areas, A_p, this ion saturation current limit is the same for both probes and the current as a function of applied probe bias voltage and electron temperature (assuming a Maxwellian distribution) is given by[28],

$$I_p(V_p) = I_{i,sat} \tanh\Big(V_p/(2T_{eV})\Big) \ . \tag{4.5}$$

Using experimental data a function of probe current in the form of (4.5) can then be fitted to estimate $I_{i,sat}$ and T_{eV}. With these two parameters along with the assumptions of $T_e >> T_i$, ion saturation approximately constant over the applied voltage range, a single species ion density, and a quasi-neutral plasma ($n_e \approx n_i$), electron density is given by the Bohm sheath criterion for ion current in the sheath, namely,

$$n_e \approx n_{i,sat} \approx n_i = \frac{I_i}{A_p \exp(-1/2) e u_B} \tag{4.6}$$

where $u_B = \sqrt{eT_{eV}/M_i}$, the familiar Bohm velocity. If a pulsed inductive plasma device is assumed to yield a repeatable plasma, various double probe bias voltages can be selected and reversed to sufficiently fill out the I-V space as a function of time. This is precisely what is done in Subsection 4.2.2 and provides estimates for T_{eV} and n_e to compare against triple probe estimates for validation.

4.1.3. Triple Probe Theory. While the double probe provides many advantages over the single Langmuir probe it is still considered a ‘slow’ probe in some respects and the post-processing task of curve fitting a hyperbolic tangent function can be error inducing and cumbersome. Thus the advent of the triple probe by Chen and Sekiguchi in 1965[37]. By introducing a third probe biased with respect to the other two into a double probe circuit, triple probe theory yields a relation for the ratio of currents between probes as a function of electron temperature. The physical arguments dictating a triple probe parallel those of the traditional Langmuir and double probes subject to the 'thin sheath' and probe separation criteria outlined above. The electron saturation current density is found to be $J_e = n_e e\sqrt{\frac{kT_e}{2\pi m_e}}$. Or more conveniently,

$$J_e = n_e\sqrt{\frac{e^3 T_{\mathrm{eV}}}{2\pi m_e}} \tag{4.7}$$

where T_{eV} is now electron temperature in electron-volts. These base principles are then applied to a probe assembly consisting of three separate probe tips to yield electron temperature and electron density directly using fixed bias voltages. The theory is as follows; First, an electrically isolated triple probe, allowed to penetrate a quasi-neutral plasma via insulated vacuum pass-throughs as shown in Figure 4.2 is considered. Since these probe circuits are isolated the entire assembly is maintained at the floating voltage, V_f. If at this point, two bias voltage sources (i.e., isolated DC batteries), V_{d2} and V_{d3}, are introduced between probe tips 1 & 2 and 1 & 3, respectively, the individual probe voltages would deviate from the floating potential accordingly. However, as the sources are isolated, the probe *assembly* would remain centered about V_f. Furthermore, with these newly added potential differences being applied across adjacent probe tips, charge carriers within the plasma would permit currents I_1, I_2, and I_3 to flow within the system. These concepts are illustrated in Figure 4.3. This current relation is then simply a function of the known bias voltages and electron temperature only given by,

$$\frac{I_1 + I_2}{I_1 + I_3} = \frac{1 - \exp(-V_{d2}/T_{eV})}{1 - \exp(-V_{d3}/T_{eV})}. \tag{4.8}$$

Graphical representation of (4.8) at the voltages used in this work can be seen in Figure 4.4 stylized similar to that presented by Chen and Sekiguchi. Based on the assumption

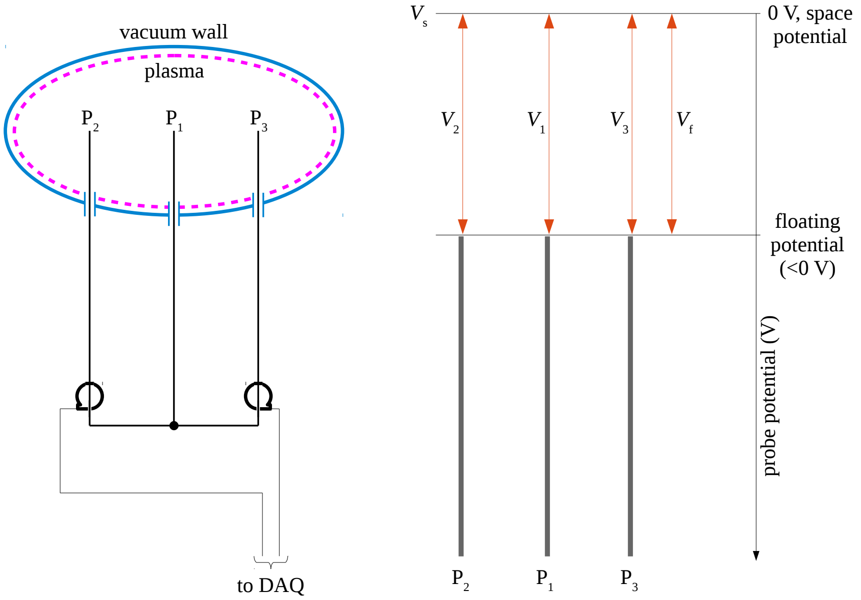

Circuit Diagram

Voltage Diagram

Figure 4.2. Triple probe assembly floating at V_f when no bias voltage (i.e., batteries) present. Current $I_1 = I_2 = I_3 = 0$.

of mono-energetic ions and thermalized electrons the current to each probe tip can be described and combined for equal area probes to yield an ion current density,

$$J_i = \frac{1}{A_p}\left\{\frac{I_3 - I_2\exp[(V_{d2} - V_{d3})/T_{\mathrm{eV}}]}{1 - \exp[(V_{d2} - V_{d3})/T_{\mathrm{eV}}]}\right\} \tag{4.9}$$

where J_i is assumed constant for all probe tip voltages. Finally, for equal electron and ion densities at the sheath edge, density is found by,

$$n_e = J_i \exp(1/2)\left(M_i/e^3 T_{\mathrm{eV}}\right)^{1/2} \, . \tag{4.10}$$

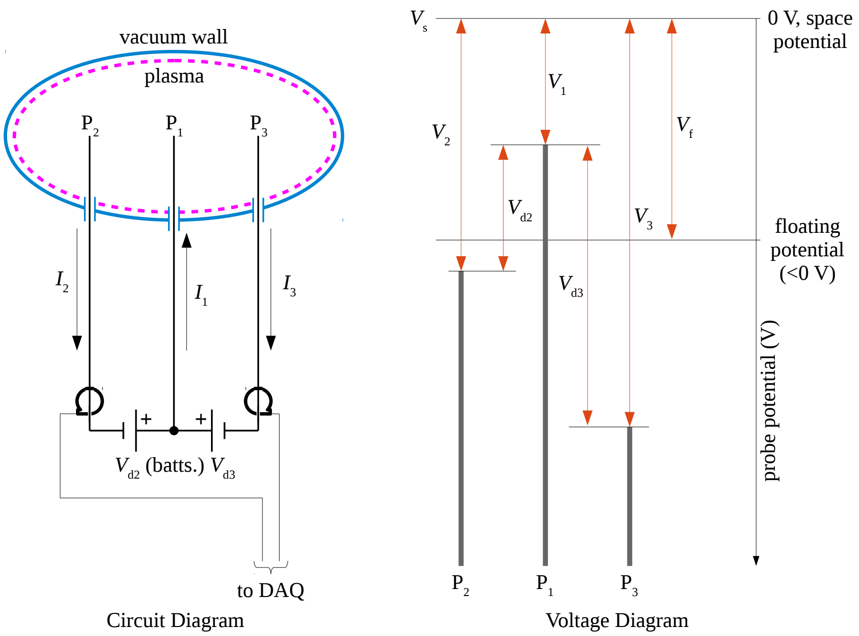

Figure 4.3. Triple probe assembly with the introduction of isolated bias voltages, V_{d2} and V_{d3}. Current $I_1 = I_2 + I_3$.

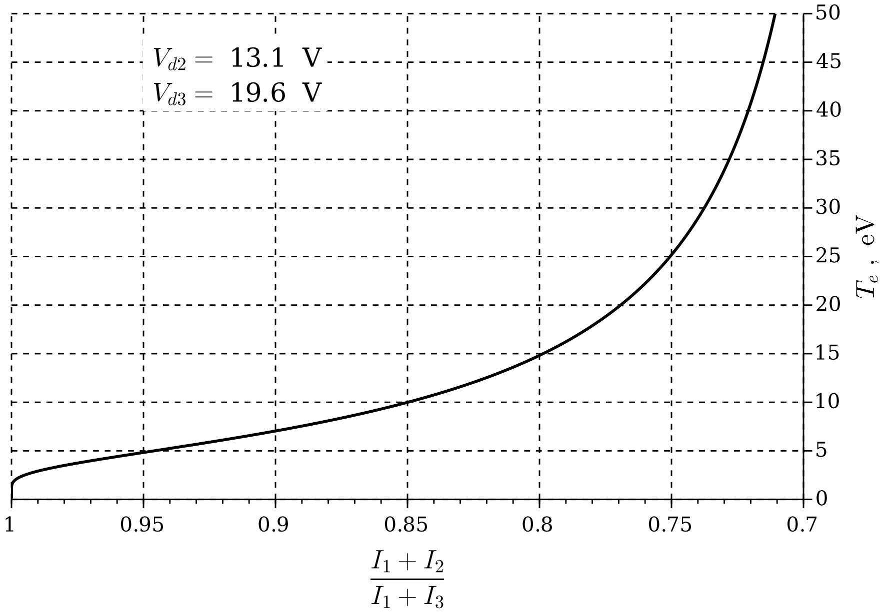

Figure 4.4. Functional dependence of triple probe current ratio on electron temperature from theory. Shown for the bias voltage combination used in this work and styled around that presented by Chen and Sekiguchi (1965).

4.2. PROBE RESULTS

Nomenclature introduced in Section 4.1.3 is continued here where probe tips 2 (TP_2) and 3 (TP_3) have voltages with respect to probe tip 1 of V_{d2} and V_{d3}, respectively, and collect currents I_2 and I_3, respectively. While the shielding efforts described in Section 2.4.1 helped significantly to reduce RF interference and increase signal-to-noise ratio, the spark-gap switch still imposes a substantial high-frequency switching noise at early times from around -1.5 μs to +0.5 μs. To mitigate influence of this noise all current data, both double and triple probe based, are run through a 5 MHz low-pass filter post-process before being used in analysis. Bode plot representation of this filter is provided in Figure 4.5 showing a negligible level of attenuation up through double MPX frequencies ($f_{MPX} \approx 466$ kHz). Some slight phase delay is introduced by filtering and is corrected for in all data presented here.

To confirm conservation of current as triple probe theory demands, preliminary tests were done monitoring current on probe tip one, I_1, in addition to tips two and three. All three current monitors were placed to measure positive electron current *to* the probe tips. Therefore, if working properly, the current sensed on probe one should be the negative sum of the currents sensed on probes two and three as depicted in Figure 4.3. Figure 4.6 confirms this to be the case at sample conditions of 90 mTorr in argon.

4.2.1. Repeatability of Triple Probe Currents. Probe currents were collected at radial locations of $r = 0$ (centerline), $^1/_4$ R, $^1/_2$ R, $^3/_4$ R, and R for all four gases; hydrogen (diatomic, H_2), helium, argon, and xenon. Effort has been made to verify the repeatability of the MPX discharge through the analysis of triple probe data collected between 10 and 100 mTorr. Between two and four shots were taken at all of these locations and for all gases. Figures 4.7(a-d) show the shot-averaged currents along with the shot-to-shot standard deviations, σ_I, at $^1/_2$ R for all gases at 50 mTorr.

Figure 4.8 shows the average standard deviation between shots, $\overline{\sigma}$, at all pressures and gases species at the $^1/_2$ R radial location. This figure shows quantitatively the high

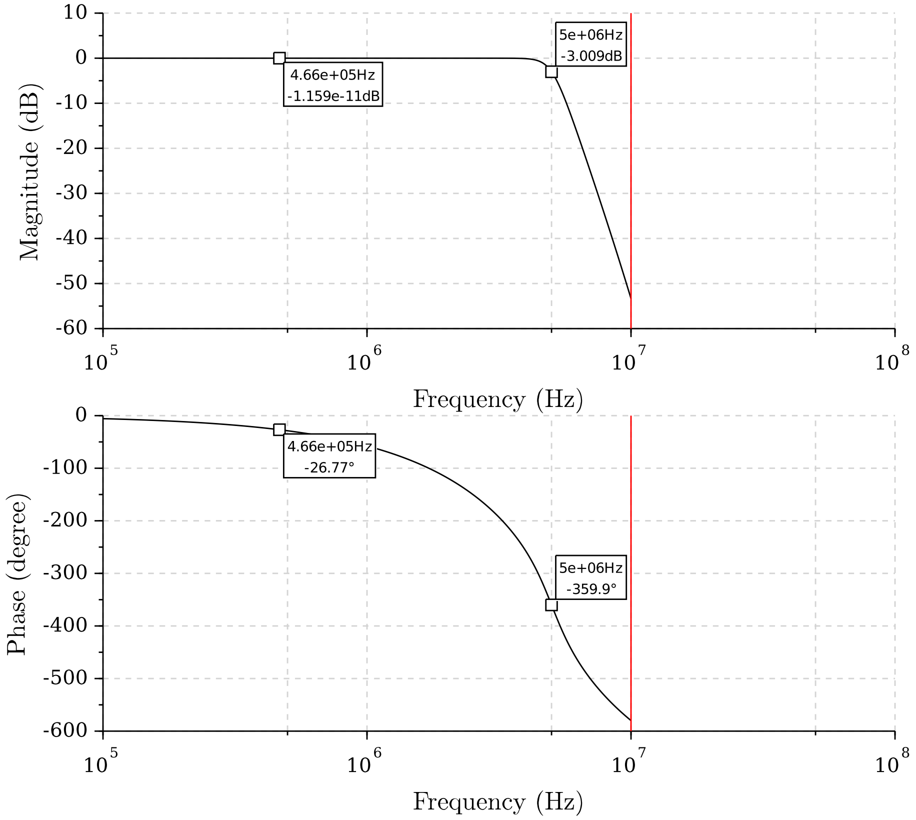

Figure 4.5. 5 MHz low-pass filter Bode plot representation.

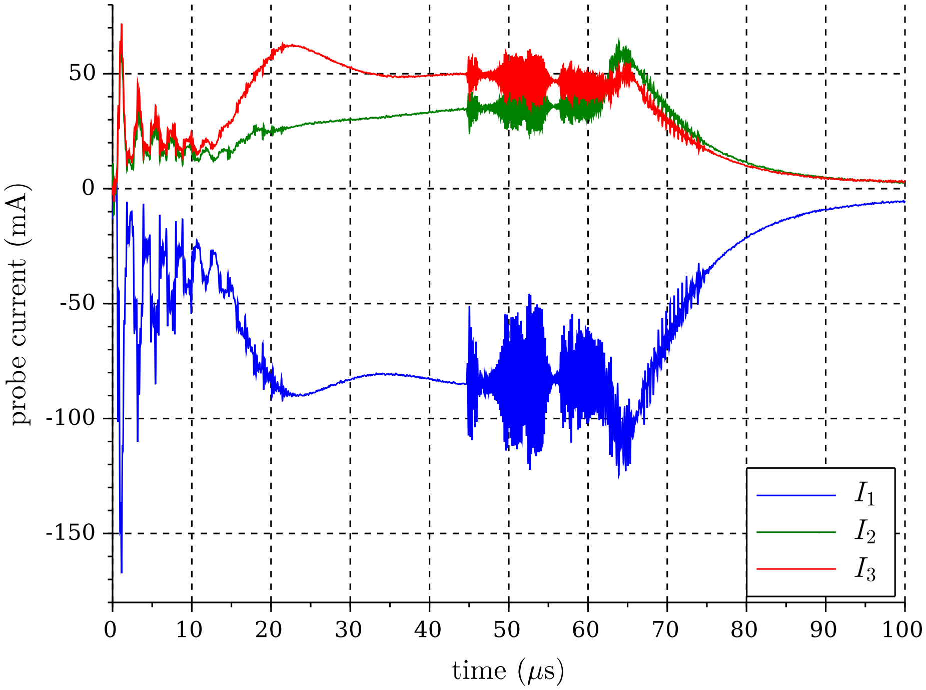

Figure 4.6. Confirmation of current conservation across triple probe assembly.

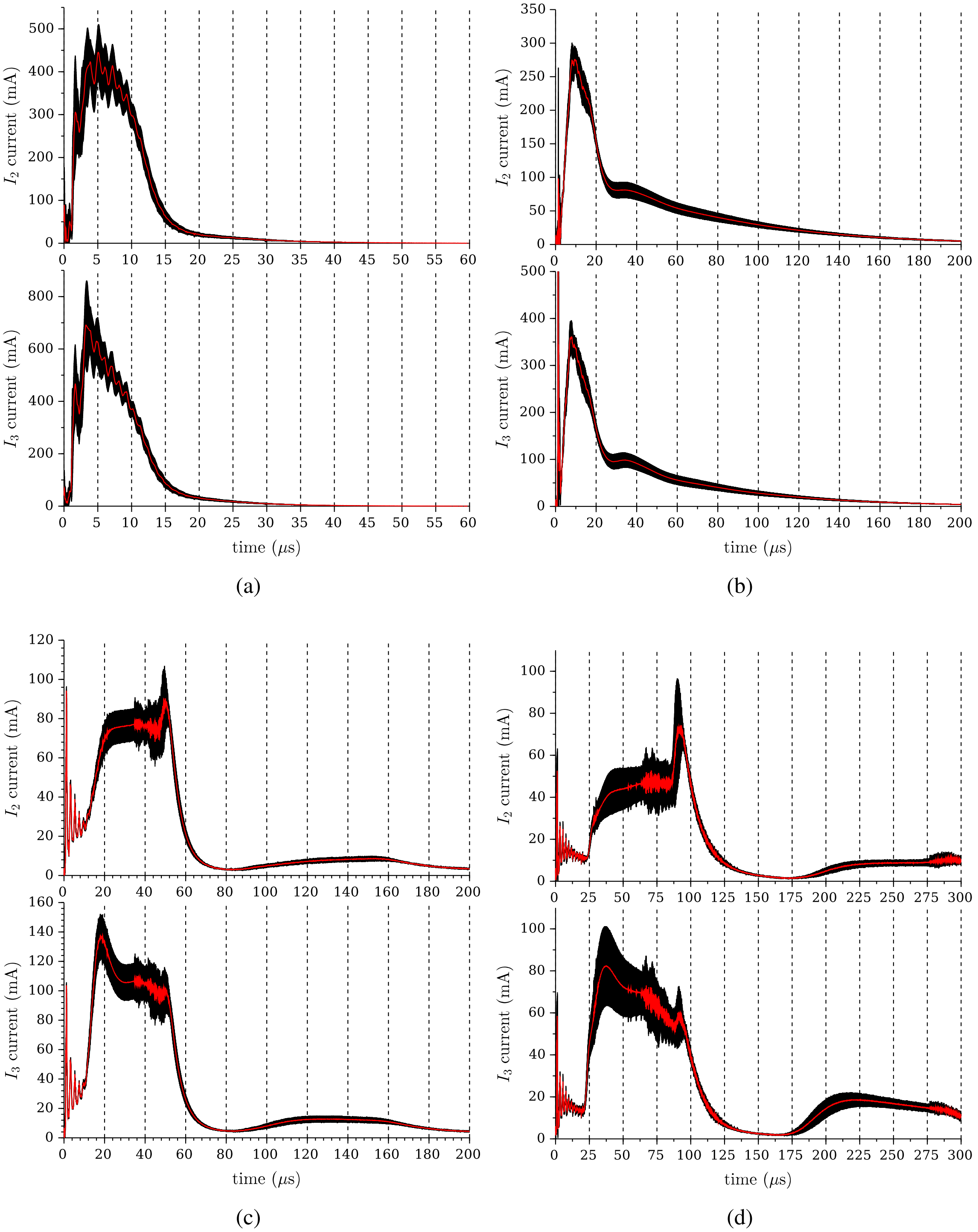

(a) (b) (c) (d)

Figure 4.7. Average current (red) and standard deviation (black) at the ½ R location in 50 mTorr (a) hydrogen, (b) helium, (c) argon, and (d) xenon.

degree of erratic plasma formation exhibited at low pressures with deviations of more than 100 mA at 20 and 40 mTorr decreasing to 5 mA or less for all gases and currents at 90 mTorr and above. Also, this trend of increasing repeatability for higher pressures agrees qualitatively with trends seen previously in MPX by Pahl and Rovey[58].

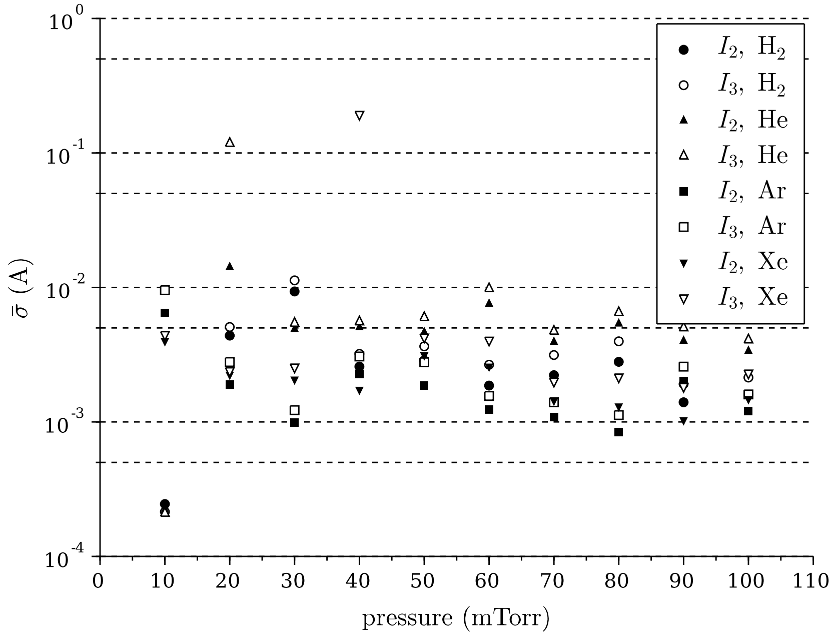

Figure 4.8. Average standard deviation of probe current for all pressures and gas species tested at the $^1/_2$ R probe location.

4.2.2. Triple Probe Validation through Double Probe Analysis. To provide confidence in the triple probe results presented here studies with a double probe configuration were compared with those of the triple probe. This approach has been successfully performed previously with double probe temperature and density agreements reported by Mackel *et al.* of within 30% and 9%, respectively, below triple probe estimates and temperature and density agreements between probes of within 7.5±4.5% and 8.5±5.5%, respectively, reported by Naz *et al.*[9, 59, 60]. Double probe studies in argon at 10, 30, 50, 70, and 90 mTorr and at the $r = {}^{R}/_{2}$ location were compared with triple probe studies in the same conditions and location using the same probe assembly. Double probe currents were sourced from multiples of high-current lantern batteries ranging from none (±0V) to six batteries in series yielding a peak applied bias of ±39.34 volts. Figure 4.9b shows a sample of collected double probe currents at 90 mTorr. While Figure 4.9a is the reconstructed I-V double probe trace accompanied by a least-squares curve fit with a functional form of (4.5). Each current data point and current trace in Figures 4.9a and 4.9b, respectively, are the resulting average of three tests done at the voltage indicated. Negative voltages were achieved by simply reversing the wiring to the probes. These resulting double probe currents were also used in the selection of appropriate bias voltages for triple probe studies based on the following observations. Visual inspection reveals that the ±6.58 volts applied (1 battery) yielded a significant undesired asymmetric current. Also, at voltages of ±26.25 volts (4 batteries) and above it became increasingly difficult to avoid test results where an undesired arc across probe tips resulted at some time during collection. This is also why Figure 4.9b is truncated at 15 µs. Avoiding these two adverse issues, a combination of V_{d2} = 13.1 volts and V_{d3} = 19.6 volts, or two and three batteries, respectively was chosen for use in all triple probe studies presented in this work. These voltages for MPX (~ 80 J stored energy) fall well within those found in literature with Byrne *et al.* (2001) using 3 and 18 volts for low energy (20 J) pulsed plasma thruster plume studies and Kirtley (2008) using 13 and 38 volts for high energy (up to 1 kJ) pulsed inductive plasma studies[9, 61].

Figures 4.10a-d show comparisons between double and triple probe T_e and n_e estimates in argon at 30 to 90 mTorr. Triple probe data seen here are the resulting average of two to four tests at the given conditions and in most cases standard deviation between tests was below 10% for electron temperatures and less for electron densities. Close agreement between the two probe methods can be seen until around 8 to 12 microseconds with worst case percent differences of 25.5±23% and 11.5±9% for temperature and density, respectively, in that time frame. This late-time divergence between probes is believed to be the result of a thin layer of higher density plasma, translating radially inward and intercepting

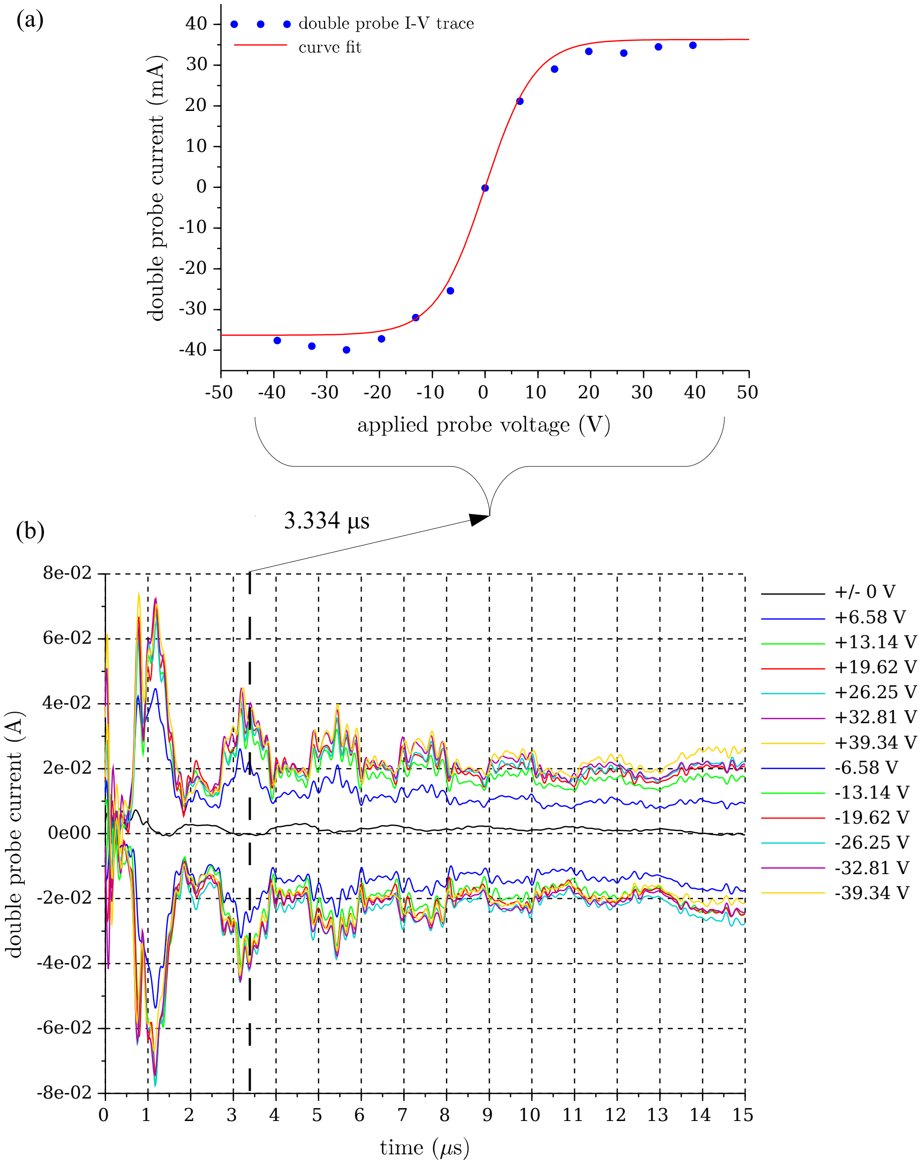

Figure 4.9. (a) Reconstructed double probe current sampled at 3.334 µs plotted as a function of probe voltage. (b) Double probe current verse time in 90 mTorr argon backfill and all positive and reversed bias voltages tested from 0 to 15 µ.

the probe residing at this $^{R}/_{2}$ location. This phenomenon will be the subject of discussion in Section 4.2.3. Upon departure from this high-density encounter the two probe methods can be seen to settle back into the same level of agreement as that of the early times which is interpreted here as an indication that electron temperature and density estimates past the initial encounter are still accurate.

Brief mention of the results of the 10 mTorr comparisons between double and triple probe estimates (shown in Figure 4.11) is made to highlight the observation that plasma formation was difficult at this pressure. Specifically, it was found that across all gas species tested an operating pressure of 10 mTorr represented an approximate lower threshold for reliable plasma formation. Despite the presence of a DC glow pre-ionization source results at 10 mTorr proved difficult to verify, generating plasma activity comparable to higher pressures only once every five to seven shots.

4.2.3. Triple Probe Current and Evidence of a Plasma Wave. In addition to the early times (< 15 μs) of the discharge, attention was given to the later times in the context of what appeared to be a radially translating high density wave. Figures 4.12 to 4.15 show probe current profiles hydrogen, helium, argon, and xenon, respectively, in a sample pressure of 50 mTorr. Currents in hydrogen and helium can be seen to have the highest magnitudes at the $3R/4$ location while currents in argon and xenon are seen to have a highest magnitude at the R location and reduce steadily as the probe is moved radially inward. By inspection it can be seen from Figures 4.14 and 4.15 for argon and xenon, respectively, and to a lesser degree in Figure 4.13 for helium that a higher charge density region (inducing higher probe currents) is moving radially inward. As an example the reader is directed to Figure 4.14 at approximately 8, 10, 18, 28, and 33 μs for the R, $3R/4$, $R/2$, $R/4$, and $r = 0$ probe locations, respectively, where currents can be seen to ramp-up. Additionally, this region appears to apex at approximately the center ($r = 0$) location and then propagate radially back out at around the same rate. Using known radial probe locations and times corresponding to the initial 'knee' in probe current I_3 a radial velocity,

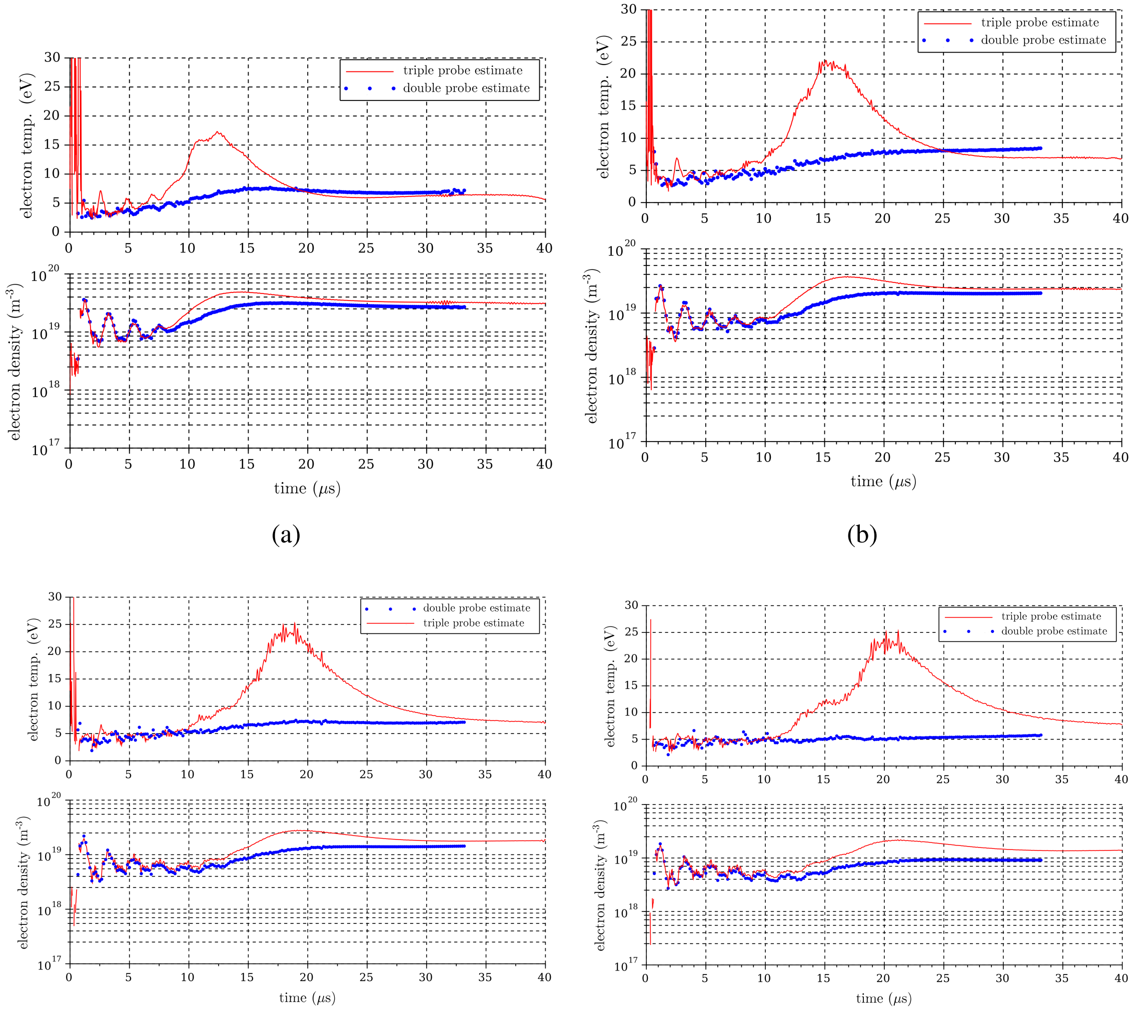

(a) (b)

(c) (d)

Figure 4.10. Comparison between double and triple probe methods at (a) 30, (b) 50, (c) 70, and (d) 90 mTorr.

v_r, of the high density front has been calculated. This time in the current I_3 profile was perceived as the time when the complete transition from pre-wave to full wave densities has occurred. In many cases this time was very apparent. However, in the lighter gases at lower pressures this point was less obvious due to either main current coupling at early times (e.g. Figure 4.12), high noise, or non-repeatable phenomena (i.e., instabilities) corrupting the average. For these reasons accurate velocities in the lighter gases became difficult to

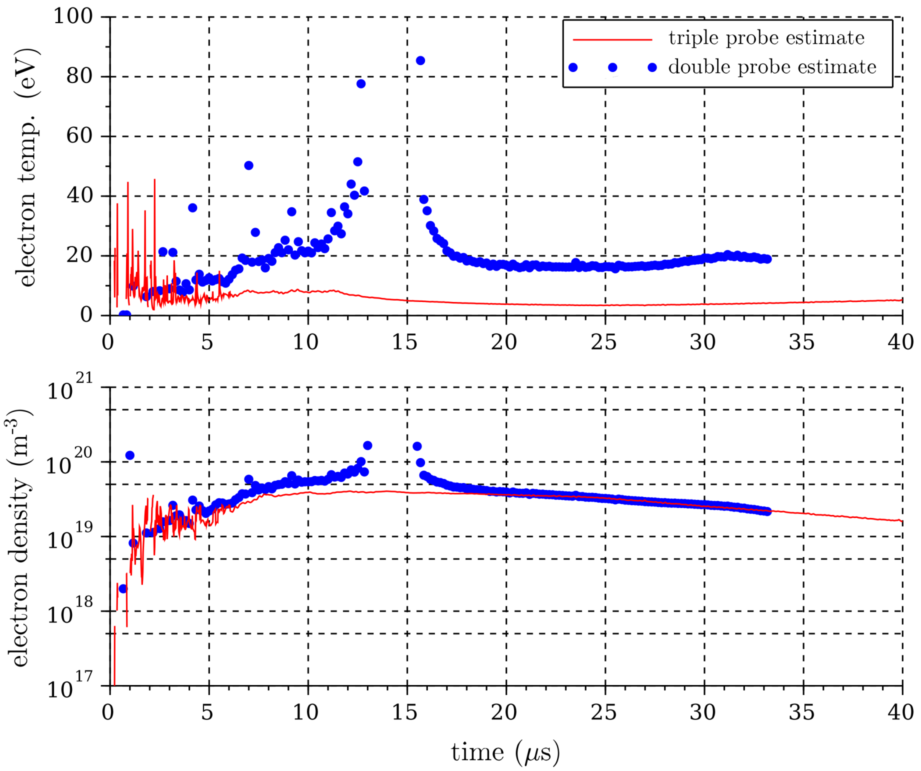

Figure 4.11. Comparison between double and triple probe methods at 10 mTorr argon.

discern and thus trends are less clear. Nonetheless, Figure 4.16 shows the radial velocities found for each gas species as a function of pressure by this method. These velocities are a four position (3/4 R to 0 R) average.

Figure 4.16 demonstrates that these radial velocities are dependent on species and pressure. Or alternatively, on M_i and $(nk_{\mathrm{B}}T)$. As a point of reference the ion acoustic wave speed for one-dimensional compression with isothermal electrons is given by[56],

$$v_s = \left(\frac{k_{\mathrm{B}}T_e + \gamma_i k_{\mathrm{B}}T_i}{M_i}\right)^{1/2} \tag{4.11}$$

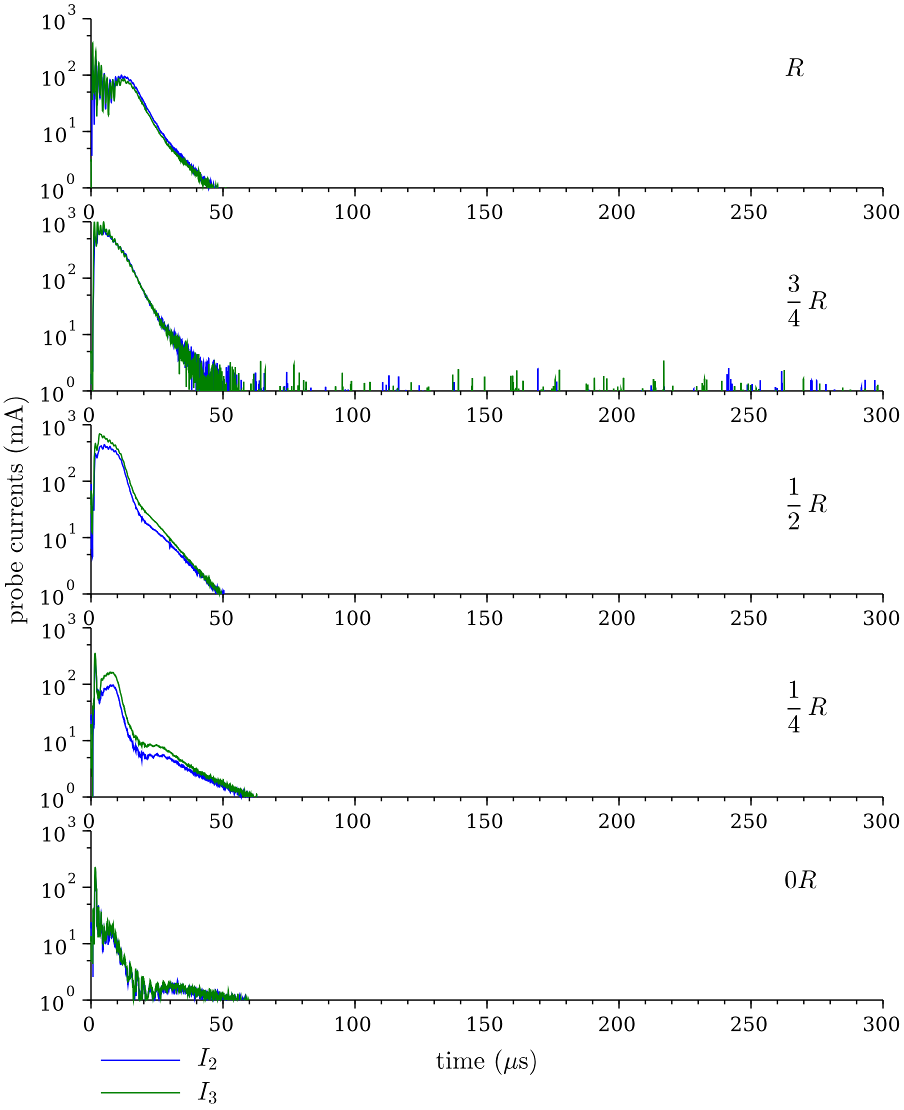

Figure 4.12. Triple probe currents in 50 mTorr hydrogen as a function of radial position.

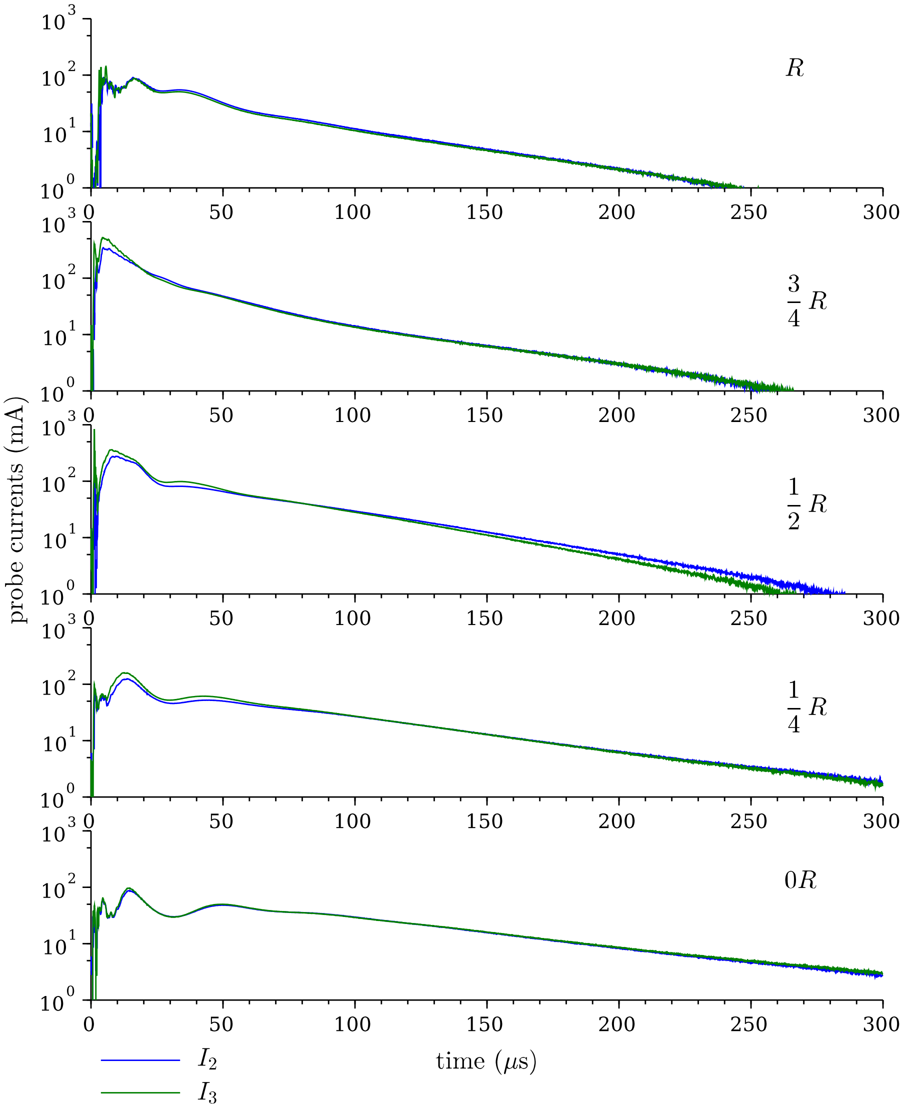

Figure 4.13. Triple probe currents in 50 mTorr helium as a function of radial position.

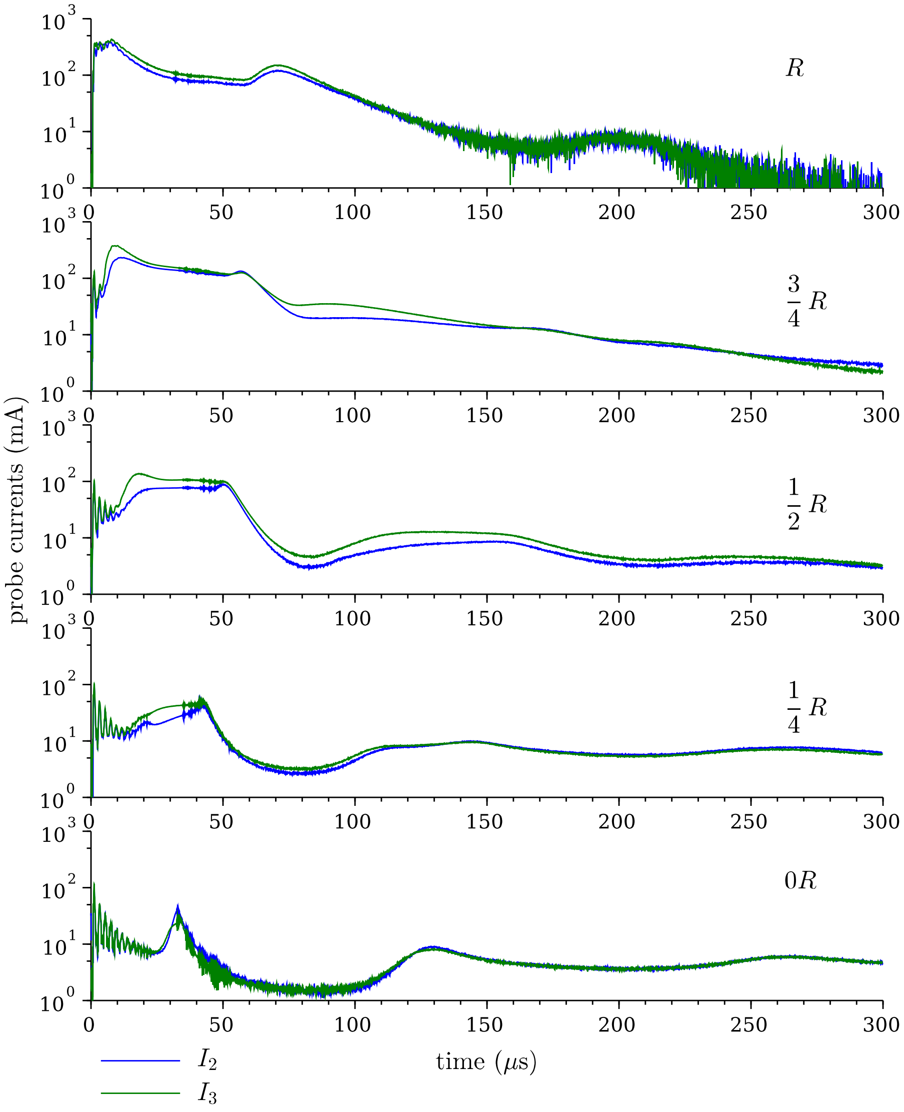

Figure 4.14. Triple probe currents in 50 mTorr argon as a function of radial position.

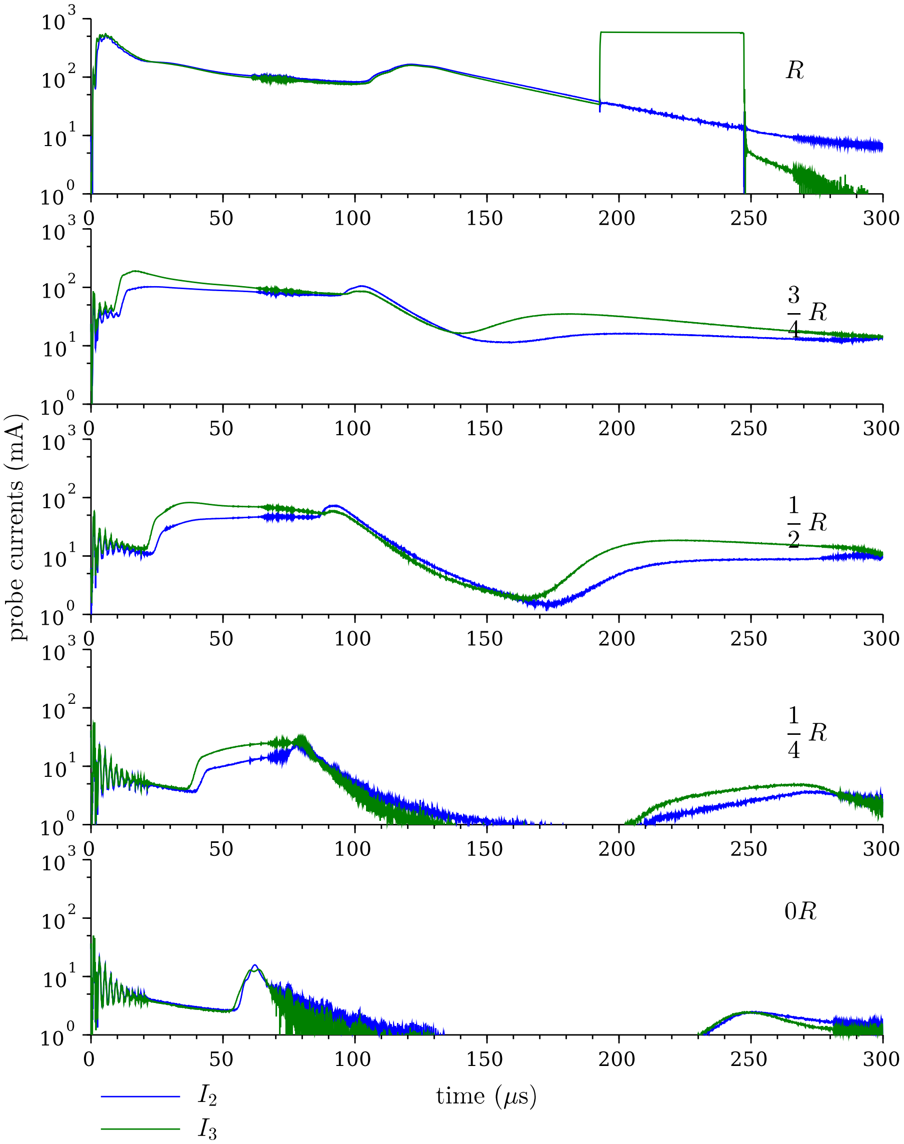

Figure 4.15. Triple probe currents in 50 mTorr xenon as a function of radial position.

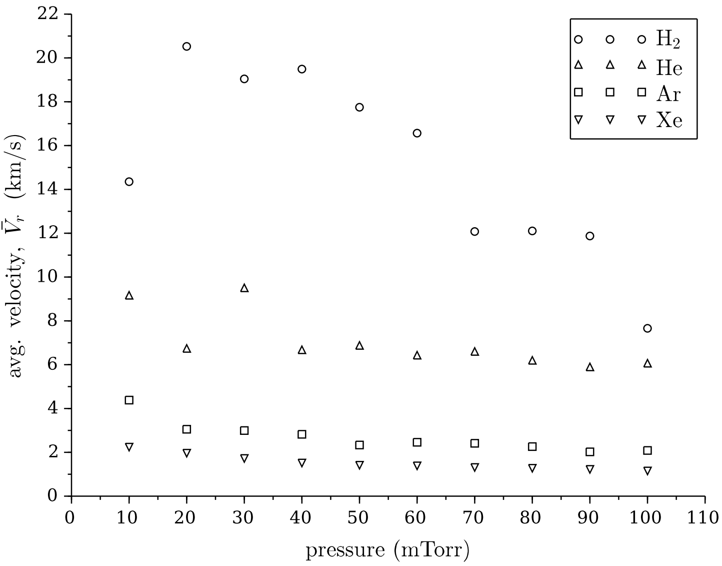

Figure 4.16. Average high density wave velocity in all gases as a function of backfill pressure.

where γ_i is the ratio of specific heats for the ions and M_i is the ion mass as given in Table 2.1. If the assumption of $T_e >> T_i$ is made then (4.11) becomes,

$$v_s \approx \left(\frac{k_B T_e}{M_i}\right)^{1/2} \tag{4.12}$$

For an electron temperature of $T_e = 5.8 \times 10^4$ K ($T_{eV} = 5$ eV) in argon (4.12) gives a wave speed of $v_s = 3474$ m/s. Returning to Figure 4.16 this agrees reasonably well with calculated average speeds for argon. If v_s is taken to be $\overline{V_r}$ with the overbar to mean a radially averaged V_r and (4.12) is rearranged to give a power law relationship,

$$\frac{\log \overline{V_r}}{\log(k_B T_e / M_i)} = \frac{1}{2}, \tag{4.13}$$

then excellent agreement (maximum over all pressures of less than 7% deviation from ½) can be seen in Figure 4.17 by assuming an average temperature of 5 eV and using the wave

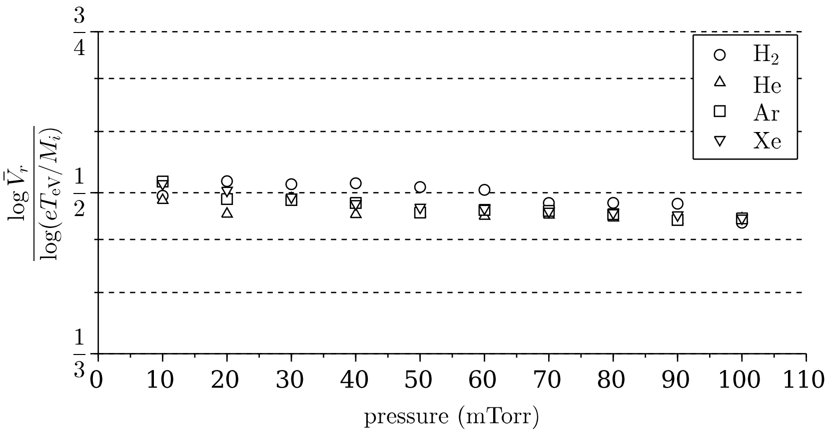

Figure 4.17. Power law relationship of the average radial high density wave velocity for a constant electron temperature, T_{eV} = 5 eV.

velocity estimates seen in Figure 4.16. The approximation in (4.12) will be revisited in Section 4.2.4 in the context of electron temperature estimation.

4.2.4. Electron Temperature and Density During Discharge. Since primary interest is on energy dissipation by the main discharge current to the plasma, electron temperature and density studies focus primarily on results within the discharge time from 0 to approximately 20 μs. Figures 4.18 to 4.21 show radially resolved electron temperature and density estimates from triple probe current analyses at the sample pressure of 50 mTorr in this time frame. One striking feature is immediately apparent when comparing the time-resolved electron temperatures and densities of the lighter species (H_2, He) to those of the heavier species (Ar, Xe): The lighter species are seen to fluctuate at a frequency of double that of the main discharge ($f_{MPX} \approx 466$ kHz) at near 1 MHz while heavier species appear to fluctuate at the same frequency as the main discharge. Furthermore, the higher frequency in activity associated with the lighter gases appears primarily in electron temperature variation while the lower frequency in activity associated with the heavier gases appears mostly confined to plasma density variation. It can also be seen from Figures 4.18 to 4.21 that 80% to 90% of all temperature estimates fall below 20 eV. This temperature limit was also observed in the steady-state corona model results of the previous chapter. Of particular note is that Figures 3.10 and 4.20 should be directly comparable for the 50 mTorr argon case and this comparison is made in Figure 4.22.

Figure 4.23 shows electron temperatures and densities radially resolved and time-averaged over the 0 to 20 μs discharge time for all tested pressures and species. As expected higher temperatures (~ 15 eV) and densities (> 10^{19}m^{-3}) are seen to reside near the wall of the cylindrical MPX quartz tube where coupling with the main coil is maximum. This being complementary to lower temperatures (~ 5 eV) and densities (< 10^{19}m^{-3}) seen near the centerline. Temperatures in hydrogen can be seen to increase with pressure more than all other species with a radial average of 3.8 eV. This agrees qualitatively with previous MPX work by Pahl and Rovey in which it was reported that ohmic (heating) losses to the plasma increased overall with pressure and increased more in hydrogen than in argon and xenon[21]. Additionally, plasma density in Figure 4.23 is seen to increase with radial location for higher pressures with a species average at 100 mTorr of 9.5×10^{17}, 2.5×10^{18}, 7.3×10^{18}, 2×10^{19}, and 5.8×10^{19} per m^3 for $r = 0$, $R/4$, $R/2$, $3R/4$, and R, respectively. This follows with the theory that higher backfill pressures (i.e., increased neutral densities) will make it more difficult for plasma created primarily at R by mutual inductance to penetrate to the centerline before dispersion via collisions.

Time-averaged density levels relative to a 1% and 10% ionization fraction (solid lines) at the $r = R$ probe location can be seen in Figure 4.24. Here heavier gases can be seen to maintain a higher ionization fraction than lighter gases. Perhaps more telling however, is that increased ionization levels seen in Figure 4.24 across species corresponds approximately with the reduced energies required to ionize seen in Table 2.1. That is with the exception of hydrogen. However, if the much lower energy to dissociate diatomic hydrogen of 4.5 eV is considered along with the energy of 13.6 eV required to ionize now single hydrogen atoms, a combined ionization potential for H^+ of 18.1 eV is found bringing it closer to that of helium than previously considered.

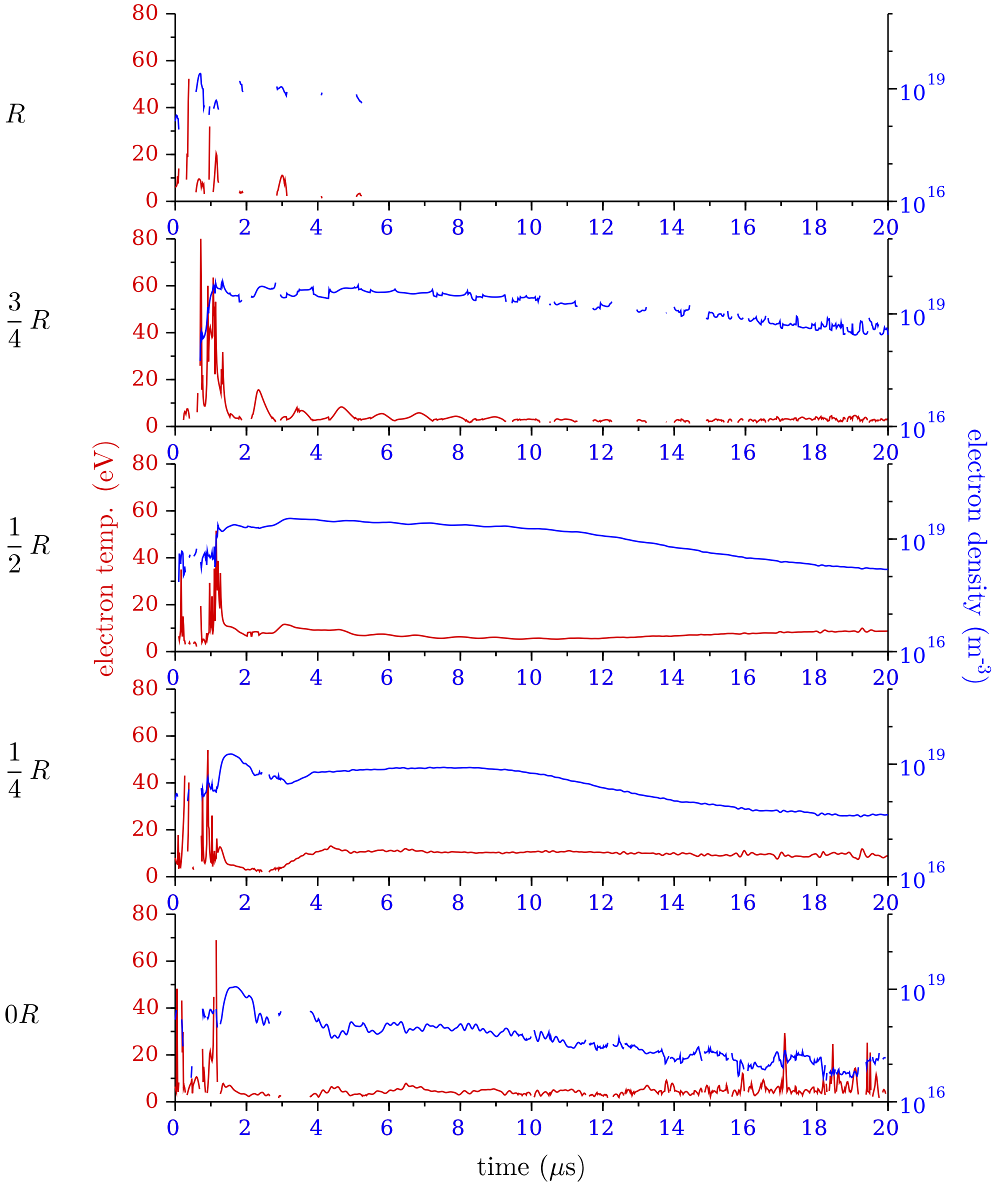

Figure 4.18. Electron temperature and density estimates for hydrogen at 50 mTorr.

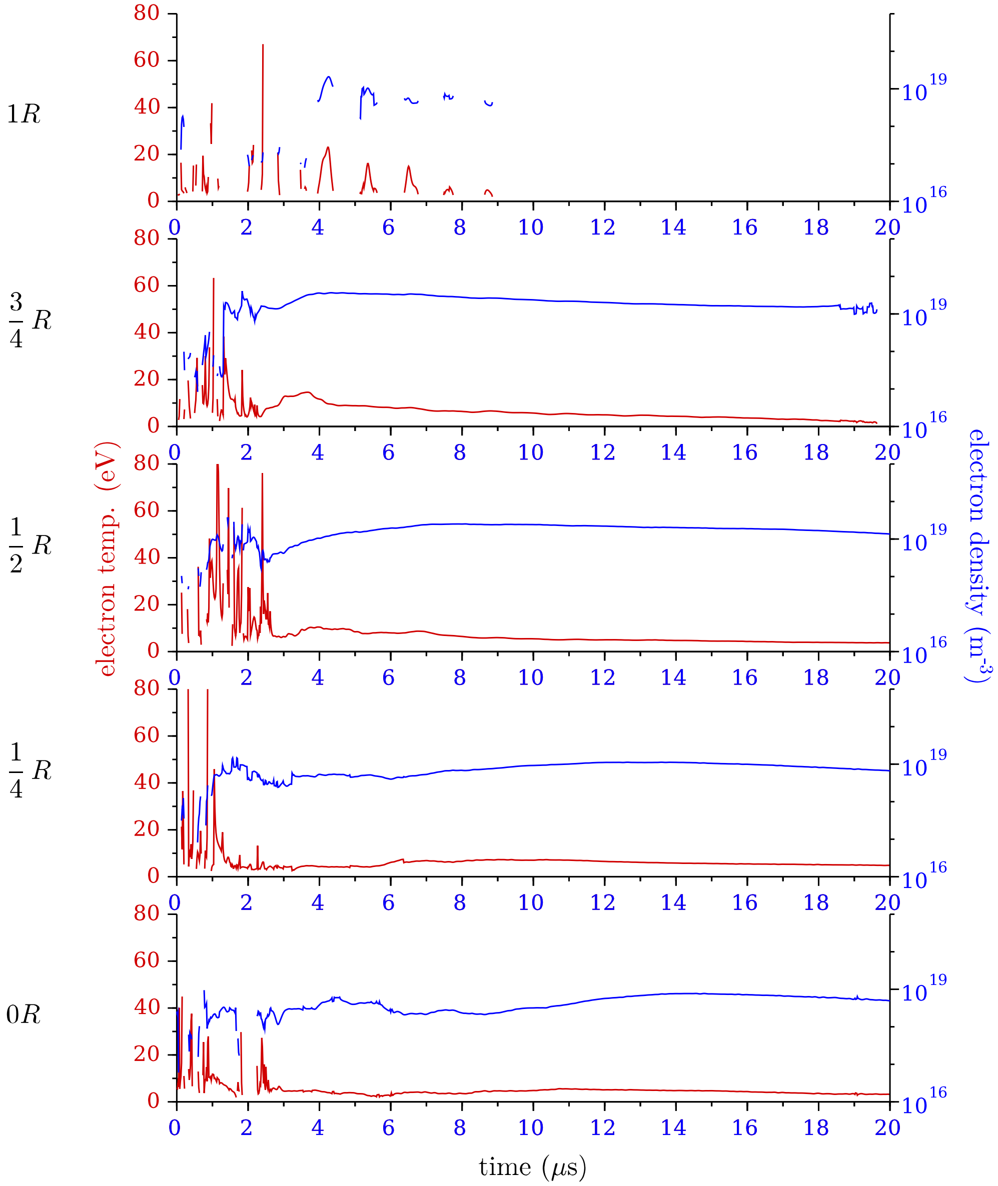

Figure 4.19. Electron temperature and density estimates for helium at 50 mTorr.

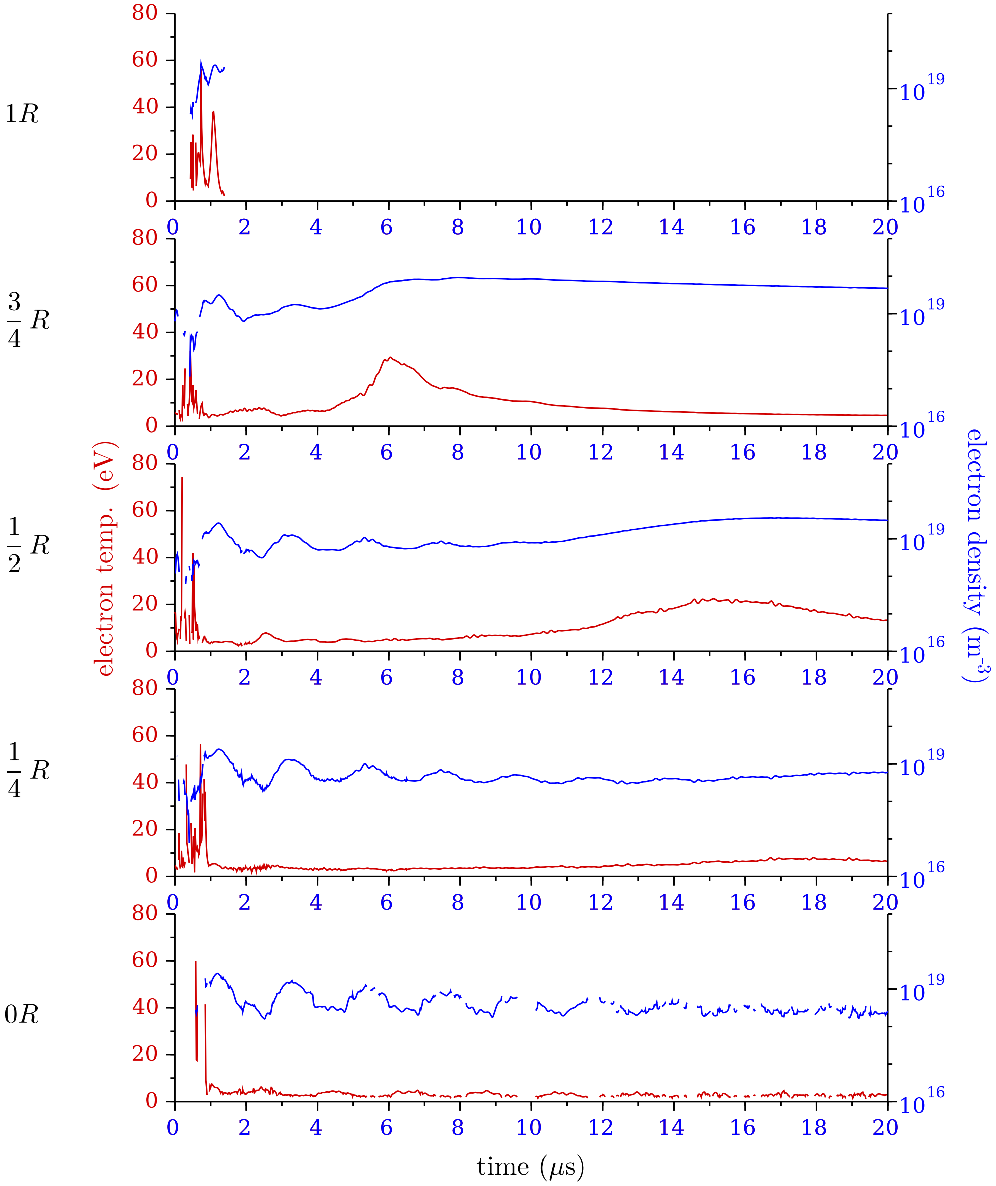

Figure 4.20. Electron temperature and density estimates for argon at 50 mTorr.

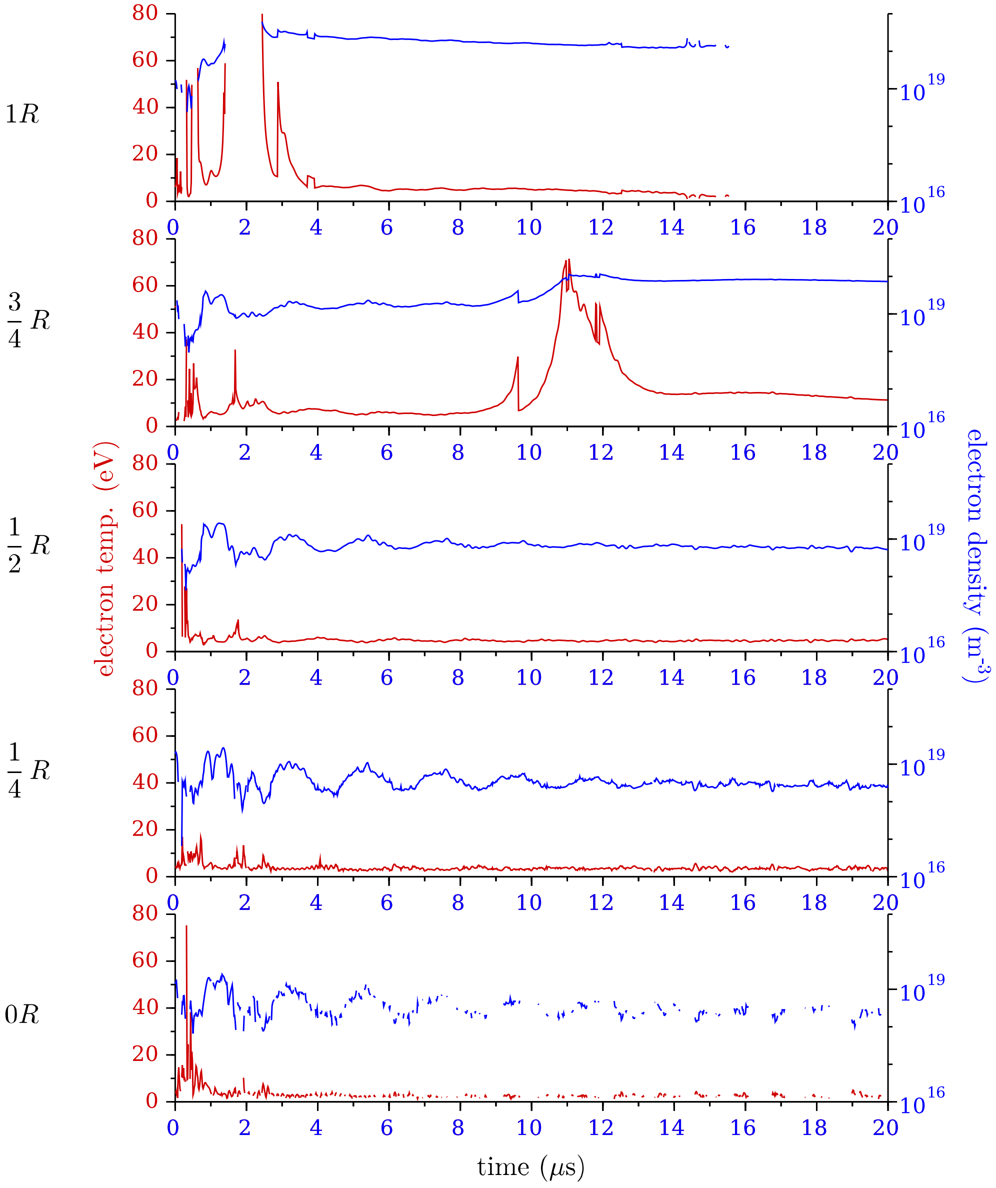

Figure 4.21. Electron temperature and density estimates for xenon at 50 mTorr.

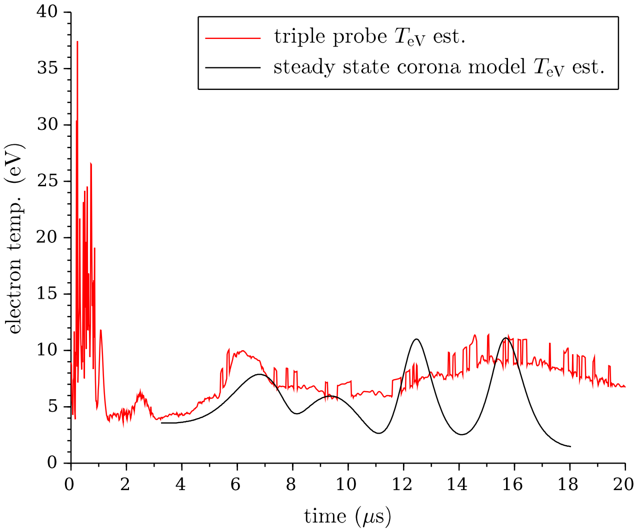

Figure 4.22. Comparison between triple probe and steady-state corona model spectroscopy results for 50 mTorr argon. Triple probe result is the radially averaged temperature.

Briefly, a return to (4.12) is made with the substitution for v_s of $\overline{V_r}$ giving the radial wave velocity as a function of electron temperature and species mass. Rearranging for temperature one finds,

$$\overline{T_{\mathrm{eV}}} = \frac{M_i \overline{V_r}^2}{e} \tag{4.14}$$

with the overbar once again to mean the radial average and mass species, M_i, given in Table 2.1. Now, using measured average velocities, $\overline{V_r}$ from Figure 4.16 electron temperatures can be estimated and Figure 4.25 shows these estimates for all gases as a function of pressure. Average temperatures from this method do show an opposite trend to that of Figure 4.23a which is attributed here to divergence in $\overline{V_r}$ from plane-wave theory that (4.11) is based upon as the wave moves radially inward.

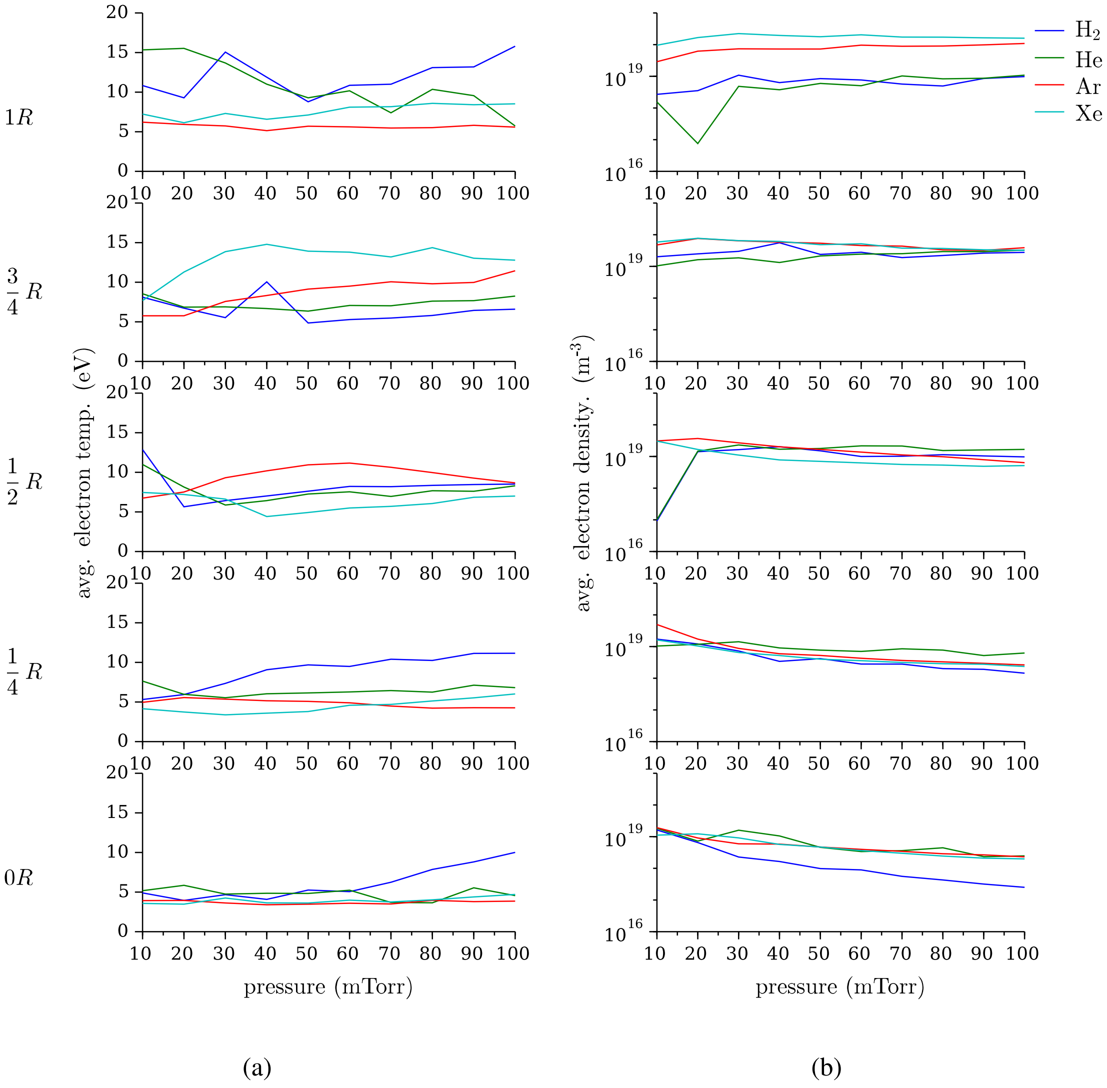

Figure 4.23. Time-averaged electron (a) temperature and (b) density during discharge as a function of pressure and radial position for all gas species.

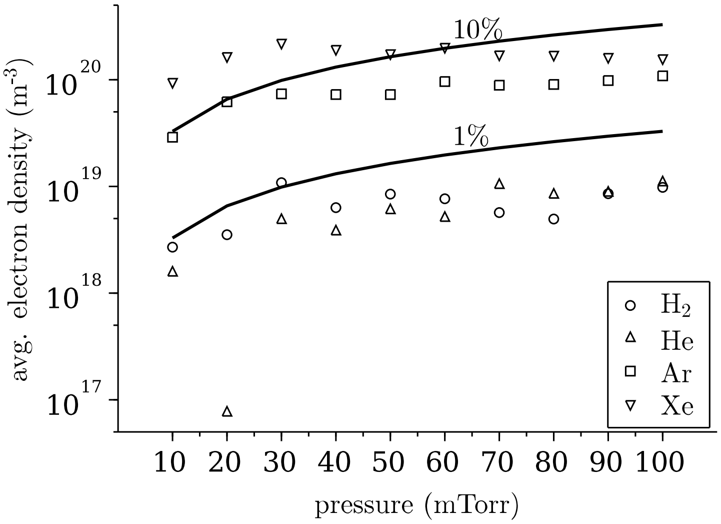

Figure 4.24. Time-averaged density as a function of pressure and species at $r = R$. Solid lines represent a constant ionization fraction.

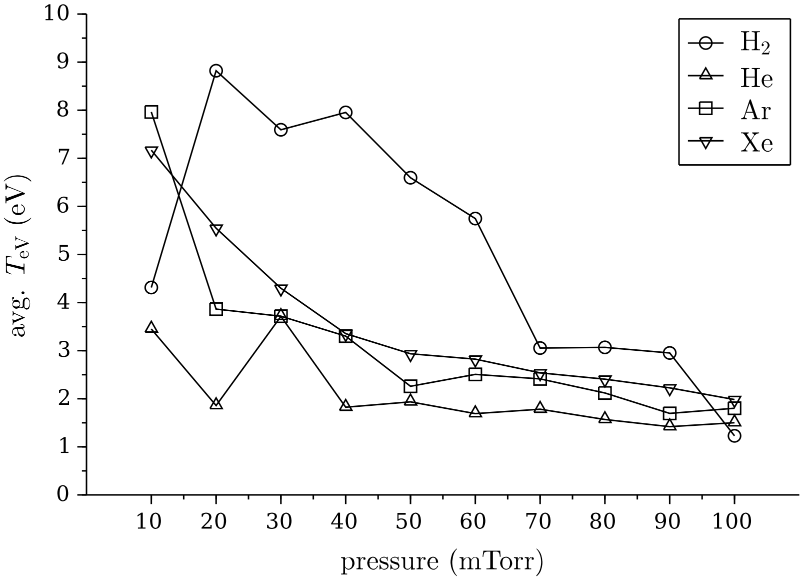

Figure 4.25. Using the ion acoustic wave speed as a measure of the average electron temperature.

5. ENERGY ANALYSIS

5.1. CALCULATION OF ELECTRON AND ION ENERGIES

With the temperature and density data obtained, a quantitative look at the energy entrained in the plasma can be performed. Specifically, energies in electrons with a temperature, T_{eV}, and in ions with ionization potential, E_{iz}, are calculated and presented as a function of time, radial location, species, and/or pressure. A simple radial integration scheme was applied to allow for volumetric total energy estimates. There where five radial locations for which triple probe data were collected. However, the $r = R$ probe location experienced significant signal issues. Most notably were non-physical current ratio readings of $I_2/I_3 > 1$ at early times when inductive coupling with the main coil was still dominant. This was generally the cause of missing regions of data in electron temperature and density estimates at the $r = R$ location such as those seen in Figures 4.18 to 4.21. To avoid this issue and provide more complete accounts of plasma energy, temperature and density estimates from the $r = {}^{3R}\!/_{4}$ to $r = 0$ locations were used. The total cylindrical volume was then partitioned into four concentric tubular volumes with bounding radii and characteristics outlined in Table 5.1 and highlighted in Figure 5.1. Energies were calculated by the following: Energy per electron with a temperature of T_e is equal to $k_{\mathrm{B}}T_e$. Or for convenience here eT_{eV} with temperature in volts. Total energy in volume, V, then with density, n_e is given by,

$$\text{total thermal electron energy} = en_eVT_{\mathrm{eV}}. \tag{5.1}$$

Energy in ions is generally more involved. However two assumptions are made here to simplify calculation. One is that as stated earlier ion temperatures are much less than electron temperatures, $T_i << T_e$. The other is that any kinetic energy in the ions is negligible compared to the ionization energy, E_{iz}, that was required to produce them. Thus the total

Table 5.1. Radial volume partitioning used in energy analysis.

label	radii inner	 outer	volume, V (cm^3)
A	$3R/4$	R	6468
B	$R/2$	$3R/4$	4620
C	$R/4$	$R/2$	2772
D	0	$R/4$	924

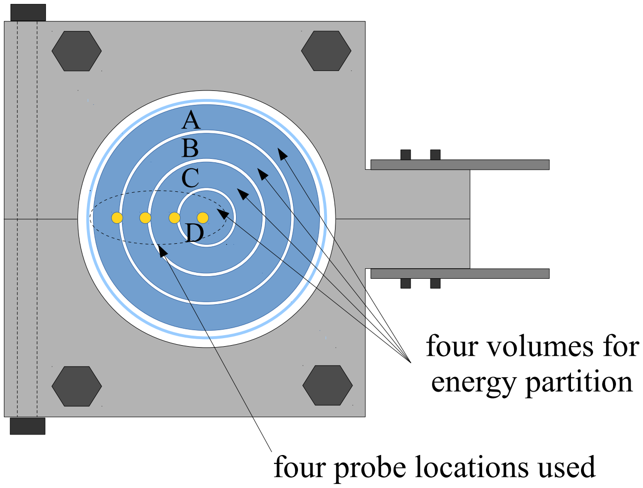

Figure 5.1. Additional clarification of volume partitioning scheme applied for energy analysis. Note the four inner probe locations were used in energy calculations.

energy entrained in ions with density, $n_i \approx n_e$ is given by,

$$\text{total ion energy} = en_e V E_{\text{iz}}. \tag{5.2}$$

Figures 5.2 and 5.3 show results of radially integrated energy in electrons and ions for all four species at 50 and 100 mTorr, respectively. Note that the red data are energy in electrons only and blue data are the sum of ion and electron energies. This allows the reader to readily see the percentages of energy entrained in electrons and ions separately while still providing the total energy profile. As mentioned in the double probe validation section, electron temperature and density estimates have shown good accuracy after the high density wave encounter. With this assumed, Figures 5.2 and 5.3 show that electron and ion energies both take longer to dissipate for heavier species. Hydrogen appears to lose nearly all of it's energy by 20 μs while helium loses most of it's energy within 20 to 30 μs but retains about 10 to 15% past 50 μs in ion energy. Energy dissipation in the heavier gases appears to happen much slower. In 50 mTorr Argon retains approximately 1.25 J in ion energy from 10 μs out to around 50 μs. Xenon demonstrates this further still by retaining 1 J in ions from 15 to 90 μs (and later for higher pressures). In both of the heavy gases as well as helium it appears that once the high charge concentration wave intercepts the probe upon return from the centerline outwards the energy stored in electrons diminishes substantially.

Energy data for all species appears to verify that ion energy entrainment slightly lags that of electron energy by 1 to 2 μs. This agrees with intuition as the light mobile electrons are always the first medium through which electrical energy is transferred. Following via collisions to other outlets such as excitation, ionization, losses to the walls, etc. Complementary to this energy in electrons consistently appears to *dissipate* first as well. Figure 5.4 shows the time-resolved radially integrated sum of ion and electron energies for all species and pressures. Figure 5.4a for hydrogen shows that consistently at all pressures tested energy in H_2 plasma is precipitously lost following (or even preceding, at higher pressures) the end of the main discharge at around 23 μs. While xenon in Figure 5.4d is shown to retain energy out to multiple discharge time scales.

Figure 5.5 shows peak electron and ion energy separately against pressure for all gas species. Peaks here were found within a much larger time frame than the discharge time. Namely, peaks within a time frame of 0 to 100 μs were used to capture full activity in all gas species. It is noted here that data for hydrogen at 40 mTorr is omitted due to an invalidated data set. Inspection of Figure 5.5 concludes that peak energy in electrons

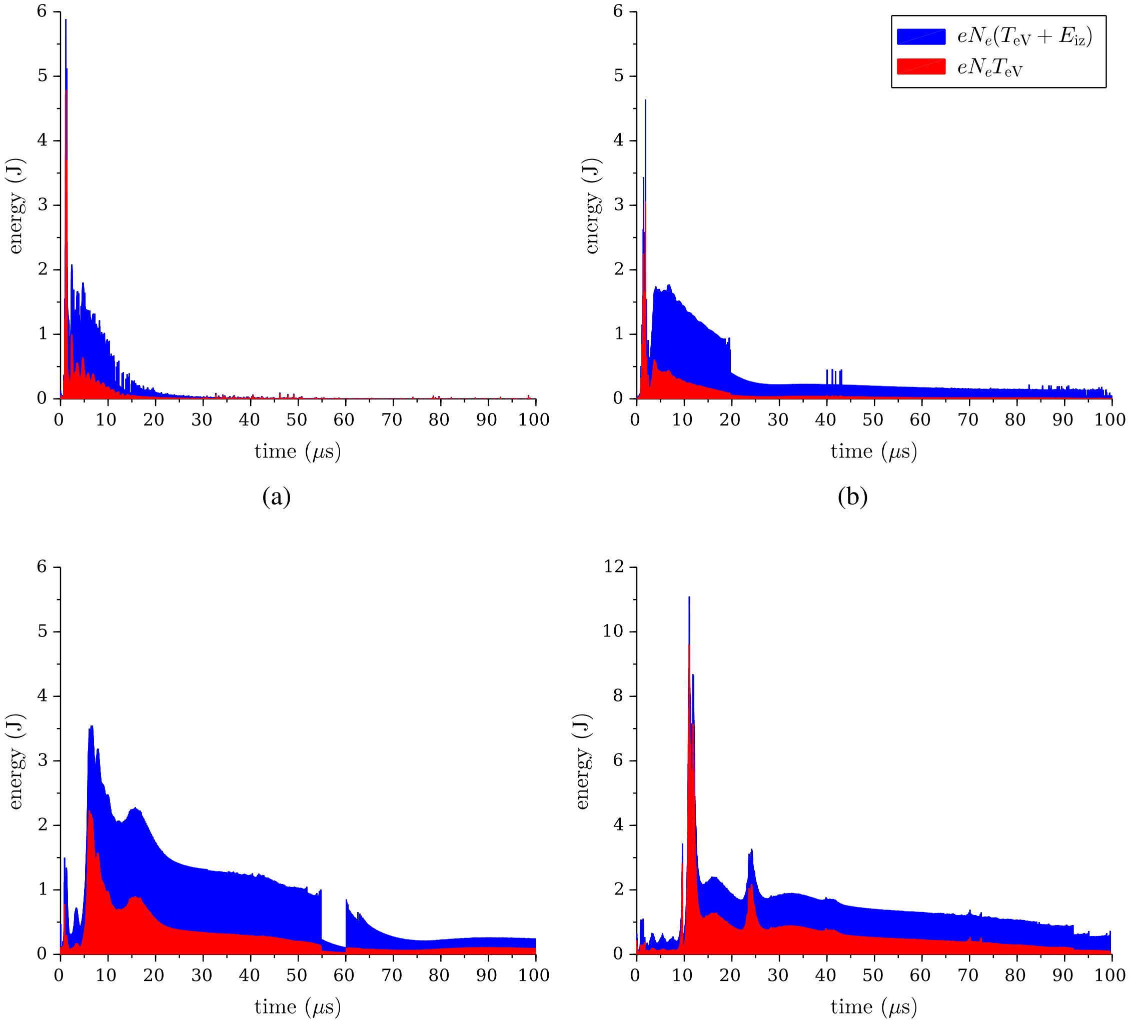

(a) (b)

(c) (d)

Figure 5.2. Time-resolved energy in electrons (eT_{eV}) and ions (eE_{iz}) radially integrated over total volume for (a) hydrogen, (b) helium, (c) argon, and (d) xenon at 50 mTorr. Note the different scale for (d).

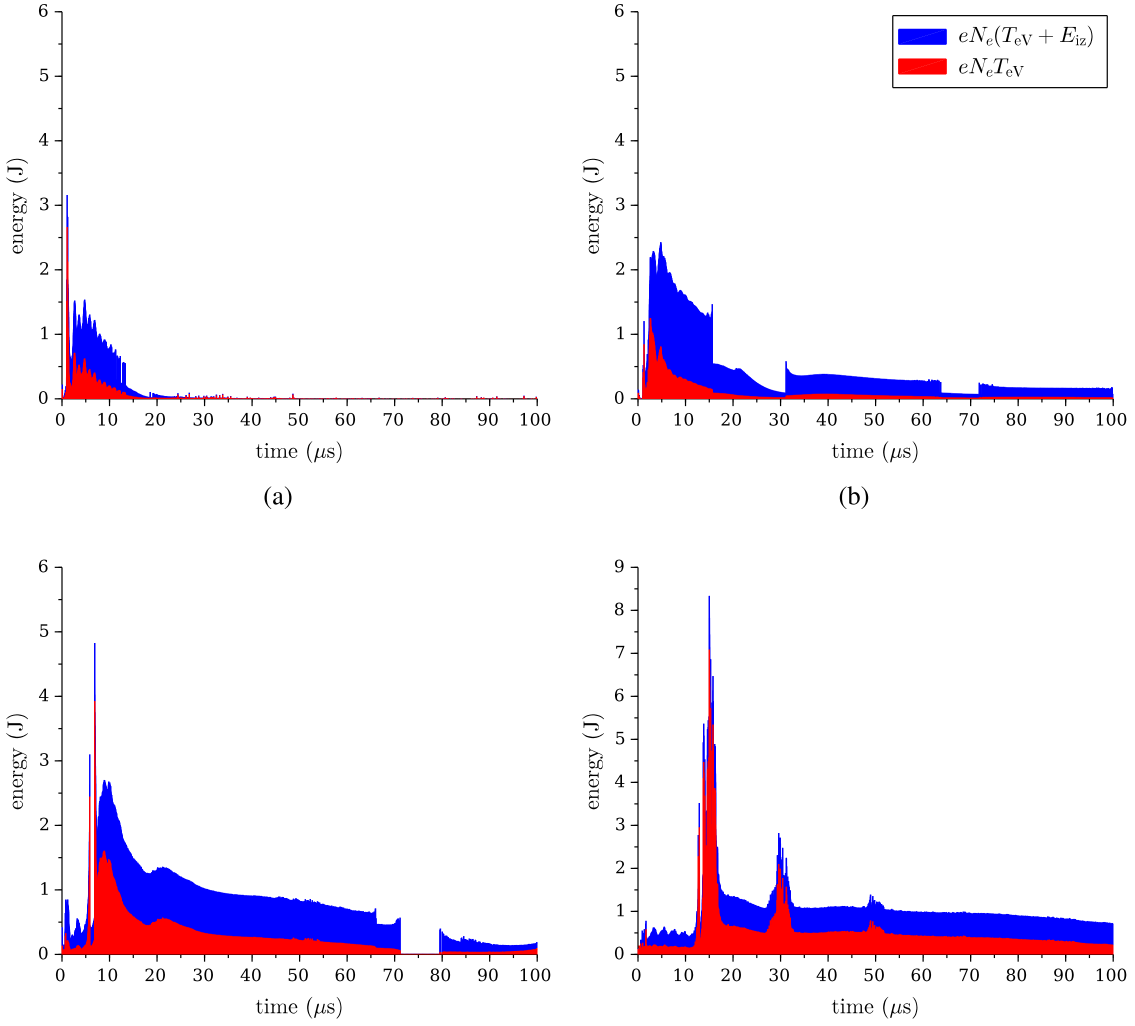

(a) (b)

(c) (d)

Figure 5.3. Time-resolved energy in electrons (eT_{eV}) and ions (eE_{iz}) radially integrated over total volume for (a) hydrogen, (b) helium, (c) argon, and (d) xenon at 100 mTorr. Note again the different scale for (d).

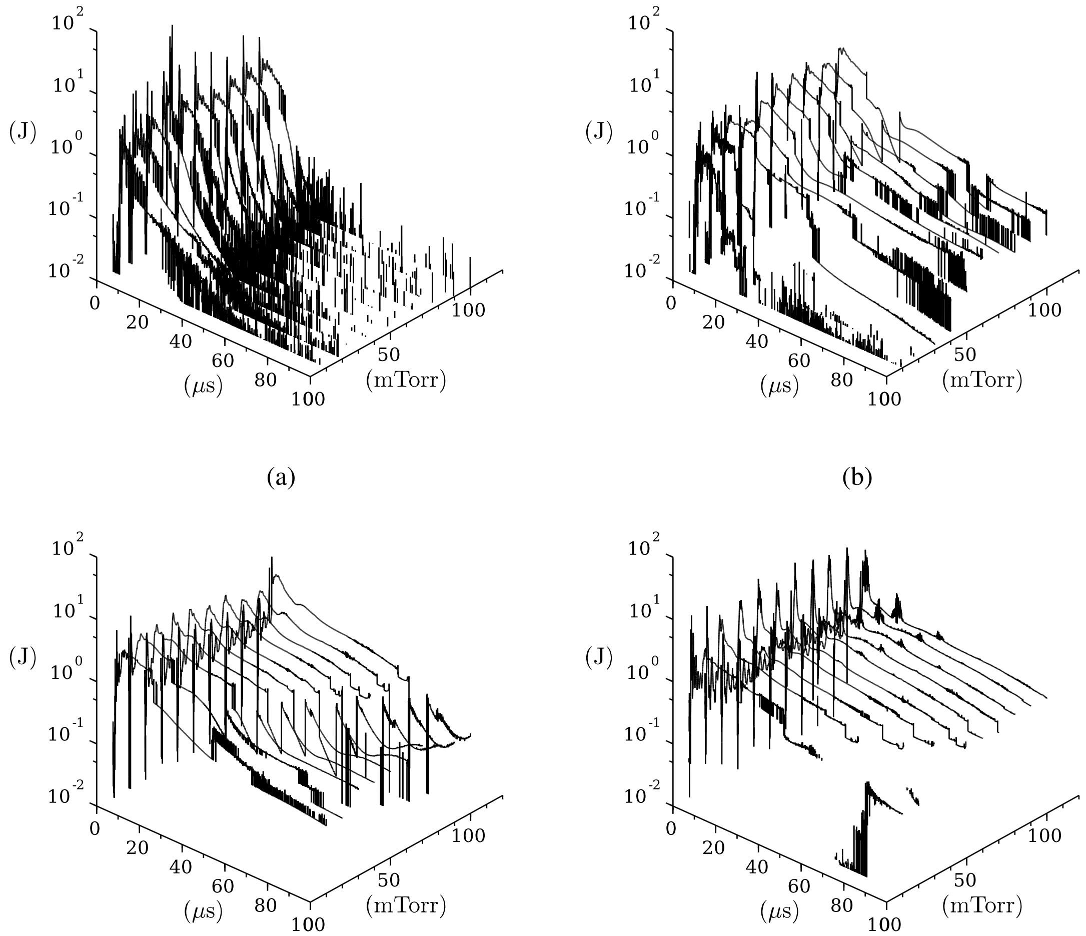

(a)

(b)

(c)

(d)

Figure 5.4. Time-resolved total energies (ion+electron) in (a) hydrogen, (b) helium, (c) argon, and (d) xenon at all pressures. Note equal vertical logarithmic scales from 0.01 to 100 J for all gas species.

consistently exceeds that in ions with the former out weighing the latter by a factor of $3.7^{+2.0}_{-1.2}$, $1.2^{+0.7}_{-0.7}$, $1.6^{+1.7}_{-0.5}$, and $5.8^{+1.9}_{-3.3}$ on average for hydrogen, helium, argon, and xenon, respectively. Peak electron energy in xenon is also consistently higher than all other gas species for all pressures with peaks on average for xenon being $2.6^{+2.0}_{-1.5}$, $7.3^{+6.9}_{-4.4}$, and $5.4^{+4.0}_{-3.9}$ higher than hydrogen, helium, and argon, respectively. Peak energy in ions is a much more mixed result with xenon being highest at 2.6 J in 10 mTorr to helium being highest at 1.6 J in 100 mTorr. All gas species except helium exhibited an overall decrease in ion energy from 10 to 100 mTorr with xenon seeing the largest decrease of 52% over the total pressure range.

Figure 5.6 shows the peak in the *total*, or the sum of the energies over the pressure range for all species. This should not be confused with the sum of the peaks that would be obtained by simply adding the energies seen in Figures 5.5a and 5.5b. As peak ion and electron energy may occur at different times it is important to make this distinction. Figure 5.6 shows a peak total energy result similar to that of peak electron energy in that xenon is consistently higher than all other species across the entire pressure range. Specifically, total energy in xenon is $2.4^{+1.8}_{-1.2}$, $4.7^{+4.5}_{-2.3}$, and $3.7^{+2.4}_{-2.2}$ times higher on average than hydrogen, helium, and argon, respectively. Change in peak total energy over the entire pressure range tested concludes that peak total energy goes down from 10 to 100 mTorr. Figure 5.6 data yields a decrease in peak total energy of around 21% for both hydrogen and helium, and argon & xenon losing around 6% and 5%, respectively.

5.2. COMPARISON WITH PREVIOUS MPX WORK

It should be noted that only thermal energy in electrons and minimum direct ionization energy are quantified. In the context of total energy and energy loss mechanisms several are not taken into account with this approach. Some of these include energy in un-absorbed light emission, lost via particle flux losses to the walls and ends, and directed motion such as induced azimuthal currents. In addition, the radial probe location $r = R$

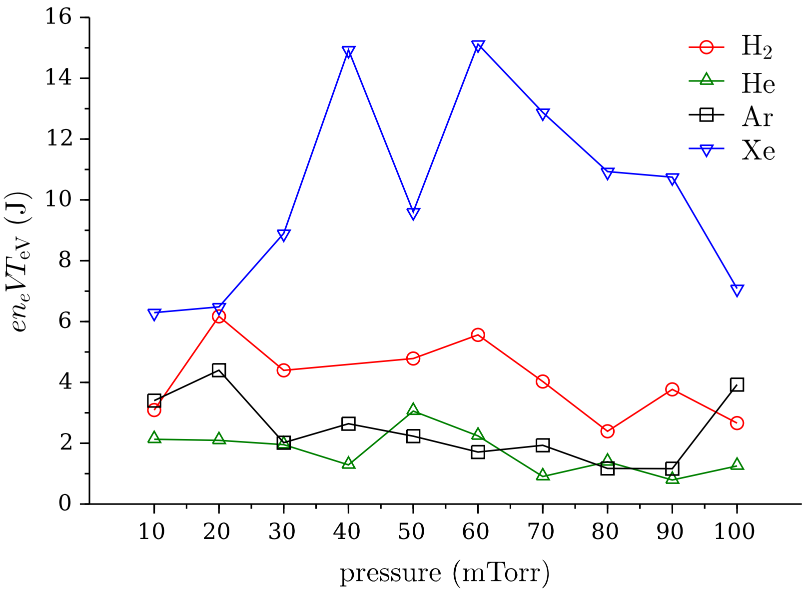

(a)

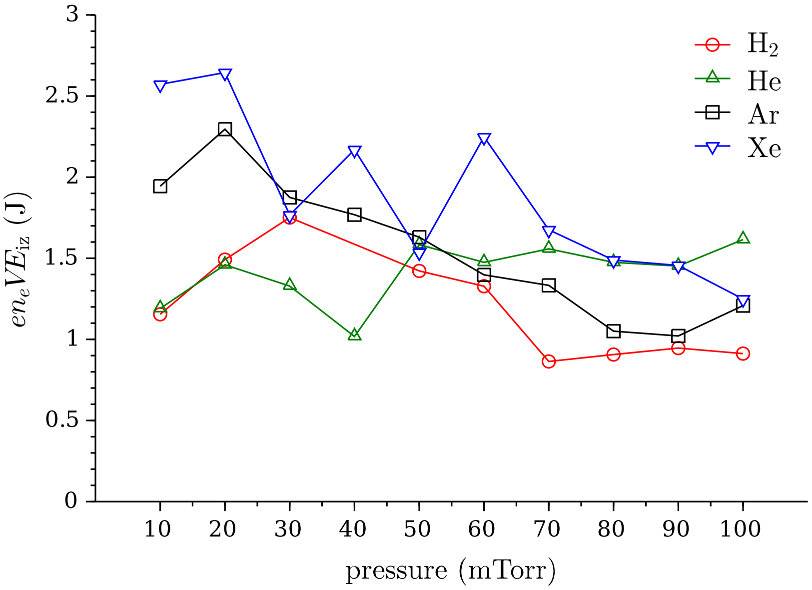

(b)

Figure 5.5. Radially integrated electron (a) and ion (b) energy peak between 0 and 100 μs as a function of pressure. Hydrogen data at 40 mTorr omitted due to an invalid data set.

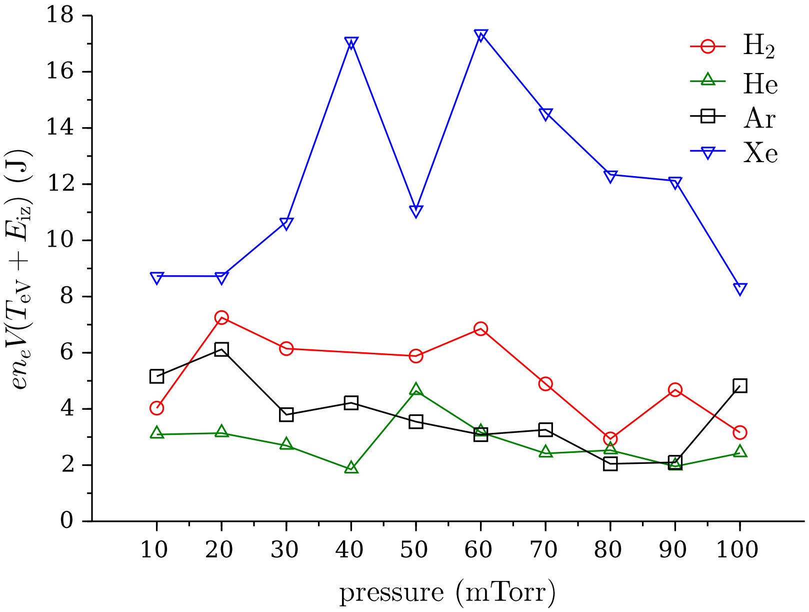

Figure 5.6. Radially integrated total (ion+electron) energy peak between 0 and 100 µs as a function of pressure. Hydrogen data at 40 mTorr omitted due to an invalid data set.

is not included in this analysis which could be withholding significant additional energy. With these considerations in mind, energy magnitudes seen in this work consistently (and as expected) come up short of total energy losses estimated in MPX previously.

Total dissipated energy levels reported in previous work are as much as 21 J in hydrogen[21]. Pahl and Rovey stated that hydrogen, argon, and xenon “show increased ohmic energy dissipation as pressure increases.” Returning to Figure 5.4 mixed results are observed. No appreciable increase in the sum of ion and electron energies appears to be taking place for increased pressure for any of these three gases. Retention of energy, or the observation of a species to lose energy more slowly does show a weak pressure dependence. However argon and xenon exhibit an opposite trend to that of hydrogen. Trends seen in Figure 5.5b for peak ion energy do follow those seen by Pahl and Rovey for inductive plasma energy with that work reporting a drop of 14%, 8%, and 14% inductive energy from 10 to 100 mTorr in hydrogen, argon, and xenon, respectively. While Figure

Table 5.2. Percentage of total dissipated energy reported by Pahl and Rovey (2014) accounted for in this work by the sum of ionization and electron thermalization.

	pressure (mTorr)	
species	10	100
H_2	27	15
Ar	32	24
Xe	54	40

5.5b shows a drop in peak ion energy of 21%, 38%, and 51% for the same from 10 to 100 mTorr.

Finally, Table 5.2 shows the percentage of the total dissipated circuit energy reported in [21] accounted for in this work by the peak sum of ionization and electron thermalization in 10 and 100 mTorr. It is seen here that electron and ion energy in xenon at 10 mTorr accounts for over half of the reported total energy dissipated for that pressure and species. Then peaking at almost 90% at 40 mTorr only to reduce to 40% at 100 mTorr. In comparison, this work can only account for a maximum of 27% and 32% in hydrogen and argon, respectively. Given this information it is concluded that, of the gases tested, xenon provides the greatest percent transfer of initially stored capacitive energy to ionization and electron thermalization, or heating. It is further concluded that this is primarily the result of two contributing factors; 1.) that xenon has the lowest ionization potential of the four species tested and, 2.) due to its higher mass it is allowed to remain in close proximity to the increased-coupling radial edge region for longer periods, giving more time for ionization and electron heating.

6. CONCLUSIONS

Pulsed inductive plasma studies were preformed on hydrogen, helium, argon, and xenon over a pressure range of 10 to 100 mTorr. The main inductive discharge was of a cylindrical geometry with a characteristic under-damped frequency of around 440 to 460 kHz and stored capacitive energy of 79 joules.

Analysis of full discharge time-integrated argon and xenon spectra demonstrates the absence of contaminant species during testing by accounting for all dominant peaks. These long duration spectra show excellent agreement with NIST cross-referencing as well as a complete lack of off-species spectra. Collisionl-statistics modeling utilizing neutral excited state transitions from the $2p$ to $1s$ orbital sub-shells appearing in the IR-band allowed for a first-approximation of time-resolved electron temperature in argon and xenon backfill pressures of 10 to 100 mTorr. Different modeling schemes and their associated assumptions provide different regimes of temperature estimation. Steady-state corona model assumptions yield a time-resolved electron temperature limited to around 10 eV in argon. While collisional-radiative model assumptions yield temperatures in the 10's of volts up to 100 eV in both argon and xenon.

Comparison between results obtained by line-ratio methods and by internal probe methods concludes that the inductive plasma studied in this work is best described by corona model assumptions with electron temperatures typically not more than 20 eV. Double probe studies performed at 10, 30, 50, 70, and 90 mTorr argon and at the $r = {}^{R}\!/_{2}$ radial probe location are used to validate triple probe results. Agreement between the probe methods within 26% and 12% for electron temperature and density, respectively, is seen in early times out to around 12 μs or roughly the first half of the discharge time. Upon which some divergence is seen due to what is best described as an ion acoustic wave translating across the probe radially inward. After which probe agreement returns. Estimated ionization levels are limited to less than 1% in hydrogen and helium. While argon transitions from 10 to 3% from 10 to 100 mTorr and xenon transitions from 28 to 4.5% from 10 to 100 mTorr, repectively. Time-resolved electron temperature and density profiles in hydrogen an helium plasmas are seen to oscillate at approximately double main inductive discharge frequencies. While the same in argon and xenon plasmas are seen to oscillate at the same frequency as the discharge.

An energy analysis using triple probe temperature and density estimates shows that the heavier gases of argon and xenon are able to retain energy in thermalized electrons and ionization out to nearly 100 μs. While the lighter hydrogen and helium gases lose this energy before or shortly after the main discharge end of 23 μs. Peak energy in electrons is consistently higher than that in ions by a factor of 1.2 to 5.8 with xenon being the greatest. Peak electron energy in xenon is also consistently higher than that in the other three gases by a factor of 2.6 for hydrogen to 7.3 for helium. Peak energy in ions is seen to decrease with increased pressure by as much as 52% from 10 to 100 mTorr. Peak total energy also favors xenon by a factor of 2.4 to 4.7 compared to hydrogen and helium, respectively. Peak total energy is also seen to decrease from 10 to 100 mTorr by 21% for the lighter gases and around 5 to 6% in the heavier gases.

Comparison with previous MPX work that focused losses by the discharge circuit shows that trends in energy losses to electron thermalization and ionization follow reported trends for inductive energy loss by going down from 10 to 100 mTorr. While the overall increase in dissipated circuit energy with pressure is not observed here. Finally, this work was able to account for between 15 and 54% of the total dissipated circuit energy reported previously as being entrained in electron thermalization and ionization.

BIBLIOGRAPHY

[1] S. Zhang, G.A. Wurden, T.P. Intrator, E.L. Ruden, W.J. Waganaar, C.T. Grabowski, R.M. Renneke, and J.H. Degnan. High-density field-reversed configuration plasma for magnetized target fusion. *Plasma Science, IEEE Transactions on*, 34(2):223–228, April 2006. ISSN 0093-3813. doi: 10.1109/TPS.2006.872164. URL `http://dx.doi.org/10.1109/TPS.2006.872164`.

[2] Patrick D. Pedrow and Abutaher M. Nasiruddin. Experimental study of CF_4 conical theta pinch plasma expanding into vacuum. *Plasma Science, IEEE Transactions on*, 17(1):17–23, Feb 1989. ISSN 0093-3813. doi: 10.1109/27.21666. URL `http://dx.doi.org/10.1109/27.21666`.

[3] B. Kronast, H. Röhr, E. Glock, H. Zwicker, and E. Fünfer. Measurements of the ion and electron temperature in a theta-pinch plasma by forward scattering. *Phys. Rev. Lett.*, 16:1082–1085, June 1966. doi: 10.1103/PhysRevLett.16.1082. URL `http://link.aps.org/doi/10.1103/PhysRevLett.16.1082`.

[4] N Takeuchi, K Yasuoka, and I Shozo. Surface modification of thin dielectric materials by compact theta-pinch plasma. Intl. Conference On Plasma Sci., Monterey, CA, June 2005. IEEE.

[5] S J Koelfgen and C W Hawk. A plasmoid thruster for space propulsion. 39th Joint Propulsion Conference and Exhibit, Hustsville, AL, July 2003. AIAA.

[6] F R T Luna, G H Cavalcanti, and A G Trigueiros. A theta-pinch as a spectroscopic light source. *Journal of Physics D: Applied Physics*, 31(7):866, 1998. URL `http://stacks.iop.org/0022-3727/31/i=7/a=015`.

[7] R. Alani, H. Azodi, M. Naraghi, B. Safaii, and A. Torabi-Fard. Material testing in a linear theta pinch. *Journal of Nuclear Materials*, 113(1):25 – 32, 1983. ISSN 0022-3115. doi: http://dx.doi.org/10.1016/0022-3115(83)90162-9. URL `http://www.sciencedirect.com/science/article/pii/0022311583901629`.

[8] D J Griffiths. *Introduction to Electrodynamics*. Addison Wesley, Boston, 3rd edition, 1999. ISBN 0-13-805326.

[9] D E Kirtley. *Study of the Synchronous Operation of an Annular Field Reversed Configuration Plasma Device*. PhD thesis, Dept. of Aerospace Engineering, Univ. of Michigan, Ann Arbor, MI, 2008.

[10] C Grabowski, J H Degnan, D J Amdahl, R Delaney, M Domonkos, F M Lehr, R Magallanes, P R Robinson, E L Ruden, W White, H Wood, D Gale, M Kostora, J McCullough, W Sommars, M H Frese, S D Frese, J F Camacho, S K Coffey, V Makhin, T P Intrator, G A Wurden, J Sears, P J Turchi, W J Waganaar, T Weber, R E Siemon,

S Fueling, B S Bauer, A G Lynn, and N F Roderick. FRC lifetime studies for the field reversed configuration heating experiment (FRCHX). 53rd Plasma Physics Meeting, Salt Lake City, UT, 2011. APS.

[11] R H Lovberg and C L Dailey. Large inductive thruster performance measurement. *AIAA*, 20(7):971–977, July 1982.

[12] G Wurden, T Intrator, S Zhang, I Furno, S Hsu, J Park, R Kirkpatrick, R Renneke, K Schoenberg, M Taccetti, M Tuszewski, W Waganaar, Z Wang, R Siemon, J Degnan, D Gale, C Grabowski, E Ruden, W Sommars, M Frese, S Coffey, G Craddock, S Frese, and N Roderick. FRC plasma studies on the FRX-L plasma injector for MTF. In *IC/P6-53*, Vilamoura, Portugal, November 2004. IAEA. URL `http://www-pub.iaea.org/MTCD/Meetings/PDFplus/2004/cn116BofA.pdf`.

[13] E Y Choueiri and K A Polzin. Faraday acceleration with radio-frequency assisted discharge. *J. Propuls. Power*, 22(3):611–619, June 2006.

[14] Glenn Wurden. FRCHX magnetized target fusion HEDLP experiments. In *IC/P4-13*, Geneva, Switzerland, October 2008. IAEA. URL `http://www-pub.iaea.org/MTCD/Meetings/PDFplus/2008/cn165/cn165_BookOfAbstracts.pdf`.

[15] J Slough, D Kirtley, and T Weber. Pulsed plasmoid propulsion: The ELF thruster. 31st International Electric Propulsion Conference, Ann Arbor, MI, September 2009. ERPS.

[16] D Kirtley, J T Slough, C Pihl, E Meier, and R D Milroy. Pulsed plasmoid propulsion: Air-breathing electromagnetic propulsion. 32nd International Electric Propulsion Conference, Wiesbaden, Germany, September 2011. ERPS.

[17] D Kirtley, J Pihl, and C Pihl. Development of a steady operating pulsed power system for frc and inductive thrusters. 33nd International Electric Propulsion Conference, George Washington University, Washington, D.C., October 2013. ERPS. URL `http://www.iepc2013.org/get?id=361`.

[18] R D Milroy and J U Brackbill. Numerical studies of a field-reversed theta-pinch plasma. *AIP Phys. Fluids*, 25(5):775–783, May 1982.

[19] K A Polzin, J P Reneau, and S Kameshwaran. Incorporation of an energy equation into a pulsed inductive thruster performance model. 32nd International Electric Propulsion Conference, Wiesbaden, Germany, September 2011. ERPS.

[20] Warner C. Meeks and Joshua L. Rovey. On the delayed gas breakdown in a ringing theta-pinch with bias magnetic field. *IOP Phys. of Plasmas*, 19(5):052505, 2012. doi: 10.1063/1.4717731. URL `http://link.aip.org/link/?PHP/19/052505/1`.

[21] R.A. Pahl and J.L. Rovey. Energy analysis of a pulsed inductive plasma through circuit simulation. *Plasma Science, IEEE Transactions on*, 42(10):3411–3418, Oct 2014. ISSN 0093-3813. doi: 10.1109/TPS.2014.2355717.

[22] R A Pahl, W C Meeks, and J L Rovey. Magnetic field mapping of a field reversed configuration test article. 47th Joint Propulsion Conference & Exhibit, San Diego, CA, 2011. AIAA. URL `http://arc.aiaa.org/doi/abs/10.2514/6.2011-5656`.

[23] R A Pahl and J L Rovey. Pre-ionization plasma in a FRC test article. 50th Aerospace Sciences Meeting, Nashville, TN, 2012. AIAA. URL `http://arc.aiaa.org/doi/abs/10.2514/6.2012-194`.

[24] Ryan A. Pahl, Joshua L. Rovey, and David J. Pommerenke. Comparison of magnetic probe calibration at nano and millitesla magnitudes. *Review of Scientific Instruments*, 85(1):015112–015112–6, Jan 2014. ISSN 0034-6748. doi: 10.1063/1.4861364. URL `http://dx.doi.org/10.1063/1.4861364`.

[25] Kurt Polzin, Millard Rose, and Robert Miller. Operational characteristics of a low-energy FARAD thruster. 44th Joint Propulsion Conference & Exhibit. AIAA, July 2008. ISBN 978-1-60086-992-1. doi: 10.2514/6.2008-5011. URL `http://arc.aiaa.org/doi/abs/10.2514/6.2008-5011`.

[26] C. Teske, J. Jacoby, F. Senzel, and W. Schweizer. Energy transfer efficiency of a spherical theta pinch. *Physics of Plasmas*, 17(4), 2010. doi: 10.1063/1.3368795. URL `http://scitation.aip.org/content/aip/journal/pop/17/4/10.1063/1.3368795`.

[27] R. Lovberg. Magnetic probes. In R H Huddlestone and L L Stanley, editors, *Plasma diagnostic techniques*, pages 69–112. Academic Press, Ch.3, 1965.

[28] F. Chen. Electric probes. In R H Huddlestone and L L Stanley, editors, *Plasma diagnostic techniques*, pages 113–200. Academic Press, Ch.4, 1965.

[29] R. McWhirter. Spectral intensities (and applied predictive models). In R H Huddlestone and L L Stanley, editors, *Plasma diagnostic techniques*, pages 201–264. Academic Press, Ch.5, 1965.

[30] W. Wiese. Line broadening. In R H Huddlestone and L L Stanley, editors, *Plasma diagnostic techniques*, pages 265–318. Academic Press, Ch.6, 1965.

[31] E. Turner. Optical and ultraviolet techniques. In R H Huddlestone and L L Stanley, editors, *Plasma diagnostic techniques*, pages 319–358. Academic Press, Ch.7, 1965.

[32] T. Stratton. X-ray spectroscopy. In R H Huddlestone and L L Stanley, editors, *Plasma diagnostic techniques*, pages 359–398. Academic Press, Ch.8, 1965.

[33] M. Kimmitt, A. Prior, and V. Roberts. Far-infrared techniques. In R H Huddlestone and L L Stanley, editors, *Plasma diagnostic techniques*, pages 399–430. Academic Press, Ch.9, 1965.

[34] R. Alpher and D. White. Optical interferometry. In R H Huddlestone and L L Stanley, editors, *Plasma diagnostic techniques*, pages 431–476. Academic Press, Ch.10, 1965.

[35] C. Wharton. Microwave techniques. In R H Huddlestone and L L Stanley, editors, *Plasma diagnostic techniques*, pages 477–516. Academic Press, Ch.11, 1965.

[36] J. Osher. Particle measurements. In R H Huddlestone and L L Stanley, editors, *Plasma diagnostic techniques*, pages 517–601. Academic Press, Ch.12, 1965.

[37] S. Chen and T. Sekiguchi. Instantaneous Direct-Display system of plasma parameters by means of triple probe. *Journal of Applied Physics*, 36(8):2363–2375, 1965. doi: 10.1063/1.1714492. URL `http://dx.doi.org/10.1063/1.1714492`.

[38] S. Chen. Studies of the effect of ion current on instantaneous tripleâĂŘprobe measurements. *Journal of Applied Physics*, 42(1):406–412, 1971. doi: http://dx.doi.org/10.1063/1.1659611. URL `http://scitation.aip.org/content/aip/journal/jap/42/1/10.1063/1.1659611`.

[39] M. Yokota. Electron temperature of helium plasmas produced by theta pinch. *Physical Society of Japan*, 18(3):419–426, 1963. doi: 10.1143/JPSJ.18.419. URL `http://dx.doi.org/10.1143/JPSJ.18.419`.

[40] C C Lin. Ground state excitation cross sections, jun 2008. URL `http://raptor.physics.wisc.edu/`.

[41] Ronald J. Sovie. Spectroscopic determination of electron temperature and percentage ionization in a helium plasma. *Physics of Fluids*, 7(4):613–614, 1964. doi: 10.1063/1.1711250. URL `http://scitation.aip.org/content/aip/journal/pof1/7/4/10.1063/1.1711250`.

[42] S. Iordanova and I. Koleva. Optical emission spectroscopy diagnostics of inductively-driven plasmas in argon gas at low pressures. *Spectrochim. Acta Part B*, 62(4), April 2007. ISSN 0584-8547. doi: 10.1016/j.sab.2007.03.026. URL `http://www.sciencedirect.com/science/article/pii/S0584854707000699`.

[43] D. L. Crintea, U. Czarnetzki, S. Iordanova, I. Koleva, and D. Luggenhölscher. Plasma diagnostics by optical emission spectroscopy on argon and comparison with thomson scattering. *J. Phys. D: Appl. Phys.*, 42(4):045208, February 2009. ISSN 0022-3727. doi: 10.1088/0022-3727/42/4/045208. URL `http://iopscience.iop.org/0022-3727/42/4/045208`.

[44] Yu-hui Chiu, Brad L. Austin, Skip Williams, Rainer A. Dressler, and George F. Karabadzhak. Passive optical diagnostic of Xe-propelled hall thrusters. I. Emission cross sections. *J. Appl. Phys.*, 99(11):113304–113304–11, June 2006. ISSN 00218979. doi: 10.1063/1.2195018. URL `http://jap.aip.org/resource/1/japiau/v99/i11/p113304_s1`.

[45] George F. Karabadzhak, Yu-hui Chiu, and Rainer A. Dressler. Passive optical diagnostic of Xe propelled Hall thrusters. II. Collisional-radiative model. *J. Appl. Phys.*, 99(11):113305–113305–12, June 2006. ISSN 00218979. doi: 10.1063/1.2195019. URL `http://jap.aip.org/resource/1/japiau/v99/i11/p113305_s1`.

[46] O Zatsarinny and K Bartschat. B-spline Breit-Pauli R-matrix calculations for electron collisions with argon atoms. *Journal of Physics B: Atomic, Molecular and Optical Physics*, 37(23):4693, 2004. URL `http://stacks.iop.org/0953-4075/37/i=23/a=010`.

[47] M. Allan, O. Zatsarinny, and K. Bartschat. Near-threshold absolute angle-differential cross sections for electron-impact excitation of argon and xenon. *Phys. Rev. A*, 74: 030701, September 2006. doi: 10.1103/PhysRevA.74.030701. URL `http://link.aps.org/doi/10.1103/PhysRevA.74.030701`.

[48] J R Taylor and C D Zafiratos. *Modern Physics for Scientists and Engineers*. Pearson-Prentice Hall, Upper Saddle River, NJ, 1st edition, 1991.

[49] Yusuf Celik, Tsanko V. Tsankov, Mitsutoshi Aramaki, Shinji Yoshimura, Dirk Luggenhölscher, and Uwe Czarnetzki. Recombination and enhanced metastable repopulation in the argon afterglow. *Phys. Rev. E*, 85:056401, May 2012. doi: 10.1103/PhysRevE.85.056401. URL `http://link.aps.org/doi/10.1103/PhysRevE.85.056401`.

[50] P A Tipler and G Mosca. *Physics for Scientists and Engineers*. W.H.Freeman and Co., New York, NY, 6th edition, 2008.

[51] Jen-Shih Chang, G L Ogram, R M Hobson, and S Teii. The instantaneous triple-probe method for the direct display of plasma parameters in a low density continuum plasma. *Journal of Physics D: Applied Physics*, 13(6):1083–1093, 1980. URL `http://stacks.iop.org/0022-3727/13/i=6/a=018`.

[52] H. M. Mott-Smith and Irving Langmuir. The theory of collectors in gaseous discharges. *Phys. Rev.*, 28:727–763, Oct 1926. doi: 10.1103/PhysRev.28.727. URL `http://link.aps.org/doi/10.1103/PhysRev.28.727`.

[53] M A Lieberman and A J Lichtenberg. *Principles of Plasma Discharges and Materials Processing*. John Wiley & Sons, Inc., Hoboken, 2nd edition, 2005.

[54] I H Hutchinson. *Principles of Plasma Diagnostics*. Cambridge Univ. Press, 2nd edition, 2002. ISBN 0-521-67574-x.

[55] F F Chen. Langmuir probe diagnostics. 30th International Conference on Plasma Sciences, Short Course, Jeju, Korea, June 2003. IEEE.

[56] F F Chen. *Introduction to Plasma Physics and Controlled Fusion*, volume 1. Springer, New York, 2nd edition, 2006. ISBN 0-306-41332-9.

[57] E. O. Johnson and L. Malter. A floating double probe method for measurements in gas discharges. *Phys. Rev.*, 80:58–68, Oct 1950. doi: 10.1103/PhysRev.80.58. URL `http://link.aps.org/doi/10.1103/PhysRev.80.58`.

[58] R A Pahl. *Energy Deposition into Heavy Gas Plasma via Pulsed Inductive Theta-Pinch*. PhD thesis, Dept. of Mechanical and Aerospace Engineering, Missouri S&T, Rolla, MO, 2014.

[59] F Mackel, P Kempkes, H Stein, J Tenfelde, and H Soltwisch. Electrostatic probe measurements in a pulsed-power plasma and comparison with interferometry. *Measurement Science and Technology*, 22(5):055705, 2011. URL `http://stacks.iop.org/0957-0233/22/i=5/a=055705`.

[60] M Y Naz, A Ghaffar, N U Rehman, S Naseer, and M Zakaullah. Double and triple Langmuir probes measurements in inductively coupled nitrogen plasma. *Progress in Electromagnetics Research*, 114:113–128, 2011. URL `http://www.jpier.org/pier/pier.php?paper=10110309`.

[61] L Byrne, N A Gatsonis, and E Pencil. Triple langmuir probe measurements in the plume and backflow region of a pulsed plasma thruster. 37th Joint Propulsion Conference & Exhibit, Salt Lake City, UT, July 2001. AIAA.

VITA

Warner Meeks was born and raised in St. Louis, Missouri to loving parents with no college education of their own. Characterized as an under-achiever during his attendance at Hazelwood Central Senior High, Warner set out into the workforce after graduation from public school. Upon spending a few years holding down various blue-collar jobs it occurred to him that his parents were right and a college education was the way to go.

Warner attend St. Louis Community College for a few years and then transferred to Missouri S&T. Upon transfer he particiated in the Federal Work-Study program for a few years as a machinist's assistant in McNutt Hall and interned as an Air Force Research Laboratory Space Scholar in 2009. As an Space Scholar Warner studied solar weather forecasting models which included the validation of the Wang-Sheeley-Arge model now used routinely at the Space Weather Prediction Center. He received his B.S. in Aerospace Engineering in May of 2010 and his M.S. in the same in December of 2012 with a thesis entitled "Studies of Inductive Plasmas and their Application to Theta-Pinch Devices via Numerical Modeling". During his graduate studies Warner has presented at six international conferences and published work in AGU's Space Weather, IEEE's Transactions on Plasma Sciences, and AIP's Physics of Plasmas.

Receiving his PhD. in Aerospace Engineering in August of 2015, Warner has taken an Assistant Teaching Professor position within the Mechanical & Aerospace Engineering Department at Missouri S&T.